ADVANCEMENTS IN TUNING TECHNIQUES FOR MICROWAVE PASSIVE AND ACTIVE CIRCUITS

A Dissertation

by

ALIREZA POURGHORBAN SAGHATI

Submitted to the Office of Graduate and Professional Studies of
Texas A&M University
in partial fulfillment of the requirements for the degree of

DOCTOR OF PHILOSOPHY

Chair of Committee,	Kamran Entesari
Committee Members,	Robert D. Nevels
	Jun Zou
	Ben Zoghi
Head of Department,	Miroslav M. Begovic

December 2015

Major Subject: Electrical Engineering

ABSTRACT

Due to the rapid development of wireless systems, the demand for communication devices that can operate in different bands is increased. The passive solution, as a result, can be one of the multiple-frequency, wideband, or reconfigurable/tunable choices. It is true that multi-frequency structures have the advantage of serving multiple frequencies at the same time, but the crosstalk from neighbor bands makes them a weak choice in comparison to tunable/reconfigurable devices. Unlike multiple/wide band microwave devices, tunable structures offer better isolation. Moreover, covering multiple bands should not decrease the selectivity and Q of the device, which is not a true statement for multi-frequency structures.

The major focus of this dissertation was to address key issues in designing tunable microwave devices. Different tunable microwave structures, specifically antennas, using mainly two methods are presented. The first method is based on loading substrate integrated waveguide (SIW) cavities with via posts and then connecting them to switching devices. Three antenna designs and one SIW-based VCO is designed and implemented based on the proposed technique. The tuning technique is first developed using a conventional SIW cavity backed antenna to achieve an octave tunable antenna with $\sim$65% of miniaturization. For the second and third antennas the method is applied to SIW antennas along with different miniaturization methods that result in tunable directive antennas with more than 80% of miniaturization.

The second method is a different technique, which is based on loading the microwave devices and antennas with non-toxic liquid metal materials. While the first SIW-based approach offers wide tuning range with high quality factor/efficiency, the latter makes it possible to avoid using lossy and power consuming switches or var-

actor diodes. Using the second technique, tunable microwave filters and antennas that are suitable for high-power applications are proposed. A major part of this work also dealt with measurement techniques to prove the suitability of microfluidic-based tuning techniques for high-power applications.

To

My Mother, Mahkameh,

My Father, Javad,

and

My Brother, Aliabas

ACKNOWLEDGEMENTS

"If you want to find the secrets of universe, think in terms of energy, frequency, and vibration."— Nikola Tesla

I would like to appreciate my adviser, Professor Kamran Entesari. Without his help and support I could not have the opportunity to come to the Texas A&M University. Working under his supervision during the last four years, has greatly elevated my levels of standard for quality, research, and thinking. His trust, patience, and support helped me learn lessons that I hope I will never forget. I would also like to thank Professor Robert Nevels for being a member of my committee and also his guidance, support, and encouragement during our meetings. He is truly one of the best teachers I have ever had. I must acknowledge the participation, support, and feedback of the rest of my dissertation committee members, Professor Jun Zou, and Professor Behbood Zoghi.

I must thank Professor Kamal Sarabandi of University of Michigan. I have used his advice many times during my masters and doctoral studies. For this I am immeasurably grateful. He is one true teacher that I always admire.

I would also like to thank my officemates/friends, Shokoufeh Arbabi, Sina Baghbani, Jaskirat Batra, Alferedo Costia, Vahid Dabbagh, Mohamed El-Kholy, Mohan Geddada, Dr. Jesus Efrain Gaxiola Sosa, Dr. Hajir Hedayati, Saman Kabiri, Masoud Moslehi, Samira Moslehi, Paria Sepidband, Sherif Shekib, Noah Yang, Jorge Zarate and Dr. Ehsan Zhian Tabasy.

Finally, I would like to thank my family. None of this would have happened without their love, support, and patience. My grandparents, specially my grandma, Setareh who was also one of my best teachers. She was the very first person who fig-

ured out my talent in mathematics. Words cannot express my feelings and how much I owe her my achievements. My parents, Mahkameh, and Javad, whose sacrifices and accomplishments have made my successes possible. It was their unconditional love and belief that motivated me to keep progressing during these years. You are my heroes. My dear brother Aliabas, who is definitely the best brother one can ever wish for. He always believed in a me that I could not see and helped me find my strengths that I wasn't aware of. With all my heart and to commemorate their love, I dedicate this dissertation to them.

A. Pourghorban Saghati

College Station, Texas

August 2015

TABLE OF CONTENTS

Page

LIST OF FIGURES

FIGURE Page

LIST OF TABLES

TABLE Page

1. INTRODUCTION

1.1 SIW Tunable Microwave Devices Using Semiconductor Components

Developing RF, Microwave, and Millimeter-wave systems require low-cost, mass-producible, high-performance, and high yield technologies for passive and active sections. Dealing with radio coexistence, and strong coupling between different subsystems while maintaining or even reducing the size and weight of the final system is a very challenging task. This is more critical when designing passive circuits such as resonators, antennas, highly-selective filters, couplers, power dividers, and circulators [2,3]. For years, the classical waveguide technology was and in some cases still is the main stream for designing high performance passive circuits and systems [4,5]. However, these bulky and heavy concomitants are not suitable for integration, and low-cost mass-production. Via posts were first used with the name of post-wall waveguide [6] or laminated waveguide [7] in 1998 to form a planar waveguide structure. Then by introduction of the Substrate Integrated Waveguide (SIW) technology as we know it today by Wu, et al. in 2003 [8], a remedy for full integration of active and passive circuits in a planar fashion was found [6–11]. Using this method, the non-planar rectangular waveguide can be made in planar form, compatible with existing PCB (Printed Circuit Board) and LTCC (Low-Temperature Co-fired Ceramic) techniques [12]. Conductive walls in classical waveguides are replaced with planar-compatible PCB via posts in SIW structures. Therefore, similar to classical metallic waveguides, by shortening the two openings of the SIW structure at both ends, SIW cavities also can be formed.

On the other hand, high Q resonators are the inevitable part of many high performance passive and active circuits. As a result, SIW is a very good candidate for

developing planar microwave devices with high quality factor. The SIW technology has been so far applied to many microwave components, such as post and cavity filters [8,13], antennas [14,15] directional couplers [16], oscillators [17,18], power amplifiers [19,20], slot array and leaky-wave antennas [21,22], and circulators [23]. The devices realized using SIW preserve most of the advantages of conventional metallic waveguides. Some of the advantages are:

1. Low loss and high quality factor for SIW cavities;
2. Permanent electrical isolation due to the shielding via posts;
3. High power handling;
4. Integrability capabilities of SIW structures with all sorts of passive and active components.

The first two items are proved to be as good as classical metallic waveguides, but the third advantage may be hindered to some extent in SIW. Based on the dielectric material used in the PCB fabrication process, and the height of the dielectric layer, the power handling capabilities of the SIW structure can be decreased. While the first three advantages are the intrinsic properties of 3-D waveguide structures, the integrability is an advantage that SIW inherits from planar structures. In other words, SIW has benefits of both 3-D and planar microwave structures in one place.

1.1.1 Why Tunable SIW?

Like almost all the resonance-based microwave structures, offering a quality factor in the range of couple of hundreds comes along with narrow bandwidth. Although, this is very helpful in designing highly selective microwave devices for a particular center frequency, sometimes covering a wider bandwidth is needed.

Besides, even in the narrow band applications, due to high sensitivity of the SIW structures (just similar to the resonant-based classical metallic cavity structures), in most cases post-fabrication tuning of the fabricated device is mandatory. This is required to fine-tune the device's operating frequency to the desired frequency response. Otherwise, corrective re-fabrication of the device is inevitable. On the other hand, unlike multiple/wide band microwave devices, tunable structures offer better isolation. It is true that multi-frequency structures have the advantage of serving multiple frequencies at the same time, but the crosstalk from neighbor bands makes them a weak choice in comparison to tunable/reconfigurable devices [24–26]. Moreover, covering multiple bands should not decrease the selectivity and Q of the device, which is not a true statement for multi-frequency structures. Knowing all the above and a revisit of [8–26] leads to several known reasons why tuning of SIW devices can be useful:

1. More standards/services can be covered by the same device;
2. Post-fabrication fine-tuning of the device becomes possible;
3. Less crosstalk sensitivity (better isolation) can be achieved while covering more bands.

The importance of SIW tuning needs to be discussed exclusively for antennas, and VCOs:

1.1.1.1 SIW Tunable Antennas

There are so many applications in which an antenna needs to be mounted on a conductive surface such as a vehicle, an airplane, or even a human body [27]. Antennas in these cases usually need to be high-gain. On the other hand, the increasing number of commercial wireless services comes along with increased antenna numbers

that a user-end device needs. The combination of these two points means antennas with high gain, mountable on conductive surfaces, and covering multiple services.

For the first two requirements, SIW antenna is a very good choice since it has a very high gain and also due to the cavity-backed structure it can be mounted on almost any surface without affecting its performance [28]. However, because of its narrow bandwidth it may not be a good choice to be used for multiple numbers of services. This is when tunability of SIW antennas becomes important.

1.1.1.2 SIW Tunable VCOs

Voltage-controlled oscillators (VCOs) are used as the local oscillator (LO) source in most radar and communication applications [29]. Some of the driving parameters for VCOs to be named are low phase-noise, high output power, low DC-power, high tuning range, and high harmonic suppression. Also, it is well-known that the performance of a VCO is highly affected by the Q of the passive resonator.

High Q, power handling, and isolation of SIW cavity resonators in addition to their integrability capabilities sounds very promising while designing oscillators. However, due to the difficulties of tuning these structures, they have not been used in VCO structures that often. As a result, a tuning method by which SIW resonators can be tuned over a wide tuning range while their quality factor variations are negligible is very demanding.

1.2 Microfluidically-tunable Microwave Devices

Based on the effort of various research groups, the idea of tuning microwave devices using semiconductor devices such as varactors or p-i-n diodes, and micro-electromechanical systems (MEMS) devices is very well-known to the RF/microwave community today [24, 30–33]. It has been shown in many different designs that tunable microwave devices can improve the performance of the radio in many ways.

Just to name some of the advantages one can recall efficient area consumption, reducing the number of passives needed, reducing the front-end complexity, the low crosstalk from neighbor bands, great noise-canceling capabilities while covering wide bandwidths, and excellent individual radio performance [24, 33]. However, no distinguished performance can be achieved without cost. While these high-performance concomitants offer very nice quality factors, bandwidth of operation, and switching speeds, they come with one worrisome drawback: these devices can only handle input power levels in the orders of less than watts [30]. While this is enough for many communication devices, tunable and high-power tolerable devices are needed in many other cases.

The second section of this dissertation explores the neoteric fluidic-based tuning methods. Whether the fluidics are being used as a switching or loading component or as the main conductor of a microwave device in the case of liquid metals, they have attracted much attention due their unique advantages in comparison with semiconductor and MEMS devices [34]. In general the boldest advantages of liquid-based methods can be listed as:

1. High linearity due to being 100% mechanical-based devices, which makes them an ideal choice for high-power-microwave applications;

2. employing soft materials using common technologies can result in flexible and wearable tunable devices easily;

3. there is no need for maintaining the actuation force once the state of the device is changed, since the liquids will remain in the same position.

Along with their advantages, just like any other emerging technology, there are some practical concerns and issues that need to be solved before these methods can be actually employed in commercial microwave devices.

1.3 Overview

The main purpose of this dissertation is a two-fold. First, to develop a tuning technique that is applicable to substrate integrated waveguide microwave structures (such as Antennas and VCOs) with major emphasis on: (1) widest possible tuning range, (2) high and consistent performance characteristics for all the tuned states, and (3) ease of implementation. Second, implementing a microfluidics-based tuning solution that is suitable for high-power tolerable microwave applications and characterizing the power tolerance capabilities.

Chapter II focuses specifically on frequency-tunable/reconfigurable SIW structures. First, a tuning technique based on loading an SIW cavity-backed antenna with via posts and connecting/disconnecting them from the cavity top/bottom walls is proposed. Using this technique, a tuning range of an octave is achieved for an antenna with directive radiation. Since, cavity-backed antennas are often large in size due to their nature, in the second part, a tunable miniature SIW-CBS antenna is proposed. The antenna achieves 85% of miniaturization with a tuning range of 1.8–4.9 GHz by switching between the negative and positive order modes. Third section also focuses on modifying the same tuning technique for an ultra-miniature SIW antenna. The antenna for this part is miniatured using a quarter-mode SIW cavity resonator which is radiating from the two open-ended fictitious magnetic walls. Finally, the forth section discusses the modification of a similar tuning technique and its application in a widely-tuned ultra-low phase-noise VCO.

In chapter III, the main focus is on microfluidically-tuned passive structures and their capabilities to be employed in high-power microwave applications. First, a tuning method based on employing liquid metal capacitive loading is presented. The method is applied to a co-planar waveguide (CPW) filter to achieve a tuning range

of 3.4–5.5 GHz. Using a costume measurement setup and by the aid of an infra red (IR) camera, the power handling capabilities of the filter are characterized and for the first time, it is proven that such tuning methods are suitable for high-power microwave applications. In the second section of this chapter, using a similar method, both miniature and reconfigurable CPW antennas are proposed. Due to the topology of folded CPW slot antennas, it is very challenging to mount semiconductor components on top of them, and as a result, widely-tuned/reconfigured CPW antennas are not available in the literature. Using liquid-metal bridges reconfigurable CPW antenna with a frequency range of 2.4–5.8 GHz is proposed and a miniature antenna with a miniaturization factor of 85% is also achieved. Third section of this chapter discusses a reconfigurable dual-band slot antenna whose both bands can be tuned independently. Discrete tuning ratio of 1.7:1 for each band and an overall coverage ratio of 3:1 (1.8-5.4 GHz) for the antenna is achieved using the liquid-metal capacitive loading technique. Forth and fifth sections both present quarter-mode SIW filters and antennas. While for the filter the same capacitive loading technique is used to achieve frequency tuning, for the antenna, a corner via post is reconfigured using the liquid metal for connection/disconnection.

Chapter IV is the conclusion and future work. The method disclosed in chapter II can be extended to more complex SIW circuits where more number of resonators are involved. Also continuous tuning of SIW antennas can be further studied using a modified version of the tuning technique. The quarter-mode SIW resonators proposed both in section II and III provide promising results and are very compact in comparison with full-mode SIW resonators. A more in-depth study is required to find compatible coupling methods for these resonators and to achieve higher order compact filters. Both the convention tuning method of section II and the liquid-based method of section III can be employed to achieve widely-tuned and ultra-compact

microwave filters and antennas. The liquid-based tuning method has some issues to be addressed and resolved before it's ready for commercialization. Actuation, reliability, repeatability, durability, and ease of integration are some important topics that need further in-depth attention as this is an emerging area in the microwave community.

2. NOVEL TECHNIQUES FOR SIW ANTENNA AND VCO TUNING USING SEMICONDUCTOR DEVICES*

In this chapter a tuning technique for SIW-based microwave antennas and VCOs is proposed. The method is based on loading the SIW cavity resonators using disconnected via posts. By connecting/disconnecting the via posts and employing different configurations of ON/OFF switches, different operating states are achieved. First, the method is developed and applied using a cavity-backed conventional SIW antenna. Then the technique is also employed and modified for miniature SIW antennas. Also, the application of this tuning method for SIW-based VCOs is proposed. For all cases, prototypes are fabricated and measured to validate the proposed designs.

2.1 A Reconfigurable SIW Cavity-backed Slot Antenna with One Octave Tuning Range

2.1.1 Introduction

To be compatible with the standards of today's wireless devices, the antenna solution can be one of the multiple-frequency, wideband or Reconfigurable Antennas (RAs). Because of the crosstalk due to the neighboring bands, the first two choices are less appealing compared to RAs. Also, the receiver filter design will be less complex

by benefiting from the frequency selectivity of the tunable narrowband antennas [24].

Because of capability to serve various frequencies at a time, ease of fabrication and compatibility with microwave integrated circuits, slot antennas are a perfect choice for tunable antenna design. In order to make these antennas reconfigurable, varactors, p-i-n diodes, and RF-MEMS switches have been used, while the first one offers analog tuning and the other two offer digital tuning [35–37]. In [35], a folded slot antenna with varactors across the slot is used to have a dual-band tunable response. In [36], using a triple slot structure and p-i-n diodes, three switchable frequency bands are achieved.

One drawback of slot antennas is their two-sided radiation pattern which makes them a weak choice for being used on an additional ground plane, such as the body of a vehicle, a Printed Circuit Board (PCB), or any other scattering object [38]. To eliminate the back side radiation, cavity backed slot antennas with high radiation performances appear to be more amenable. However, whether using a metallic reflector plane or a shallow cavity for this concept, complex fabrication process, intrinsic bulky size, and incompatibility with simple PCB techniques hinders their use as an alternative. For instance, White *et al.* demonstrated a shallow CBS antenna in which a varactor is placed across the slot in order to tune the antenna frequency response, where a tuning range of 1.9:1 is achieved. The cavity is machined into a block of aluminum and then filled with PTFE (r = 2.1) inside [38].

Recently, by the invention of Substrate Integrated Waveguide (SIW) circuits, achieving the same radiation performance of conventional CBS antennas along with the advantages of low profile, ease of fabrication, and compatibility with planar integration has become possible [14, 15, 39]. In [40], a tunable SIW-CBS antenna oscillator is proposed where a narrow tuning range of 180 MHz (fc = 10 GHz) is achieved by loading the cavity with a variable capacitor. Ref. [40] is the only tunable

SIW-CBS antenna found by the authors in the literature.

In this section, a new technique is used to tune a SIW-CBS antenna for a wide frequency range. This technique was first proposed by Sekar *et al.* [41] to tune SIW filters and is based on loading the cavity with different tuning posts. Each single post changes the field distribution inside the cavity. As a result, the magnetic fields around the slot will be perturbed, and the resonance frequency of the antenna changes. The tuning posts are controlled using high performance p-i-n diodes. By choosing different ON and OFF combinations of four tuning posts, six different states in the range of 1.1–2.2 GHz are achieved. Also, by loading the cavity antenna with the tuning posts, antenna miniaturization is achieved by a factor of 66%. When these posts are not connected to the bottom ground plane, they just load the antenna as a reactive element, and as a result, the antenna resonance frequency shifts down. The antenna itself is designed to work at 2 GHz. By inserting the posts inside the SIW cavity, the antenna frequency of operation is lowered to 1.2 GHz. This method also avoids the placement of any components on the radiating side of the CBS antenna. As a result, SIW-CBS antennas can have additional circuitry on their back side without affecting their radiation pattern.

2.1.2 The Tunable SIW-CBS Antenna

2.1.2.1 Antenna Structure

Fig. 2.1 shows the top and cross section views of the proposed antenna with the four tuning posts. As can be seen, the CBS antenna is constructed using a two-layer SIW structure to isolate the p-i-n diodes and the biasing circuit from the cavity antenna. The bottom substrate of height h_1 and dielectric constant of ϵ_1 with width W and length L is used as the cavity for the antenna and the top layer with thickness of h_2 and dielectric constant of ϵ_2 is used for implementation of the

biasing circuit. The cavity is utilized using the SIW technology, where periodic metal posts with diameter d and spacing b between the holes are used to form the cavity vertical walls. The top and bottom walls of the cavity are formed using the middle and bottom metal layers, respectively. According to [9], a thick substrate is used to minimize the conductor loss related to the cavity. To minimize the leakage from the spacing between the adjacent posts, two design rules $d/b \geq 0.5$ and $d/\lambda_g < 0.2$ are satisfied for the SIW cavity. At first, the dimensions of both the slot antenna and the cavity are set for the same resonance frequency. The cavity used is a rectangular cavity in which the dominant mode TE_{101} is excited. The dimensions of the cavity are then set using the following relations for the SIW cavity:

$$f_{101} = \frac{c}{2\sqrt{\epsilon_r \mu_r}} \sqrt{(\frac{1}{L_{eff}})^2 + (\frac{1}{W_{eff}})^2} \tag{2.1}$$

$$L_{eff} = L - \frac{d^2}{0.95.b} + 0.1\frac{d^2}{L} \tag{2.2}$$

$$W_{eff} = W - \frac{d^2}{0.95.b} + 0.1\frac{d^2}{W} \tag{2.3}$$

where c is the speed of light in vacuum and ϵ_r and μ_r are the relative permittivity and permeability of the substrate, respectively [10, 42]. Length l of the slot is set equal to be half of the slot-line mode wavelength λ_s which is defined as $\lambda_0/\sqrt{\epsilon_s}$, where $\epsilon_s = 0.5(\epsilon_r + 1)$ is the effective dielectric constant of the slot-line mode [38]. A Conductor Backed Co-Planar Waveguide (CB-CPW) line is used to excite the combination of the cavity and the slot antenna as a single resonance structure. The CB-CPW line is then connected to a microstrip line in order to realize the matching network designed for the tunable antenna as will be discussed later. The inner

Table 2.1: The Reconfigurable SIW-CBS Antenna Parameters.

L	66 mm	W	90 mm	L_s	28 mm	L_p	8 mm
d	1.5 mm	b	3 mm	h_1	3.2 mm	h_2	1.3 mm
d_s	1.3 mm	S	1.7 mm	W_m	9.5 mm	W_g	3.7 mm
L'	45.5 mm	L_g	4.5 mm	ϵ_{r1}	2.2	ϵ_{r2}	10.2

conductor and the gaps widths of the CB-CPW part (W_m, W_g in Table 2.1) are sized to provide a 50-ohm line the same as the microstrip line on the bottom substrate. All the relevant dimensions are summarized in Table 2.1.

The SIW-CBS antenna is designed to work at 2 GHz when it is not loaded with the posts. The posts have a miniaturization effect and they shift down the resonance frequency of the antenna. Fig. 2.2 shows the center frequency of the antenna for different number of loading posts. None of the posts are connected to the cavity top wall in this analysis. It can be seen that by inserting the posts (not connected to the bottom metal plane), the antenna resonance frequency shifts down. The total shift achieved due to locating the posts inside the cavity is ∼0.8 GHz that shows a miniaturization by a factor of 61%. This is computed using $[(\text{Area}_\text{c} - \text{Area}_\text{n})/\text{Area}_\text{c}] \times 100$, where Area_c is the area of the cavity top plane for a conventional antenna working at 1.22 GHz, and Area_n is the same parameter for the proposed antenna. The heights of the two antennas are assumed to be the same. This can be described by the capacitive loading effect of a disconnected via post. By adding the number of the posts, the capacitive loading effect increases. As a result, large frequency shift occurs. It is notable that this value for miniaturization does not include the effects of the biasing network and the diodes' parasitics which will be discussed later.

Another advantage of this method is that miniaturization is achieved without using any lossy component. As a result, no resistive loading effect is present at the lowest frequency compared to the other technique presented for tuning conven-

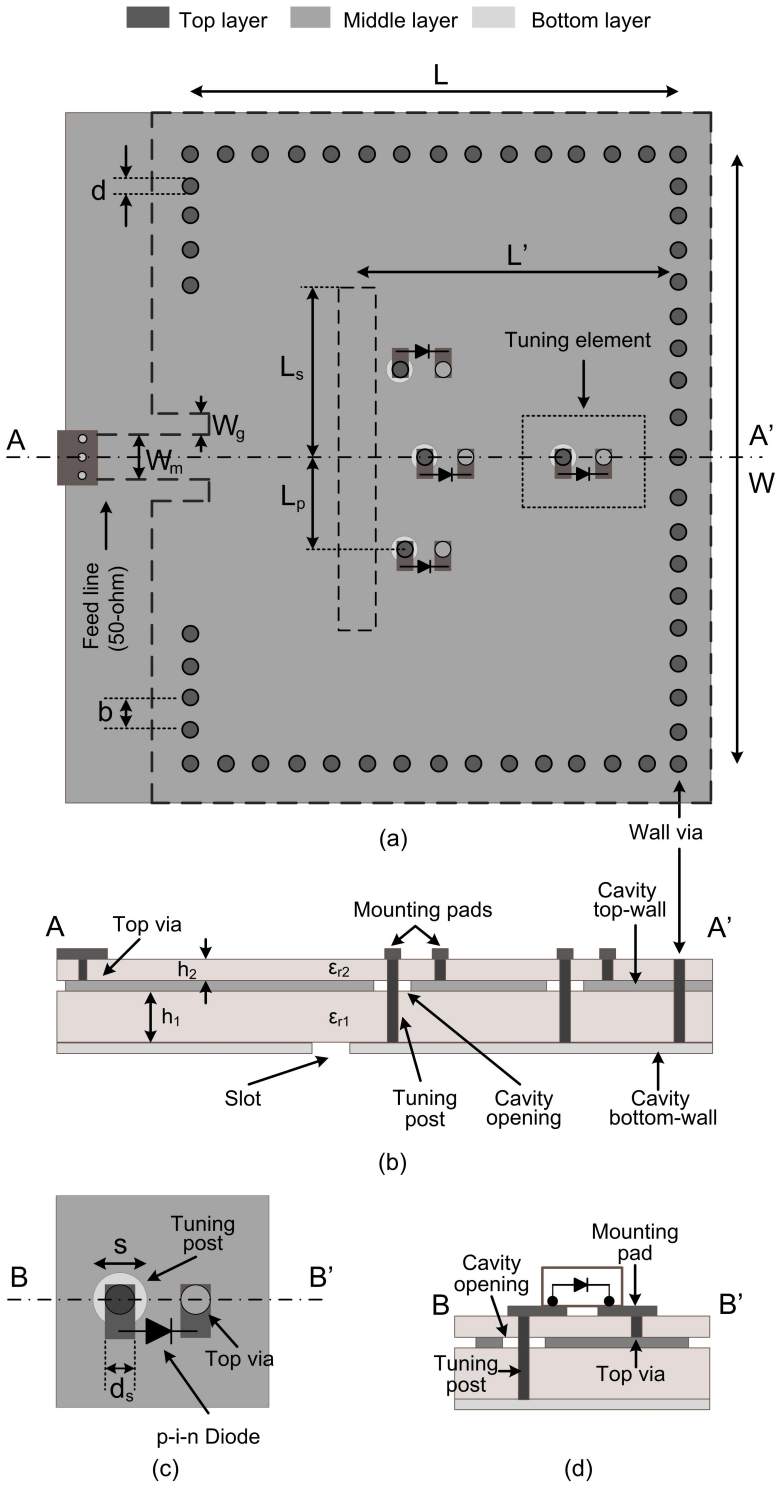

Fig. 2.1: (a) Top view of the proposed SIW-CBS RA. (b) A-A' cross section view of the structure. (c) Magnification of a single tuning element. (d) B-B' cross section view of the tuning element.

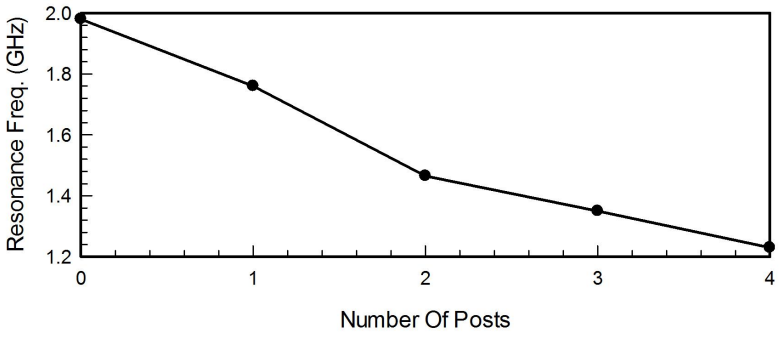

Fig. 2.2: Effect of the disconnected tuning posts on the operating frequency of the antenna.

tional CBS antennas in [38]. This improves the radiation efficiency of the antenna significantly at this operating band as will be discussed later.

2.1.2.2 Tuning Mechanism

To make the SIW-CBS antenna widely tunable, a novel method is proposed. Instead of directly loading the slot antenna with capacitance [35], or changing the length of the slot by using a switch across it [36], the field perturbation inside the cavity is used in order to tune the antenna. The idea is based on loading the antenna with a via post and then connecting it to and disconnecting it from the cavity top-wall using p-i-n diodes (Fig. 2.1). Fig. 2.3 shows both the E- and H-field distribution inside the SIW-CBS antenna loaded with only one via post, for the two conditions when the via post is disconnected (a), (b) and when the via post is connected (c), (d). As can be seen, by connecting the via post to the cavity top wall (middle metal layer in Fig. 2.1) the E-field distribution inside the cavity is perturbed. As a result of this manipulation of fields, the resonance frequency of the antenna is changed. As shown in Fig. 2.3 (b), (d), by comparing the vector magnetic fields in the cavity and around the slot, because of the H-field perturbation around the

connected via post, the area dedicated to the maxi-mum H-fields around the slot is smaller in (d), as a result the frequency is higher in this state. This can also be justified using the Maxwell's equations and the relation between the surface currents and H-fields, as in the ON-state, the surface currents detour a shorter path and the frequency increases. The E-field plots show a more tangible understanding of this phenomenon. By turning the via post ON, the white region (the maximum magnitude area for the E-field) becomes smaller and the frequency shifts to a higher value. Based on this configuration as a starting point, more via posts are added to the structure to increase both the tuning range and the number of states. Because of the concentration of fields around the slot antenna, the effect of the via posts (all switches turned ON) is 300% more than what has been achieved in [41] for frequency tuning, where the via post is used to tune a cavity resonator and so a multi-cavity SIW filter. Choosing the optimum position and also the number of the via posts will be described in the next subsection.

As shown in Fig. 2.1(c), a complete tuning element consists of one through metal via post (tuning post), one top via, two mounting pads, and a switching component which here is a high performance p-i-n diode. The connection between the through via and the cavity top wall (middle metal layer) is made using the switch. Whenever the switch is ON, the via post is connected to the cavity top wall, and manipulates the fields inside the cavity. Once the switch is turned OFF, the via post is disconnected and acts just as a loading capacitance, not perturbing the fields but lowering the frequency of the antenna. The permanent disconnection between the metal via post and the cavity top wall is guaranteed by etching circular slots with diameter S around the via posts, shown as the cavity openings in Fig. 2.1(d). The openings are relatively small in comparison with the wave-length at frequencies of operation. Thus, these do not affect the Q of the cavity since there won't be a considerable

leakage. Effect of the p-i-n diodes parasitics, as the limiting factor of the tuning range in this method are discussed in section 2.1.3.

2.1.2.3 Resonance Contours

In order to study the effect of the connected via post on the resonance frequency of the SIW-CBS antenna and the fields inside the cavity, the resonance frequencies for various locations of the via post inside the SIW-CBS antenna are found using a commercial High Frequency Structure Simulator (HFSS) [43], then the resulting resonance contours have been plotted in Fig. 2.4(a). Changing the placement of the tuning post alters the field perturbation inside the cavity. As can be seen in Fig. 2.4(a), the closer the via post to the center of the cavity and the slot antenna, the more frequency shift is observed. This is because the concentration of the fields inside the cavity is in the center and around the slot antenna. The contours in Fig. 2.4(a) show a huge resemblance to the electric field distribution of the SIW-CBS antenna plotted in Fig. 2.4(b). These two plots offer that greater resonance frequency shifts occur due to greater field perturbations, and greater field perturbations occur when the via post is closer to the maximum electric field or minimum magnetic field magnitudes. Similarly, moving the via post away from the cavity center and closer to the cavity side-walls results in a resonance frequency very close to the fundamental resonance frequency of the SIW-CBS antenna. This can be justified by assuming the SIW-CBS antenna as a parallel L-C resonator, with a resonance frequency of $f_0 = 1/2\pi\sqrt{LC}$. When the via post is connected to the cavity top-wall, surface currents are induced on its surface. As a result, it can be equivalently represented by a shunt inductance (L_p) [44]. Due to the additional inductance introduced by the via post, the new resonance frequency of the antenna is $f_0' = 1/2\pi\sqrt{L_{eq}C}$ where L_{eq} is $(L||L_p)$. The value of L_p is related to the magnitude of the electric fields at

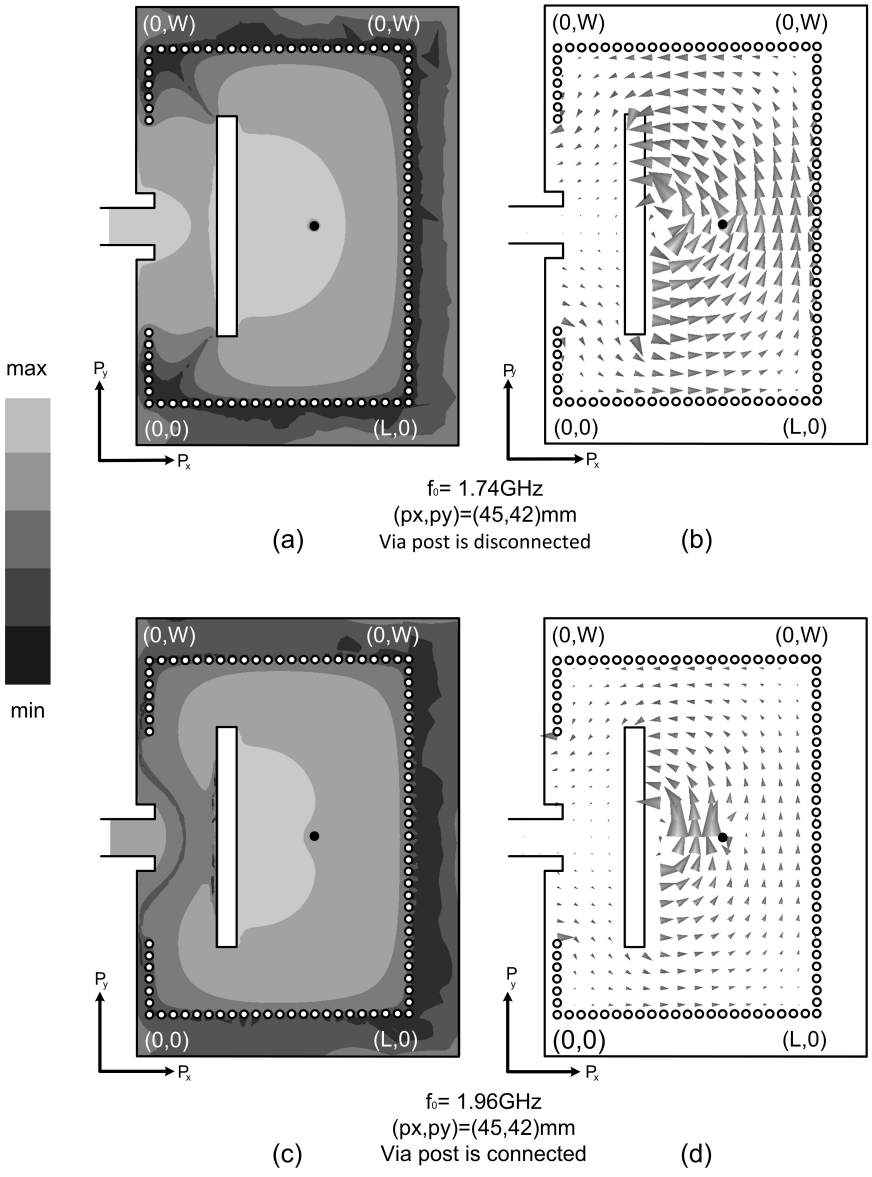

Fig. 2.3: Magnitude of electric field distribution and the vector magnetic field distribution inside the SIW-CBS antenna when (a), (b) the via post is disconnected, and (c), (d) when via post is connected.

the position of the via post [44]. At the cavity center, due to the maximum electric field, the shunt inductance of the via post is minimum. This results in the maximum possible frequency shift. The capacitive effect of the disconnected via post can be justified the same way. When the via post is not connected, it can be represented as a shunt capacitance, this time resulting in a decrease of resonance frequency. Looking at the contours, there is also a region behind the slot where the frequency is lower than that of the OFF state. Although by placing the via post in this position the tuning range may get wider, this causes poor matching of the slot to the SIW cavity. Also poor radiation performance occurs by putting the via post in this region because the via disturbs the coupling of fields to the slot antenna. As a result, putting the via post in this position is prohibited in the design of the tunable SIW-CBS antenna. Based on the relationship between the via post and the cavity resonance, the initial position for the four final via posts has been chosen. Then the optimum positions are found using the resonance contours and also the electric field distribution inside the SIW-CBS antenna.

2.1.2.4 Tunable SIW-CBS Antenna With Four via Posts

Four different via posts have been located around the maximum frequency shift contour to achieve different states and also the maximum possible tuning range. The performance of the antenna along with the inserted via posts is then studied in HFSS to achieve the highest possible tuning range when all the via posts are connected to the cavity top-wall. These four via posts are shown as P, Q, R1, and R2 in Fig. 2.5(a). Consequently, the SIW-CBS antenna can have $2^{(4-1)} = 8$ different possible tuning states. Where two of these states cannot be used as will be discussed. The ultimate number of states then will become six. The via posts P and Q are controlled separately and the other two vias (R1, R2) are turned ON and OFF together at the

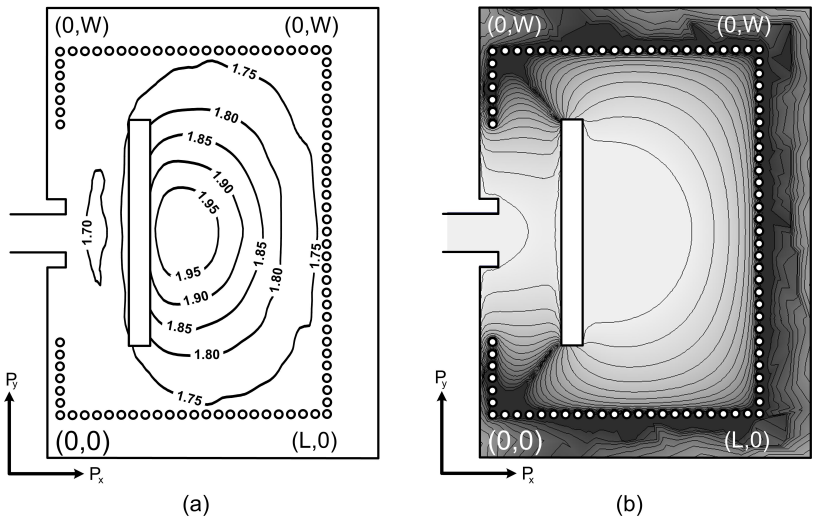

Fig. 2.4: Simulated resonance contours for a single connected tunning post for different positions inside the SIW-CBS antenna. (b) The electric field distribution with different magnitude region lines.

Table 2.2: Different Tuning State Via Posts' Configurations and the Via Posts' Locations.

Tuning states		**Via posts' locations**	
State	Configuration (PQRR)	Post	Location: (P_x, P_y in mm)
1	0000	P	(45,29)
2	0100	Q	(45,42)
3	1000	R1	(39,27)
4	0011	R2	(51,27)
5	1011	–	–
6	1111	–	–

same time. This is because the antenna has a symmetrical radiation pattern and manipulating the ground plane and/or the fields inside the cavity asymmetrically, ends up providing tilted radiation patterns. Therefore, maintaining the symmetry in the structure of the SIW-CBS antenna must be taken into consideration at all the tuning design steps. Obviously, it is also possible to have more tuning states by sacrificing the symmetry of radiation patterns. The positions of the via posts along with the possible six post configurations are shown in Table 2.2.

Fig. 2.5(a-f) show the electric field distribution inside the cavity for all the six tuning states, where state 1 is the state when no via post is connected (0000), and state 6 is the condition when all the via posts are connected (1111) to the cavity top-wall. As can be seen, the switches decrease the area dedicated to the maximum electric field region gradually in Fig. 2.5(a-e), where they totally eliminate the maximum electric field region in state 6. The connected via posts are shown as black circles while the disconnected ones are shown in white. The effects of the p-i-n diodes are taken into account by inserting their lumped element model.

Up to this point, the design steps have been limited to the change of the resonance frequency and the input impedance matching level of the SIW-CBS antenna in different tuning states has not been considered yet. Locating the via posts inside the cavity causes the antenna to be loaded either capacitively or inductively when the via posts are disconnected or connected, respectively. In both situations, the input impedance of the antenna is affected, and the antenna is not matched to the 50-ohms input impedance for all the tuning states. To achieve perfect impedance matching for the antenna over the entire tuning range, a matching network at the input port is necessary. Transforming the affected input impedance (setting the resistive part to 50-ohms when the reactive part is zero) to the required impedance (50-ohms) over one-octave tuning range requires a complex matching network as the effect of the via posts and the loading changes at different frequencies of operation. Alternatively, it is more convenient to change the imaginary part to zero (compensation for the loading effect of the posts) at the frequency where the real part is 50-ohms inherently (setting the reactive part to zero when the resistive part is 50-ohms) using a series reactance at the input of the antenna. Inductive or capacitive matching can be employed for positive or negative input reactance.

In this case, it was found necessary to match the SIW-CBS antenna using the

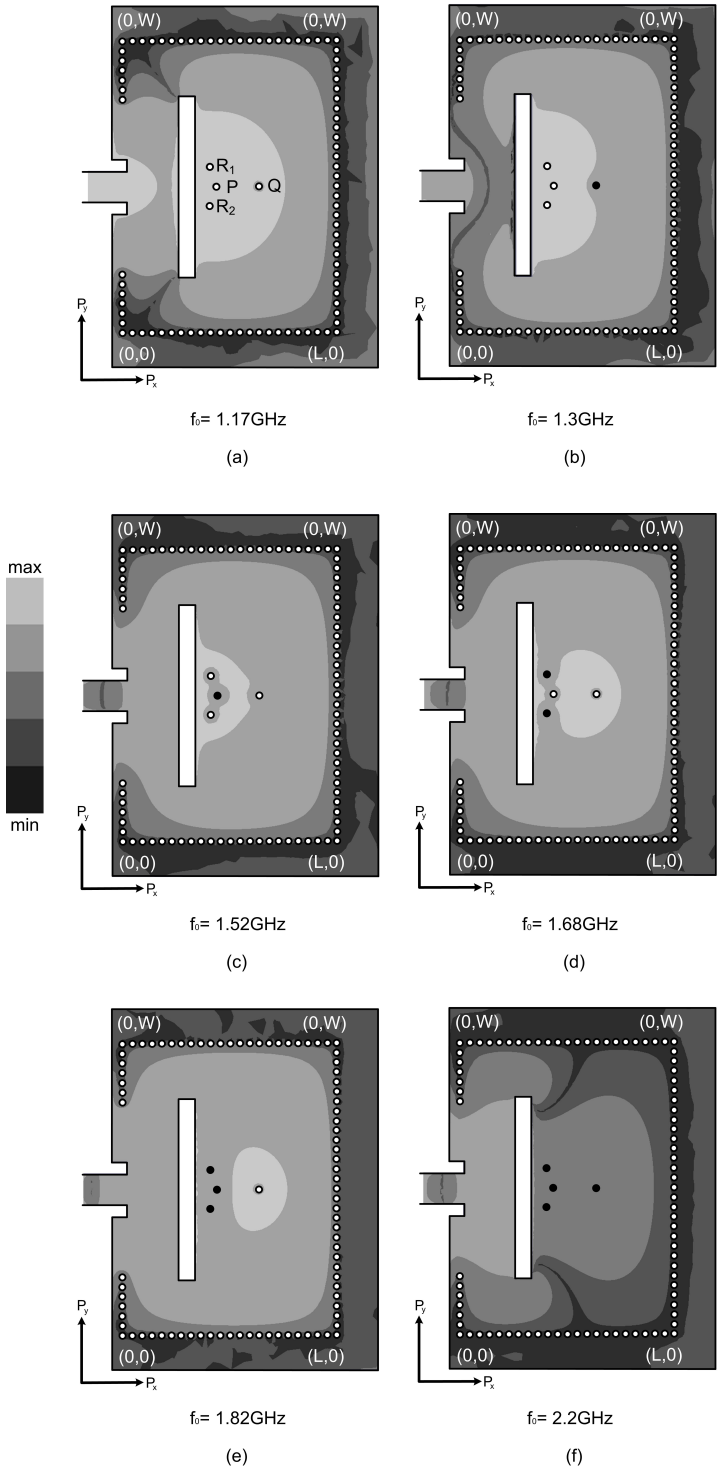

Fig. 2.5: Magnitude of electric field distribution inside the SIW-CBS antenna for different configurations of via posts shown in Table II. (a)-(f) refer to states 1-6, respectively.

series inductive matching. The value of the required inductor in series with the transmission line changes with frequency as the antenna is tuned. This value has to be chosen to eliminate the imaginary part of the input impedance of the antenna in all the states while the real part is always near 50-ohms. Thus, an average value of 2.2 nH over the tuning range has been chosen by which near perfect matching can be achieved for all of the tuning states except state 7 (switches R1,2 and Q are ON), since the reactive part for this state does not stand within the range of the other states reactive part value. For instance, the input impedance of the antenna with and without the matching inductor is shown in Fig. 2.6 for tuning state 5. The ultimate design has 6 tuning states, equally fulfilling the whole tuning range (1.1–2.2 GHz). Two states are eliminated here, one has poor matching problem and the other (P and Q are in the ON state) has a resonance frequency very close to state 4. Fig. 2.7 shows the resonance frequencies of the different tuning states along with their impedance matching level with and without the 2.2 nH matching inductor. As can be seen, this method causes a slight change in the resonance frequency of the antenna (due to the nature of reactive matching) which can be neglected (Maximum error of 3%). By adding the matching inductor, the matching level for all the states improves to a level better than -19 dB.

2.1.2.5 Effects of the p-i-n Diodes as the Switching Elements

To realize a reconfigurable antenna, high performance BAP65LX p-i-n diodes from NXP semiconductors have been used as the switching elements [45]. The non-ideal diodes have additional loading effect on the performance of the antenna which needs to be taken into account. This effect can be modeled by using the RF equivalent circuit of the diodes provided by the manufacturing company. The model used in the full-wave simulations for this design is shown in Fig. 2.8(a). As can be seen,

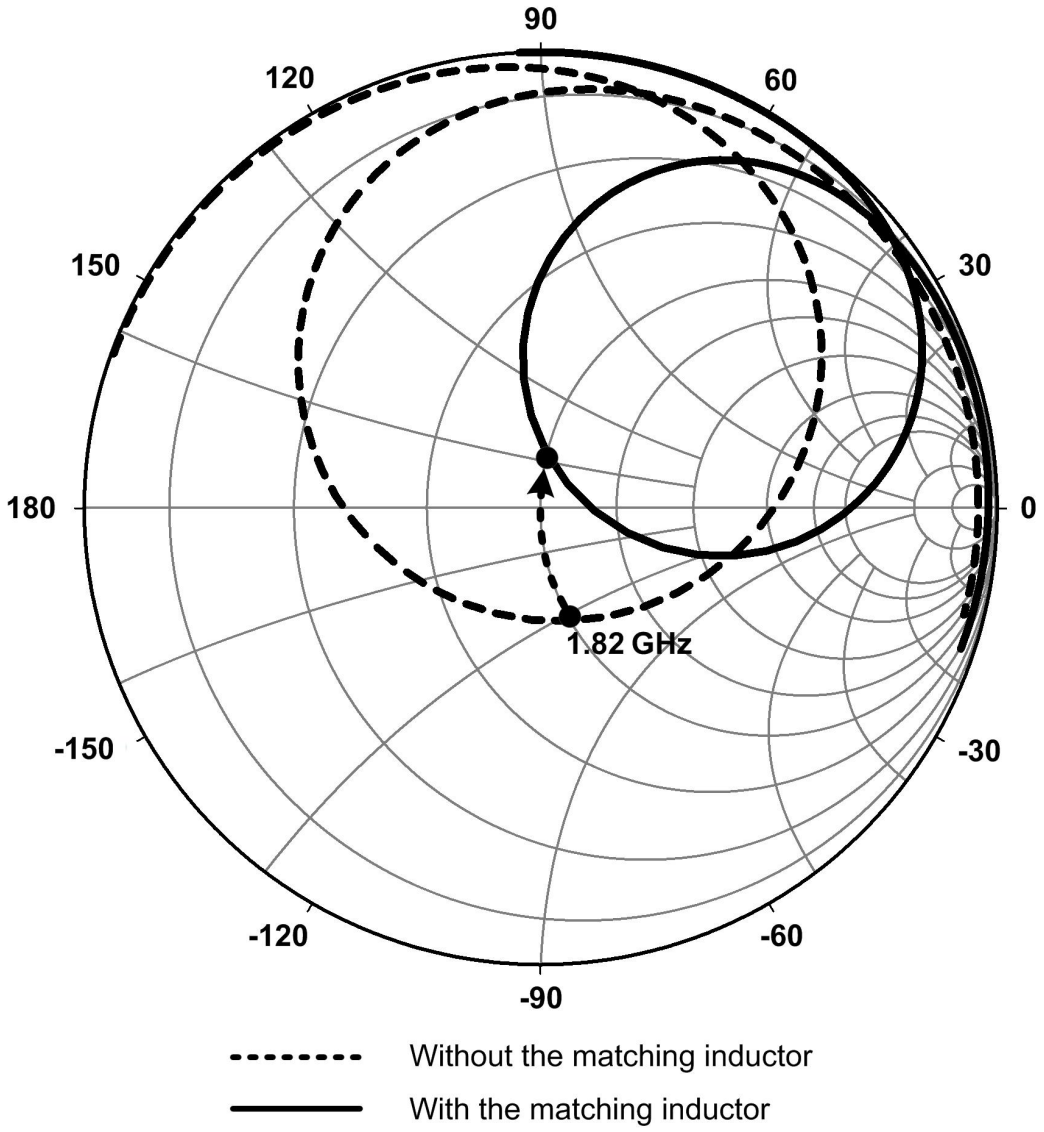

Fig. 2.6: Input impedance of the antenna working at state 5, before and after employing the matching inductor.

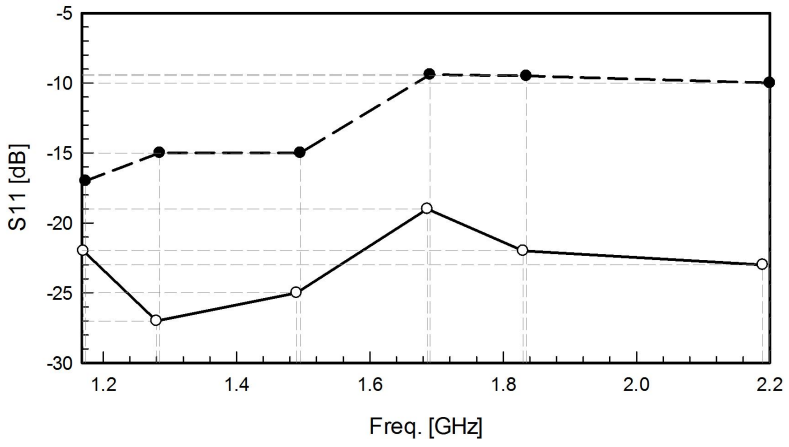

Fig. 2.7: The simulated input impedance matching level for the different working states of the antenna, without the 2.2 nH matching inductor (dashed line) and with the matching inductor (solid line).

the resistance of the diode is the most limiting factor as it introduces loss when the switch is in the ON state. In addition the diodes have notable capacitive (C_d) and inductive loading (L_p) effects as well. Rs and the C_d come from the electric properties of the diode junction in ON and OFF states and L_p models the packaging inductive effect [46]. Although these values may not seem to be very important when one switch is being used, they become crucial in the proposed antenna, where more than one switch is being used for most of the states. As a result, the model shown in Fig. 2.8 has been used to take these effects into account. The resistive part of the model affects the matching of all different states except the first state where no switch is in the ON state. This effect is shown in Fig. 2.9 where the matching level of the different states is shown for different values of diode resistance. In order to match all the states with p-i-n diodes ON, the gap length and width of the GCPW section of the feed line and the diameter of the tuning vias need to be adjusted. The matching inductor value discussed earlier, and all the dimensions provided in

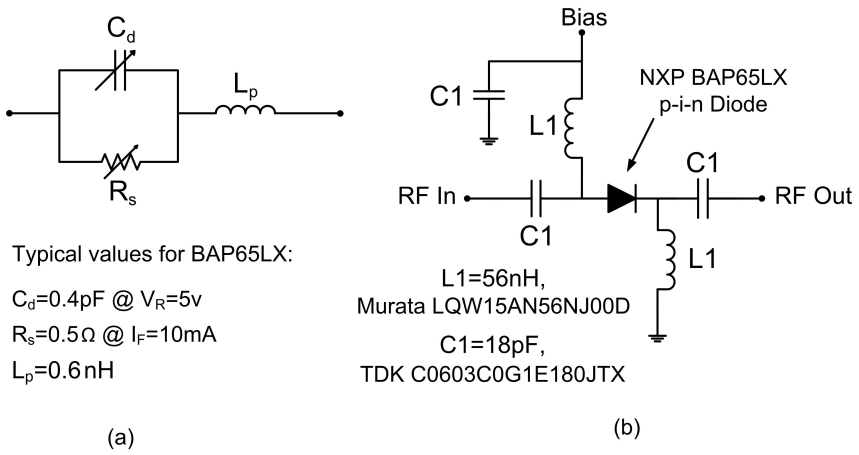

Fig. 2.8: (a) Equivalent RF circuit of the p-i-n diode, (b) p-i-n diode biasing network.

Table 2.1 are found at the presence of the diode model in Fig. 2.8(a). On the other hand, the reactive parts of the diode model cause a shift (Δf) in the initial resonance frequency of the antenna (f_i). The shift ratio stays roughly constant in all states. The frequency shift in the sixth state is due to the packaging effects of the diode, represented with the inductance L_p in the diode model (Fig. 2.8(a)). This is a constant shift, regardless of the ON and OFF state of the diode. Fig. 2.10 shows this shift versus different operating states of the antenna. Therefore, the resistive loading causes the matching to be poor and makes the design more complex and the reactive loading degrades the tuning ratio by 11%.

2.1.3 Fabrication, Measurement, and Discussion

2.1.3.1 Realization of the SIW-CBS Tunable Antenna

A prototype of the SIW-CBS antenna is fabricated based on the parameters given in Table 2.1 (Fig. 2.11). Two different Rogers substrates are used for the main layers of the structure, where the top layer (substrate layer) is the Rogers RT/Druid 6010 ($\epsilon_r = 10.2$), and the bottom one (Cavity layer) is the Rogers RT/druid 5880

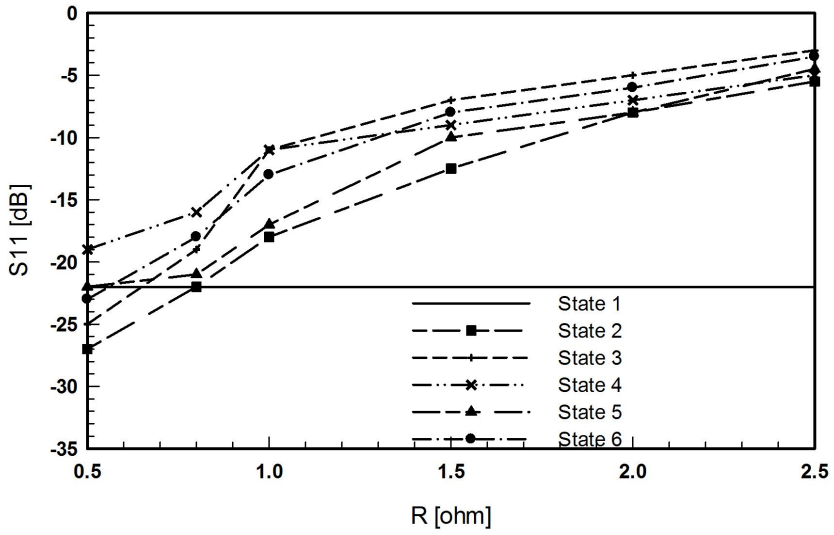

Fig. 2.9: The simulated return loss for different values of diode resistance at all the operating states.

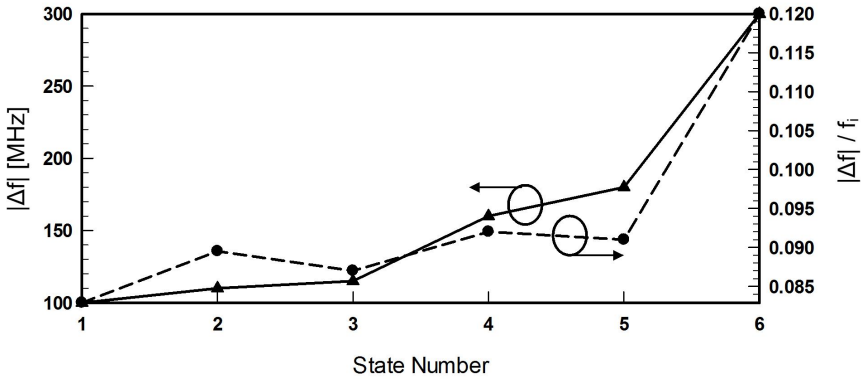

Fig. 2.10: Operating frequency shift and its ratio at different states due to the reactive loading effect of the p-i-n diodes.

($\epsilon_r = 2.2$). The first has been used for the top layer of the antenna as it is a reliable substrate for soldering components on, however, the latter is suitable for passive microwave structures due to its low loss ($tan\delta = 0.0004$) [47]. The mounting pads connecting the diodes to the through and top vias, and the biasing circuit are etched on the upper side of the top layer, and then the cavity top wall with the openings is etched on the other side of this layer. At this step, the top vias connecting the middle metal plane (ground plane of the antenna) and the biasing circuit are drilled in the upper substrate. The ground plane is brought to the upper side of the top layer using the same top vias for SMA access. Next, the cavity bottom wall along with the 50-ohms feed line and the slot are etched on the backside of the bottom substrate, while the other side is totally removed. The backside of the top substrate is then bonded to the upper side of the bottom substrate using the Rogers RO4450B pre-preg material ($\epsilon_r = 3.3$, $h = 0.09mm$). At the end the through metalized via holes are drilled as the walls of the cavity and also the tuning via posts through the entire structure. High performance p-i-n diodes are then soldered onto the mounting pads. A circuit similar to the one shown in Fig. 2.8(b) is employed as the biasing network of the p-i-n diodes. The value of all the DC-block capacitors used is 18 pF, and the value of all the RF-choke inductors used is 56 nH. These values are selected such that they ensure the maximum DC and RF isolation between biasing circuit and the SIW-CBS antenna at all operating frequencies. A 2.2 nH surface mount inductor is used in series with the microstrip line at the feeding point as the matching inductor. 3D Full-wave simulations verify that the pre-preg material and the biasing circuit's effects on the performance of the antenna are negligible.

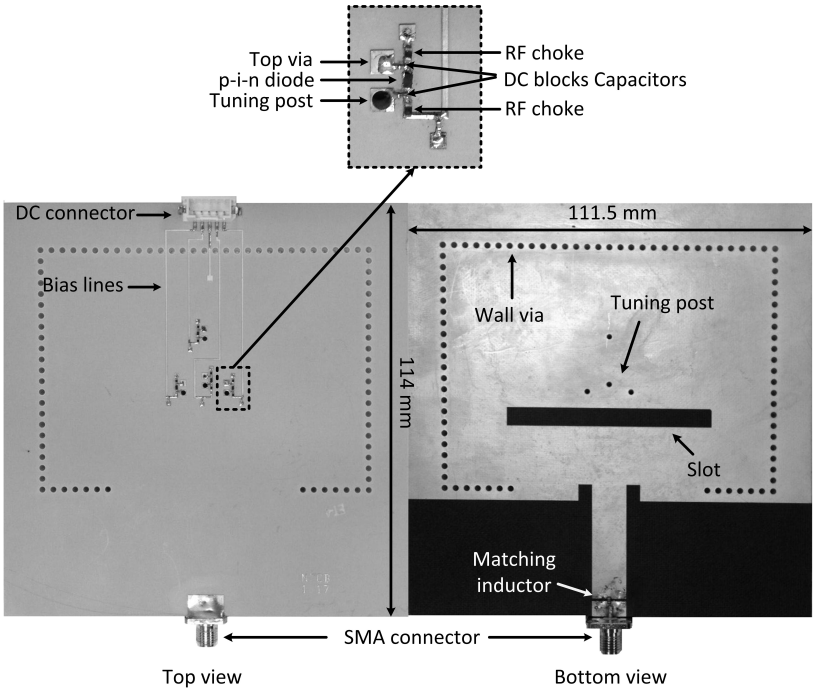

Fig. 2.11: Fabricated 1.1–2.2 GHz tunable SIW-CBS antenna.

2.1.3.2 Experimental Results

The input reflection coefficient of the fabricated antenna for all the six states is measured using an Agilent N5230A calibrated vector network analyzer (VNA). Fig. 2.12(a) and (b) show the simulated and measured results for all the six states, respectively (states are as described in Fig. 2.5). As can be seen, a relatively good agreement is observed between the simulation and measured results. The comparison between the simulation and measured results show no or little difference for the resonance frequencies (Maximum error of 2% at third and fifth states). There is also some difference between the matching levels of the simulated and measured results. This can be justified by the tolerance in the exact dielectric constant value and thickness of the substrates, errors in the thickness of the pre-preg material, fabrication errors such as the misalignment of the two boards in the connection process,

variations in via diameter, soldering and parasitic effects of the SMA connector and other components, and the SMA transition loss which was not taken into account in the simulations. Nevertheless, comparing the simulated and measured results shows a good agreement (with a maximum error of 2%) where matching better than 15 dB for all six states is achieved along with an octave tuning range. The 10-dB bandwidth of the antenna varies from 1% to 1.6%. This bandwidth variation is due to the change in the total capacitive loading of the switches. In the last state, the capacitive loading of the vias and the switches is at its minimum value, thus the bandwidth degradation will be smaller. On the other hand, in the first state where the capacitive loading is at its maximum value (all the switches are OFF), the largest bandwidth degradation can be seen. The same effect can be seen in the literature for the case where a capacitive load is used across the slot in the conventional method of tuning slot antennas [38].

As can be seen in Fig.2.12(b) the measured lowest frequency of the antenna is located at 1.12 GHz which shows more shift due to additional parasitics. As a result, the final miniaturization factor of the antenna using the formula provided earlier is 66%. This is achieved by comparing the fabricated antenna to a conventional CBS antenna working at 1.12 GHz.

The radiation characteristics of the prototype antenna are then measured using a standard anechoic chamber for three of its frequency states. The measured Co- and Cross- polarized far-field radiation patterns of the antenna are shown in two principal cut planes in Fig. 2.13(a), (b), and (c) for the states 1, 4, and 6, respectively. The similarity of the radiation patterns at resonance frequencies is comparable in both E- and H- plane. As can be seen, the antenna shows directive and near symmetric patterns which is common among all kinds of CBS antennas. The polarization of the antenna is linear in all the states and pattern purity (i.e. the difference between co-

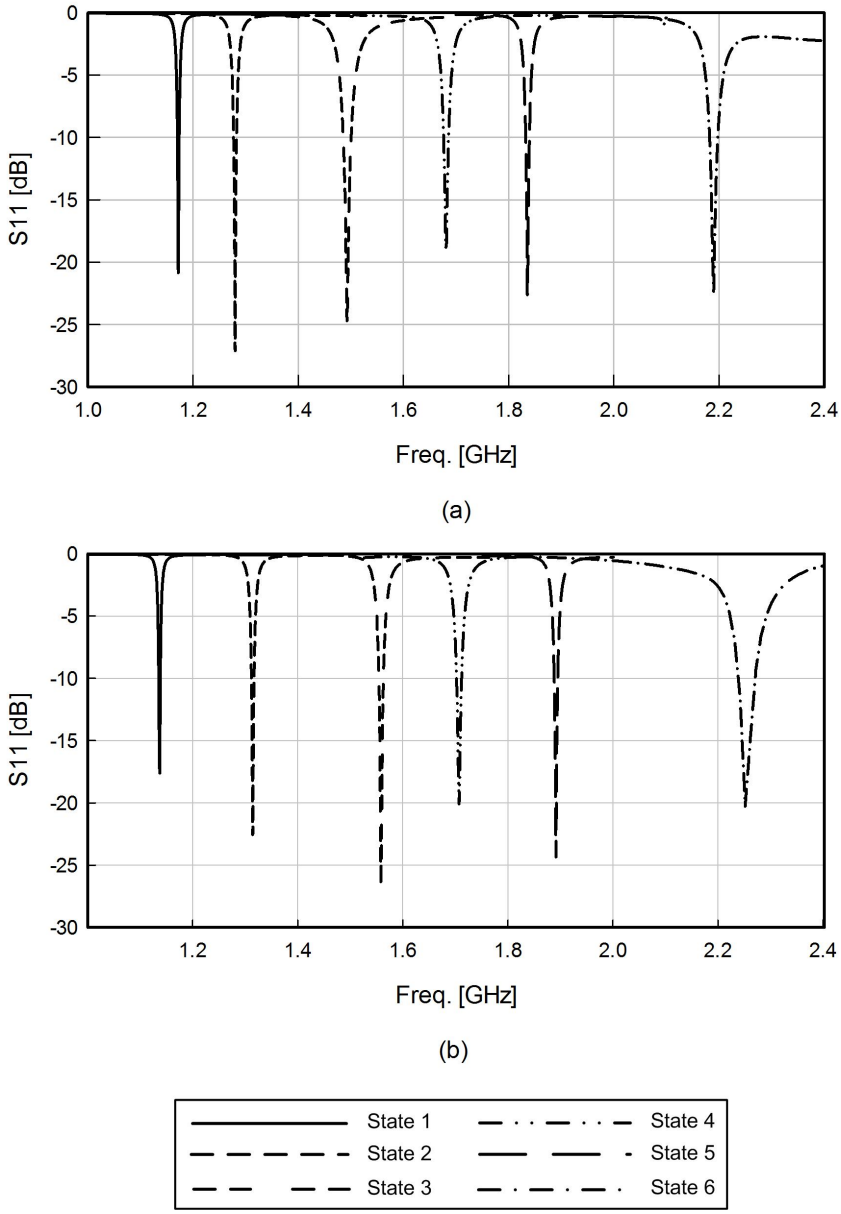

Fig. 2.12: (a) Simulated and (b) measured input reflection coefficients of the reconfigurable SIW-CBS antenna.

and cross- polarized levels) is better than 18 dB in all states. The front-to- back ratio is as low as 5 dB in the first state, 10 dB in the second state and as high as 20 dB in the sixth state. The reason for low front-to-back ratio at the first state is because the cavity size designed to work at 2 GHz, thus the performance of the cavity at 1 GHz is not as well as the one around 2 GHz (the cavity at 1 GHz is electrically small). The measured maximum gain of the antenna is 0 dB, 2.2 dB, and 5 dB at states 1, 4, and 6 respectively. The reason for lower gain at lower frequencies is the same as the reason of the low front-to-back ratio. However, due to the special nature of all the cavity-backed slot antennas and the fact that they can be mounted on any ground plane and metal surface, the degradation in front-to-back ratio, gain and similarity of E- and H-plane patterns can be solved by employing a bigger ground plane without any change in the impedance matching of the antenna. The ripples mainly seen in the back-side part of the E-plane radiation patterns are due to scattering from the components, and bias lines located at the back side of the antenna. However, the level of the received power at these angles is lower than -8 dB due to the nature of the antenna and its high front-to-back ratio.

The measured efficiency at state 1, state 4 and state 6 is 71%, 78%, and 75%, respectively. The low efficiency of the lower bands of the antenna is due to the topology and the reduction of its electrical size that occurs because of the loading effect of the disconnected vias. The contribution of p-i-n diodes to loss increases as the number of switches increases. As a result, efficiency decreases as the number of the switches increases. This is because the dissipated power in the resistive part of the p-i-n diodes increases. The reduction of the electric size is at its maximum value at the first state and the sole responsible for lower efficiency at this state. On the other hand, the switch loss is at its maximum value at the sixth state and the sole responsible for the lower efficiency value at this state. At state 4, however,

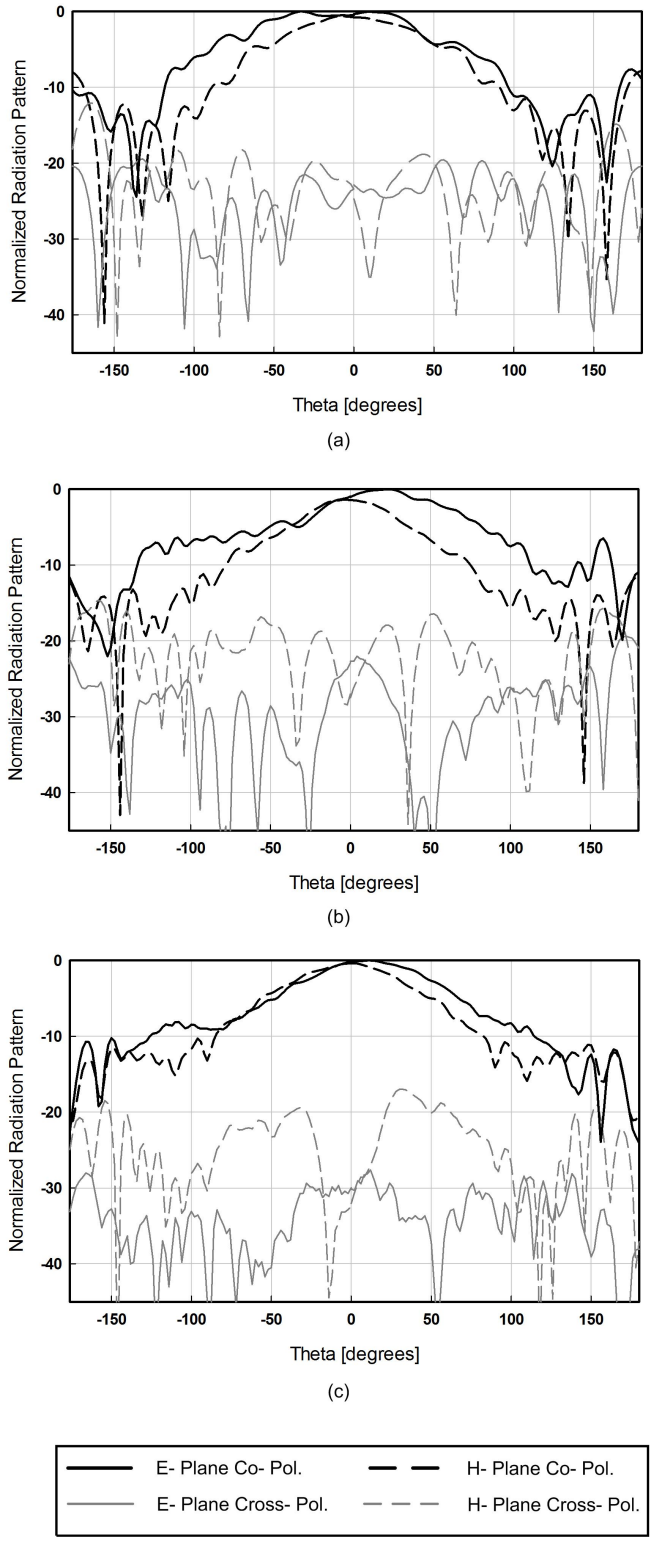

Fig. 2.13: Measured radiation pattern of the antenna at (a) first state (1.12 GHz), (b) fourth state (1.72 GHz), and (c) sixth state (2.27 GHz).

both the electrical size reduction and switch loss are affecting the efficiency of the antenna where none is at its maximum. As a result, a higher efficiency at this state is observed. The effect of resistive part of p-i-n diodes on efficiency observed is much less than the same effect when a varactor placed directly in series across the slot antenna. As the simulations show, the largest loss contribution is due to the resistive part of the p-i-n diodes (simulated efficiency is 88% at state 6 when ideal switches are used), after that the pre-preg material loss and finally the metal and dielectric losses are dominant. The ohmic loss of the inductor is negligible in comparison to the mentioned ones.

2.1.4 Conclusion

A new technique for designing reconfigurable SIW antennas is proposed and is successfully applied to design a SIW-CBS antenna with an octave tuning range. The reconfigurability of the antenna is achieved by inserting four via holes into the center of the SIW cavity by which the field distribution of the antenna alters in when each via hole connects top and bottom walls of the cavity through p-i-n diodes. In addition, when all the vias are disconnected, due to the reactive loading effect of the disconnected vias, a miniaturization by a factor of 66% is observed. Four identical p-i-n diodes are used to connect the via holes to the ground plane of the antenna. A prototype of the SIW-CBS antenna is fabricated and measured. The measurement results show good matching along with low cross polarization levels and radiation pattern similarity for all the states. To the best of authors' knowledge this was the first demonstration of a SIW-CBS tunable antenna with one octave tuning range and also the technique used for antenna tuning.

2.2 A Miniaturized Switchable SIW-CBS Antenna Using Positive and Negative Order Resonances

2.2.1 Introduction

Tunable slot antennas are widely used in various applications [24]. However, despite their wide tuning ratio, they suffer from the drawback of two-sided radiation pattern. As a good alter-native to slot antennas, same tuning methods have been applied to Cavity Backed Slot (CBS) antennas due to their high gain and one-sided radiation pattern. Using a varactor across a slot on top of a conventional cavity, a tuning ratio of an octave is achieved in [38]. This design seems to have both the advantage of tuning and one-sided radiation pattern, but at the same time, it is not compatible with simple PCB fabrication process. SIW structures are then the solution to this problem. However, both CBS and SIW-CBS structures have one drawback in common; conventional miniaturization techniques for standard slot antennas cannot be applied easily to any of them due to the presence of the cavity. One remedy to this problem is introduced in [48], where miniaturized SIW-CBS antennas are introduced by using a CRLH slot on top of a SIW cavity. However, this structure is not compatible with conventional tuning methods for CBS antennas. As a result, finding a new way to make this miniaturized antenna tunable seems to be a good solution for the demand of tunable small antennas with one-sided radiation pattern.

In this section, a new method for switching the negative order resonance of a miniaturized CRLH SIW-CBS antenna to the positive one is introduced to increase the antenna tuning range. The method is based on loading the antenna with tuning posts where by connecting these posts to the ground plane of the cavity, the resonance order of the antenna can be changed from negative to positive. Also, by locating

the posts inside the cavity in the disconnected condition (negative order resonance), additional miniaturization is achieved. Realization of the antenna using this method along with antenna performance is presented.

2.2.2 The Tunable Miniaturized SIW-CBS Antenna

2.2.2.1 Antenna Structure

Fig. 2.14 shows the schematic top and side view of the proposed antenna. As can be seen, the antenna employs a two-layer substrate structure in which the bottom layer (Rogers RT/duroid 5880) with height of $h_1 = 0.508mm$ and dielectric constant of $\epsilon_1 = 2.2$ is used for the cavity of the antenna and the top substrate (Rogers RT/duroid 6010) with height of $h_2 = 0.254mm$ and dielectric constant of $\epsilon_2 = 10.2$ is used for isolating the biasing circuit from the antenna. The biasing circuit is then etched on the upper side of the top dielectric layer (biasing layer). These two substrate layers are bonded to each other using a pre-preg material (Rogers RO4450B) with height of 0.09 mm. As the 3D full-wave simulations show, the effect of this layer on the performance of the antenna is negligible. There are four different tuning posts used in order to change the resonance frequency of the antenna. The permanent disconnection of these tuning posts from the cavity top wall is achieved using the cavity opening annular slots with a diameter of 0.9 mm as shown in Fig. 2.14(b). As the antenna has only two different tuning states, all the tuning posts are connected to each other on the biasing layer. Using a tuning element shown in Fig. 2.14, these four posts are connected to or disconnected from the cavity top-wall. The feed line of the antenna is placed on the cavity bottom-wall as shown in Fig. 2.14. In order to achieve matching for both bands, parameters Wg and Wm need to be adjusted. The ground plane is brought up to the biasing layer using the top posts for SMA access.

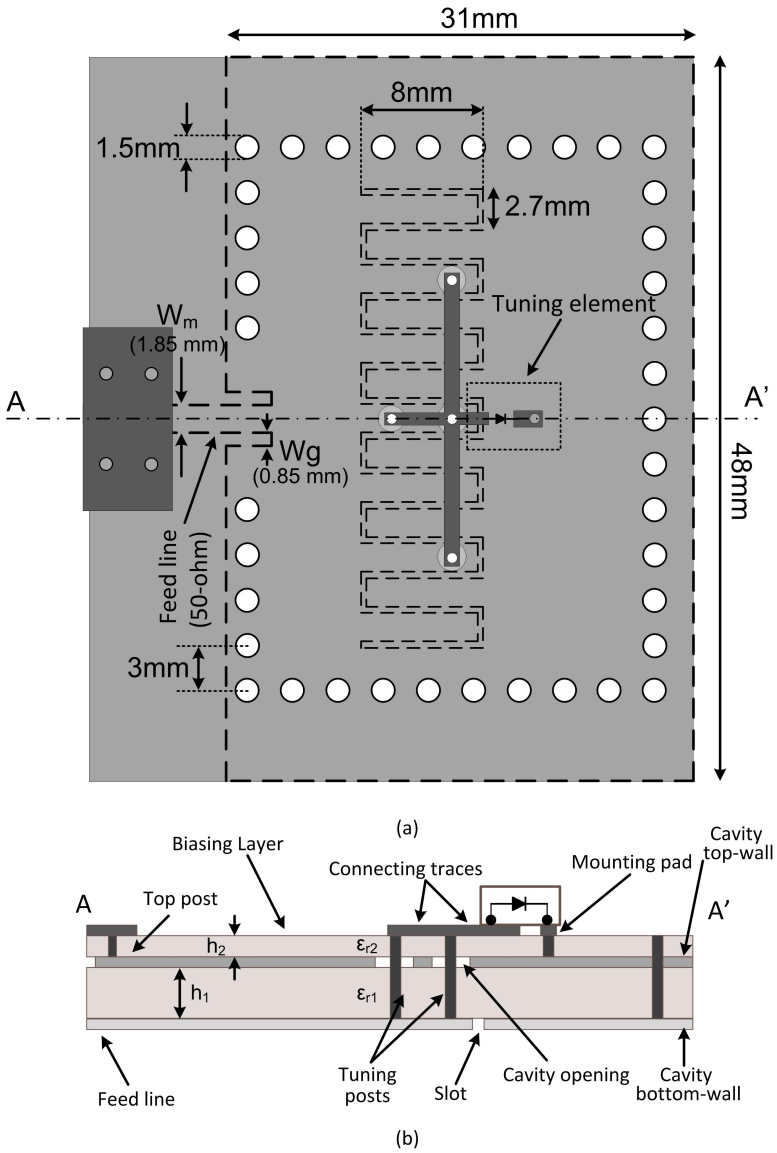

Fig. 2.14: (a)top view of the proposed SIW-CBS switchable antenna. (b) A-A' cross section view of the structure.

2.2.2.2 Antenna Miniaturization

The conventional SIW-CBS antenna with the same size but the rectangular slot works at 4.5 GHz. Using the CRLH structure technique described in [48], the frequency shifts down to 3.3 GHz while the antenna is not loaded with any tuning post. The tuning posts have a miniaturization effect as they shift down the frequency of the antenna due to their reactive loading effect. The resonance frequency of the antenna with the CRLH structure at the presence of the disconnected posts occurs at 1.83 GHz. The miniaturization ratio achieved by the antenna employing just the CRLH structure is 30% while the miniaturization is increased to 77% by inserting the disconnected posts.

2.2.2.3 Antenna Performance and Measurement Results

The proposed antenna shown in Fig. 2.14 is fabricated as shown in Fig. 2.15(a), and (b). The input matching and the radiation patterns of the antenna at both operating states are measured. High performance p-i-n diodes (SMP1352-079LF from Skyworks) are employed as switching elements where 18 pF capacitors and 70 nH broadband conical inductors are used for the biasing of the diode. Fig. 2.15(c), and (d) show the simulated and measured reflection coefficients of the proposed antenna for both bands. The measured frequencies for the first and second bands are 1.83, and 4.93 GHz, respectively. The tuning ratio is then 2.7. The frequency error between simulated and measured values of reflection coefficient at state 1 is 2.4% where for state 2 this value lowers down to 0.4%. The discrepancy seen between the simulated and measured results can be justified by the errors in fabrication process, the model used for the diode and other components, and the errors in the dielectric constant numbers. The parasitics effects on two states are different since one is a negative order resonance and the other is a positive order one. In the measured results, the

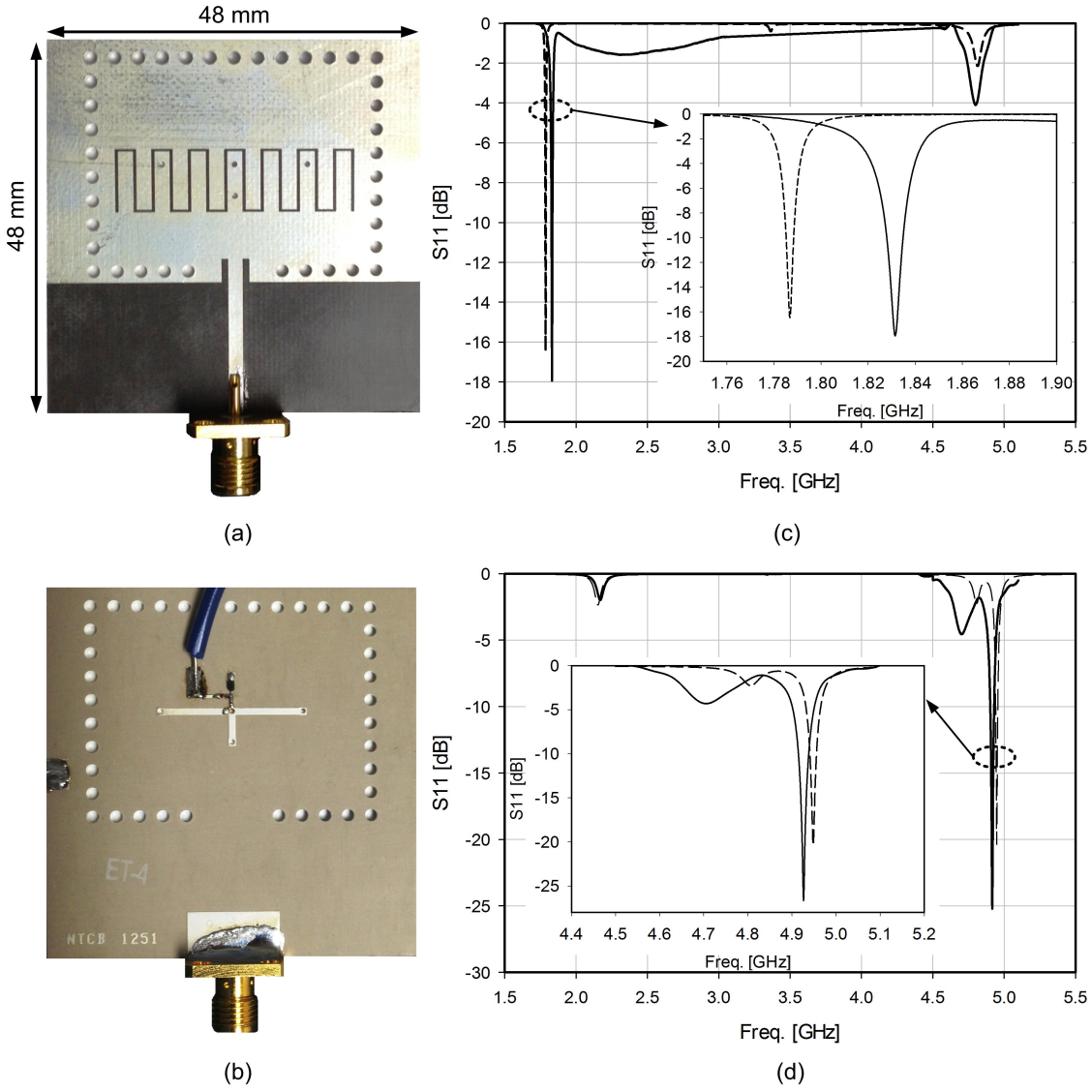

Fig. 2.15: (a) Fabricated prototype top view. (b) Fabricated prototype bottom view. (c), and (d) Measured (solid line) and simulated (dashed line) reflection coefficient of the antenna in states 1, and 2, respectively.

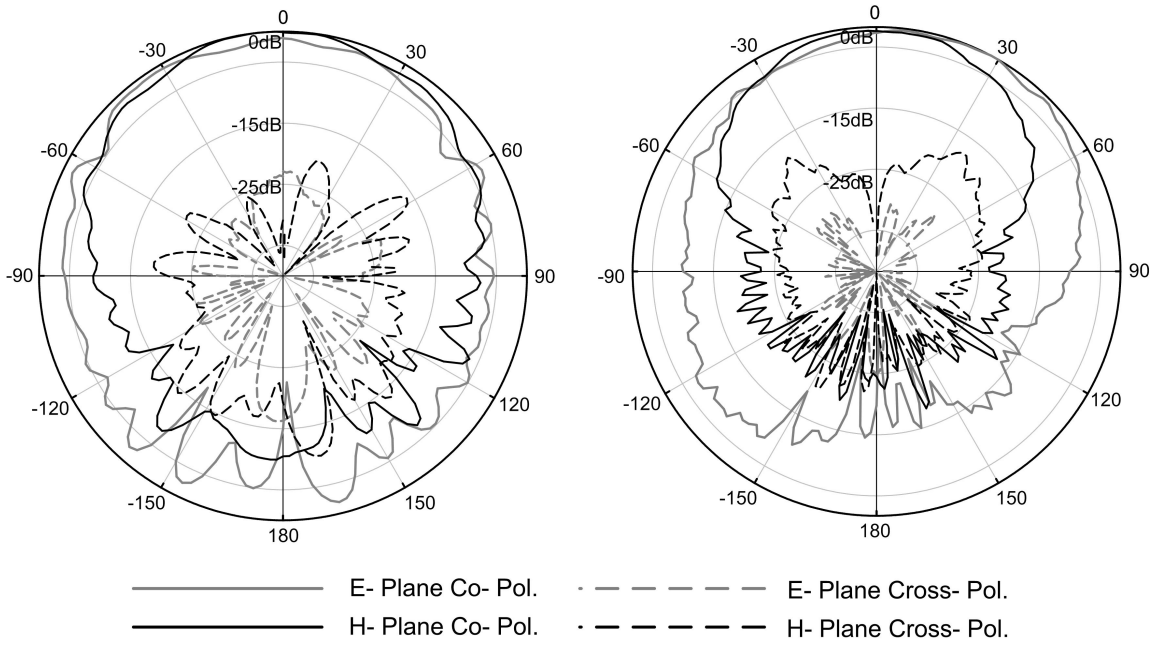

Fig. 2.16: Normalized radiation patterns of the antenna in (a) State 1, and (b) State 2.

1st state is shifted up due to the additional parasitics where the 2nd state is shifted down because of the same parasitics. The measured radiation patterns are shown in Fig. 2.16 for both states. The polarization of the antenna is linear at both bands and pattern purity (i.e. difference between the cross- and co- polarized levels) better than 16 dB is measured. The pattern for both bands is one-sided with a front-to-back ratio of 9 dB, and 15 dB at states 1 and 2, respectively. The measured maximum gain of the antenna is -4 dB, and 3 dB at states 1 and 2, respectively.

2.2.3 Conclusion

A new technique for tuning or switching the operating frequency of SIW-CBS antennas is introduced. Using this technique and a CRLH structure 77% of miniaturization is achieved. Antenna performance and details about the antenna structure are discussed.

2.3 A Tunable Quarter-mode Substrate Integrated Waveguide Antenna

2.3.1 Introduction

Substrate integrated waveguide antennas are well-known for their one-sided and high-gain radiation characteristics. However, the miniaturization methods of conventional planar antennas cannot be applied to them, which results in bulky antennas. One method to achieve miniature SIW cavity-backed slot antennas is to use the metamaterial-inspired negative order resonances of a SIW slot antenna [48]. While this method results in miniature antennas with the same radiation characteristics, tuning these antennas has been shown to be a challenging task. To resolve this issue, [49] proposes a metamaterial SIW CBS antenna with two operating states of 1.83 and 4.93 GHz using connected/disconnected via posts. Also, in [50], the same type of antenna is tuned using varactor diodes but for a limited range of 23% (4.13–4.5 GHz).

Recently, it is shown in [51] that by bisecting a SIW cavity on its two fictitious magnetic walls, a QMSIW antenna can be formed, by which a linear polarized leaky-based one-sided radiation pattern is achieved at the TE_{101} mode of the cavity. This results in an ultra-miniature antenna with a one-sided radiation pattern. Since this antenna is not based on a cavity-backed radiating slot, the above mentioned tuning techniques for SIW-based slot antennas are not applicable here. Therefore, finding a method to tune its frequency seems to be a good remedy for the demand of small tunable antennas with one-sided radiation pattern.

In this section, a new method to continuously tune a QMSIW antenna using varactor diodes is proposed. By employing a back-to-back varactor configuration, the linearity of the antenna is also improved [52]. The antenna shows a one-sided radiation pattern over the entire tuning range. Compared to the previous works in the area of miniature tunable SIW one-sided high-gain antennas, this antenna shows a

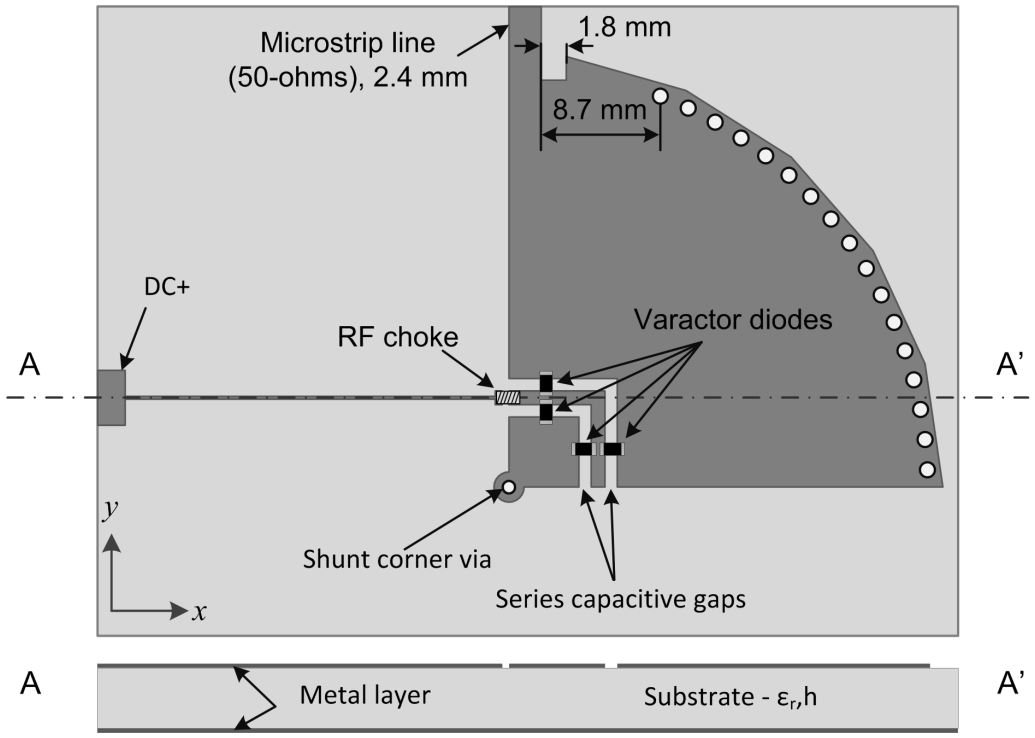

Fig. 2.17: Top and A-A' cross section views of the tunable QMSIW antenna.

continuous tuning over a broader range, while maintaining the same miniaturization. The antenna is loaded with a corner shortening via connected to two series capacitive gaps on the cavity's top wall. Afterwards, these gaps are loaded with two pairs of varactor diodes to load the antenna capacitively and change the frequency of operation.

2.3.2 Antenna Topology and Design

Fig. 2.17 shows the top and side views of the proposed tunable antenna. The antenna is designed based on a Rogers [47] RT/duroid 5880 substrate ($\epsilon_r = 2.2, tan\delta = 0.0009$) with thickness of $h = 1.6$ mm. A full mode SIW circular cavity resonator is loaded with a shortening via (all via holes have the same diameter of 1.1 mm) at the center, then two series surface ring gaps with width of 1 mm are inserted

on the cavity's top wall in order to isolated the via post from the cavity top wall and at the same time load the cavity resonator with a very small series capacitance. Afterwards, the resonator is transformed into a QMSIW one based on the approach first introduced in [53]. Since the cutting lines are fictitious magnetic walls, each of the quadrants operates at a very similar mode to a full mode SIW resonator. This results in a ∼75% miniature cavity resonator and as a result a miniature antenna. The two edges of the quarter-mode resonator are the ones responsible for radiation as described in detail in [51], as a result inserting the via post in the middle does not affect the radiation characteristics of the antenna. Accordingly, by locating 4 varactor diodes over the series capacitance gaps, the capacitance value of the gaps is increased and as a result, the frequency of the antenna is shifted down. Based on the value of the varactor diodes' capacitance, the frequency shift varies. While frequency tuning for the antenna is also possible using only one surface ring gap, in order to bias the varactor diodes easier, two of these gaps are inserted on the cavity's top wall. The metal strip with width of 1 mm in between the ring gaps is used for biasing the varactor diodes. This results in a very simple bias circuit and also a back-to-back varactor diode configuration, which consequently means improved linearity for the antenna [52].

2.3.3 Fabrication, Simulations, and Measurements

A prototype of the antenna is fabricated and shown in Fig. 2.18 using common PCB techniques. High performance varactor diodes (Skyworks SMV2019-079LF) are used along with a 56 nH RF choke as the tuning components. The positive voltage needed for the varactor diodes is applied to the antenna using a bias pad on the top layer. The bias ground is applied to the antennas bottom cavity wall as shown in Fig. 2.17, and 2.18.

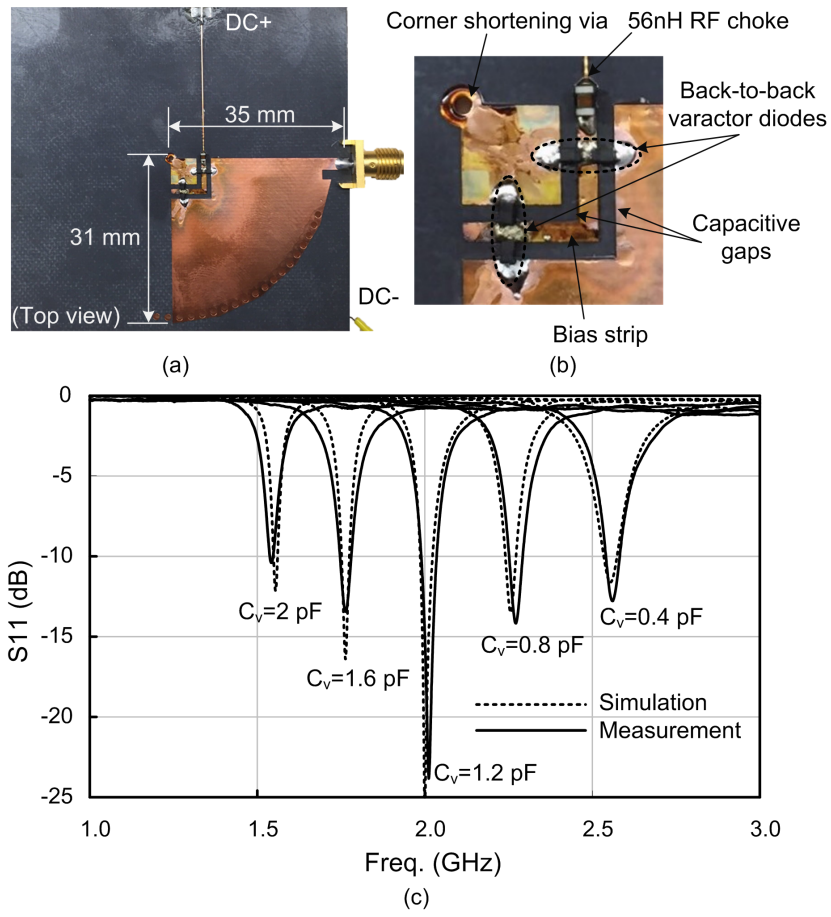

Fig. 2.18: (a) Top view of the fabricated tunable QMSIW antenna. (b) Magnification of the capacitive gaps and the back-to-back varactor diodes. (c) Simulated and measured S_{11} results.

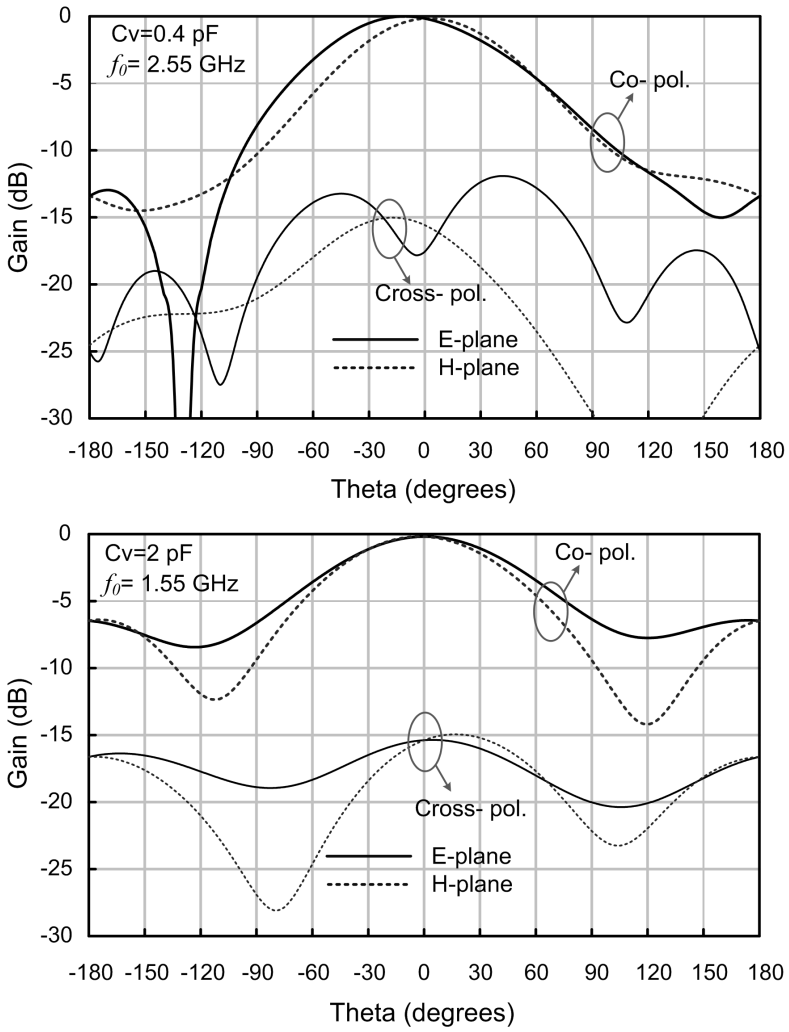

Fig. 2.19: Simulated radiation pattern of the proposed QMSIW antenna at two operating frequencies of 2.55, and 1.55 GHz.

A detailed version of the antenna is simulated using HFSS. Varactor diodes' packaging effects are added in the full-wave simulations, and the capacitive loading effects are included in the modelings using the ADS circuit simulator. The simulated and measured S_{11} results are shown in Fig. 2.18. As can be seen, the antenna performs a tuning range of 1.55-2.55 GHz (∼1.7:1). The simulated radiation pattern of the antenna is shown in Fig. 2.19. Simulations show that the polarization of the antenna is linear and it offers a pattern purity (i.e. difference between the cross- and co- polarized levels) of better than 15 dB. The pattern is one-sided over the tuning range with a front-to-back ratio varying in the range of 7–14 dBc. The simulated maximum gain of the antenna is in the -0.5–4.5 dB range.

2.3.4 Conclusion

A varactor-tuned ultra-compact QMSIW antenna is proposed for the first time, to the best of author's knowledge. By employing the capacitive loading tuning method, additional miniaturization is achieved and the antenna at its lowest operating frequency is 84% miniaturized. The antenna achieves a matching of better than -10 dB over its tuning ratio of 1.55-2.55 GHz (∼1.7:1).

2.4 A 1.7–2.2 GHz Compact Low Phase-noise VCO Using a Widely-tuned SIW Resonator

2.4.1 Introduction

Tunable high-Quality factor (Q) resonators are fundamental units of nowadays reconfigurable microwave circuits and modules such as tunable microwave filters and antennas, and low-phase noise voltage-controlled oscillators (VCO). Recently, by the invention of substrate integrated waveguide (SIW) structures, achieving a high-Q resonator along with advantages of low profile, ease of fabrication, and integration compatibility with other planar structures has become feasible [54].

Different tuning methods of SIW resonators have been reported in [55–58]. In [55,56] a varactor mounted on a floating metal patch on the back side of the cavity is used to tune the SIW resonator in which a tuning range of 20% in [55] and 2% in [56] is achieved, respectively. Despite the tuning range presented in [55], the slot etched around the floating metal patch might be the reason for the reported low-moderate quality factor of the tuned SIW resonator (Qu=30 150). In [57], a varactor is directly coupled to the SIW cavity, and thus using the loading effect of the varactor, a tuning range of 492 MHz at a center frequency of 11.45 GHz (4.3%) is reported.

Although some of the above tuning techniques have been employed in voltage controlled oscillators (VCOs) with SIW resonators, they have resulted in either low tuning range, or higher phase-noise for a portion of the tuning range where the Q of the resonator drops. For example in [58], the floating metal plate tuning method is applied to a reflective-type VCO structure in which a tuning range of 4.8% along with a phase-noise of around 88 dBc/Hz at a 100-kHz offset is achieved. In [40], the varactor coupling technique is used to implement a tunable active antenna oscillator with a tuning rang of 180 MHz (fc=10 GHz). The same technique has been applied

to a low phase noise VCO structure in [57], where a tuning range of 4.1% along with a phase-noise of -93 dBc/Hz at a 100 kHz offset is presented.

In this section, a widely-tuned low phase-noise VCO based on an SIW cavity resonator is presented. In order to tune the SIW cavity, a unique method is utilized to achieve a wide tuning range while not affecting the Q of the resonator. The tuning method is based on what has been presented in [41, 59, 60] to tune SIW-cavity filters and antennas using the loading effect of via posts inside the cavity. However, in this work the via posts are continuously loaded with a varactor diode instead of having them connected to or disconnected from the cavity bottom layer using a switch. This way an analog tuning range of 1.8-2.4 GHz is achieved for the resonator. Also, loading the cavity resonator with the tuning posts results in miniaturization by a factor of 50%. Benefiting from a two-layer structure, the biasing layer is totally isolated from the cavity resonator. Therefore, all the components of the VCO, including the active parts entirely fit within the area of the SIW resonator, on top of the biasing layer. Due to the high-Q of the SIW cavity resonator over the tuning range, a phase noise of better than 109 dBc/Hz at a 100 kHz offset within the tuning range is achieved.

2.4.2 The Tunable SIW Cavity Resonator

2.4.2.1 Resonator Design

The design of the resonator is based on the same procedure as discussed in section 2.1.2.1. For the sake of brevity, this information is not repeated here. However, the layout of the resonator is shown in Fig. 2.20, and the related parameters are tabulated in Table 2.3.

2.4.2.2 SIW Cavity Miniaturization

The tuning via posts are permanently disconnected from the cavity top-wall using the cavity openings in this metal layer (Fig. 1). This causes the disconnected via

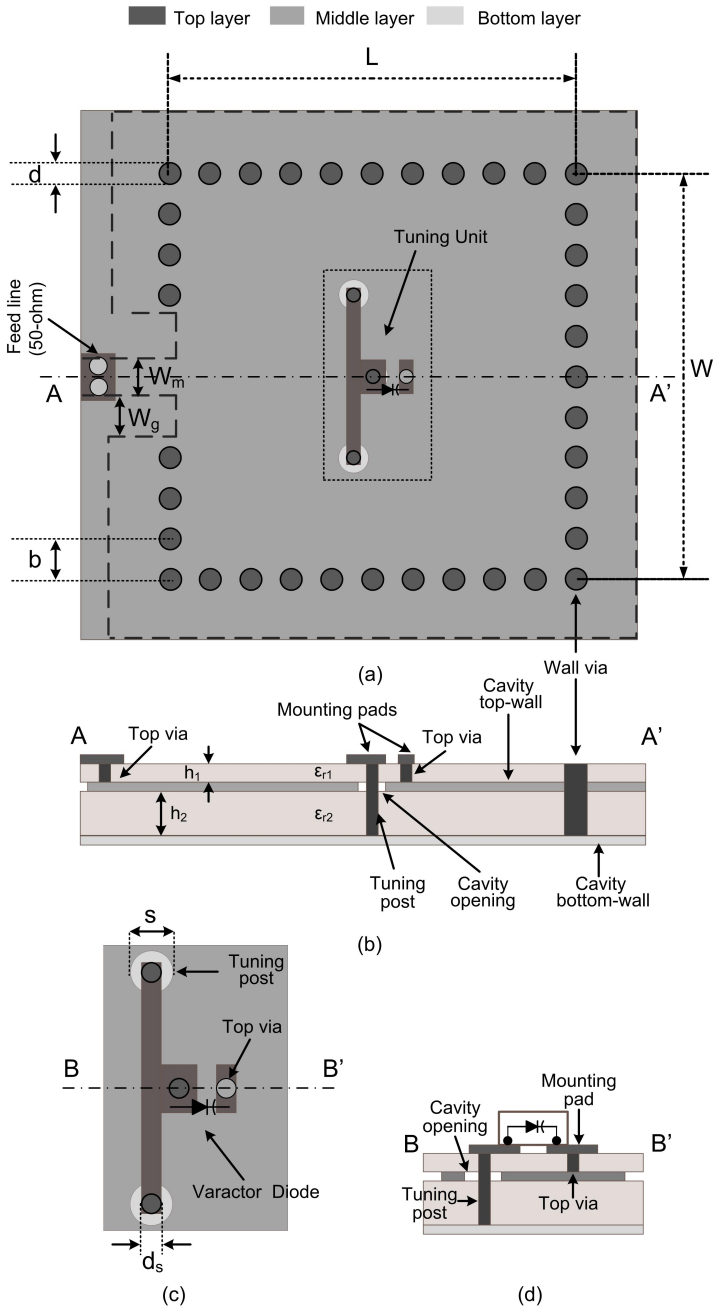

Fig. 2.20: (a) Top view of the proposed SIW cavity resonator. (b) A-A' cross section view of the structure. (c) Magnification of the tuning unit. (d) B-B' cross section view of the tuning unit.

Table 2.3: The Tunable SIW Cavity Parameters.

L	20 mm	W	20 mm	d	1 mm	b	2 mm
d_s	0.6 mm	S	1.4 mm	h_1	0.65 mm	h_2	1.9 mm
ϵ_{r1}	10.2	ϵ_{r2}	10.2 mm	W_m	1.7 mm	W_g	2.2 mm

posts to load the cavity resonator and as a result, they shift down the resonance frequency. The cavity resonator is designed to work at 3.5GHz. However because of this loading effect the new operating resonance frequency of the resonator is located at 2.4GHz. This frequency shift equals to a miniaturization by a factor of 50%. This is computed using $[(\text{Area}_c - \text{Area}_n)/\text{Area}_c] \times 100$, where Area_c is the area of the cavity for a conventional resonator with a resonance frequency of 2.4 GHz, and Area_n is the same parameter for the proposed cavity resonator. The height for the two cavity resonators is assumed to be the same for proper comparison. This can be described by the capacitive loading effect of a disconnected via post. By increasing the number of the via posts, the capacitive loading effect and as a result, the frequency shift increases. This miniaturization factor does not include parasitic loading effects due to the biasing circuit and the diode. The miniaturization does not affect the quality factor of the cavity resonator as will be seen later.

2.4.2.3 Tuning Mechanism

The SIW cavity resonator is tuned by loading the resonator with via posts. Instead of loading the SIW cavity using the floating metal patch as shown in [55,56], or coupling a varactor directly to the SIW cavity in [57], the SIW cavity is loaded with three via posts all connected to a metal pad on the biasing layer (2.20). A varactor diode connects the pads for the three tuning via posts to the pad for the top via. Using this technique, the varactor diode is placed between the top and bottom metal layer of the SIW cavity resonator. Applying different voltages across the varactor diode changes the effective capacitance value seen by the via posts. As a result, the operating frequency of the SIW cavity resonator is changed. The permanent disconnection of the through via posts and the SIW cavity top wall is ensured using three circular slots with diameter S etched around the via posts in the middle metal plane

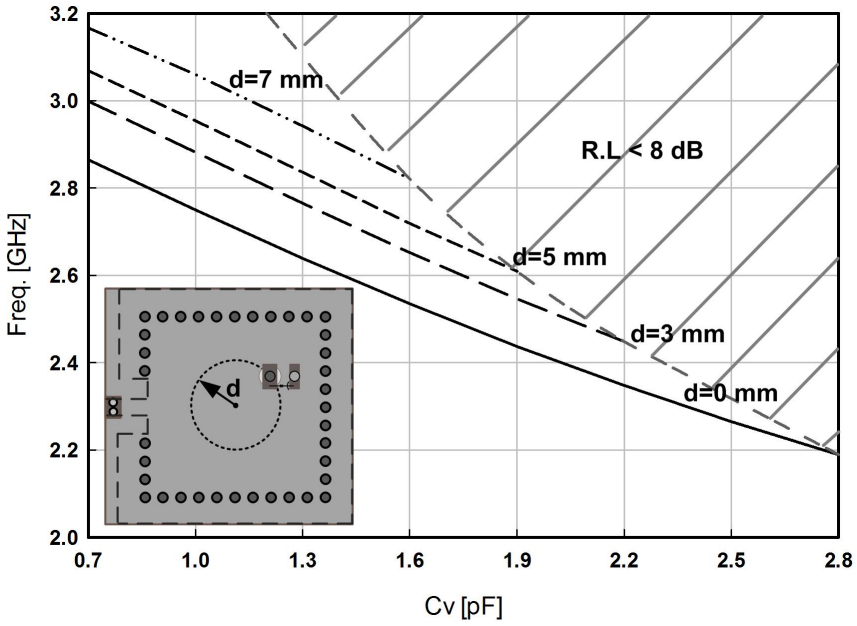

Fig. 2.21: Variations of frequency with respect to the effective capacitance of the varactor diode (C_v) and the distance of the via from the center of the SIW cavity (d, as displayed in the inset of the figure).

as shown in Fig. 2.20(d). Because of the small size of these openings compared to the wavelength at frequencies of operation, they do not affect the quality factor of the SIW cavity resonator [60].

As mentioned before, both the location of the via post and the effective capacitance of the varactor diode are responsible for the resonance frequency of the SIW cavity resonator. In order to study the effect of each, and understand how each one contributes to tuning of the SIW resonator, different combinations of via post locations and the varactor capacitance values are simulated using a commercial High Frequency Structure Simulator (HFSS) [43]. The extracted data is then used to plot the graph shown in Fig. 2.21. This figure shows the relation between the resonance frequency, distance of a sole via post from the center of the cavity (shown in Fig. 2.21 as d), and the effective capacitance value of the varactor diode. It is notable

that the acceptable resonance frequencies are only the ones with an input matching better than -8 dB. As a result, for the distance farther than 3 mm, the capacitance values of more than 2.2 pF cannot be used.

As can be seen, the closer the via post to the center of the SIW cavity, the more tuning range can be achieved. On the other hand, the loading effect of the varactor diode is much less for the cases where the via post is located farther from the center of the cavity and closer to the cavity side walls. For example, for d=7 mm (the closest position of the via post to the cavity side wall), the tuning range is within 2.6–3.2 GHz range. The upper frequency in this case is very close to the intrinsic resonance frequency of the unloaded SIW cavity with minimal varactor loading ($f_{0,u} \approxeq 3.5$ GHz).

Based on Fig. 2.21, and the relationship between the resonance frequency and the via post location, three different via posts are initially inserted into the regions where the shift in the frequency is at its highest value or the E-field inside the cavity is maximum with minimal varactor loading [41, 49, 59, 60]. The final position for the three via posts is then optimized using HFSS to achieve the highest frequency shift possible. In order to study the effect of the via posts when loaded with different capacitance values, the E- field distribution inside the cavity is shown in Fig. 2.22. As can be seen, by increasing the capacitance value of the varactor, the effect of the via posts on the field distribution also increases and the frequency of the SIW resonator decreases. Using three via posts connected to the varactor diode, a tuning range of 1.8–2.4 GHz is achieved.

Finally, Table 2.4 shows the resonance frequencies and simulated unloaded quality factors of the final tunable resonator cavity with three via posts connected to a varactor diode. The quality factor of the SIW resonator slightly decreases as the capacitance value of the varactor increases. This relates to the smaller electrical size

Table 2.4: SIW Resonator Tuning Range Information and the Via Posts' Locations of Via Posts.

Tuning range information			**Via posts' locations**	
C_v (pF)	f_0 (GHz)	Q_u	Post	Location: (P_x, P_y in mm)
0.7	2.4	297	P	(10,10)
1	2.27	305	R1	(6,9)
1.2	2.15	296	R2	(14,9)
1.6	2.05	286	–	–
2	1.92	283	–	–
2.4	1.8	280	–	–

of the cavity when loaded with a larger capacitance value and also this fact that the ohmic loss and the capacitance value of the varactor are maximum at the same time. The tuning range of the SIW resonator is set for a higher upper limit of 2.4 GHz compared to the one of the VCO (2.2 GHz). This helps to achieve the oscillation conditions for the entire tuning range as will be discussed in the next subsection.

2.4.3 Reflective-type Tunable SIW VCO Design

The tunable SIW cavity resonator is used in a negative resistance, reflective-type oscillator [29]. Fig. 2.23 shows the topology of the oscillator employing a series source feedback capacitance (C_s) to introduce the negative resistance needed. The gate network consists of a 50-ohms microstrip line with length θ_g in series with a varactor (C_g), and the tunable SIW cavity resonator with an impedance of $Z_C(f)$. The series varactor (C_g) is responsible for maintaining the oscillation conditions satisfied as the loading impedance of the SIW cavity resonator changes with frequency [29, 61]. The drain network consists of a DC blocking capacitor (C_B), and a three-pole elliptic low pass filter realized by lumped off-the-shelf components. The filter is designed in a way to have a cut off frequency of 2.6 GHz, and minimum -30 dB harmonic suppression over the entire VCO tuning range. The entire VCO circuit including the gate, source, and drain networks is placed on the back side of the SIW cavity resonator and as a result, a very compact VCO with a size limited to the area of the

SIW resonator is achieved.

2.4.3.1 Source Network

In order to design the source network, a simplified circuit shown in Fig. 2.24(a) is characterized using Agilent ADS. As described in [29,61], in order to have a common source oscillator topology with an output located at f_0, the value of C_s must be adjusted to provide a negative resistance looking into the gate. In other words, the condition $|\Gamma_{IN}(f_0)| > 1$ must be satisfied at all times. Therefore, the properly-biased transistor is terminated by 50-ohms loads at the gate and drain ports and then simulated in Agilent ADS using the non-linear model of the transistor [62]. The transistor used in this design is the Avago Technologies' ATF-36077 pseudomorphic high electron-mobility transistor (pHEMT). Fig. 2.24(b) shows the variation of $|\Gamma_{IN}|$ at $f_0 = 2.2$ GHz with respect to the changes in the source capacitance value (C_s). In order to maintain the oscillation condition satisfied at all times, the Cs value is chosen to maximize $|\Gamma_{IN}|$ at $f_0 = 2.2$ GHz. In order to achieve a stable oscillation at frequency f_0, the following equations need to be valid [29]

$$|\Gamma_{IN}| \times |\Gamma_g(C_v, C_g, f_0)| > 1 \tag{2.4}$$

$$\angle\Gamma_g(C_v, C_g, f_0) = -\angle\Gamma_{IN}(f_0) \tag{2.5}$$

Fig. 2.24(b) also shows the $\angle\Gamma_{IN}$ with respect to frequency for the source capacitance value of $C_s = 4$ pF. Choosing a constant C_s of 4 pF will guarantee the oscillation condition for all other frequencies of operation as will be shown in the following.

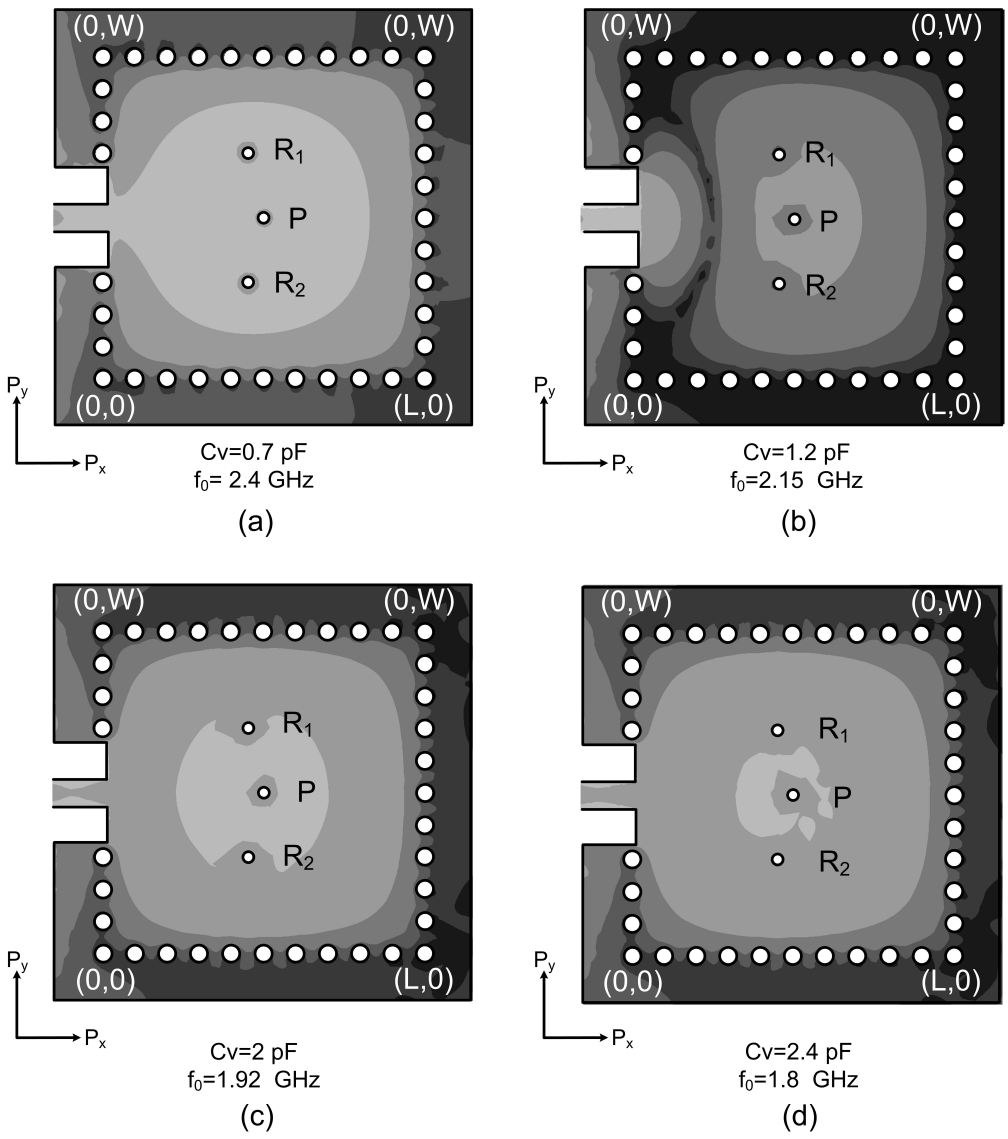

Fig. 2.22: Magnitude of electrical field distribution inside the SIW cavity resonator for different capacitance values for the varactor diode.

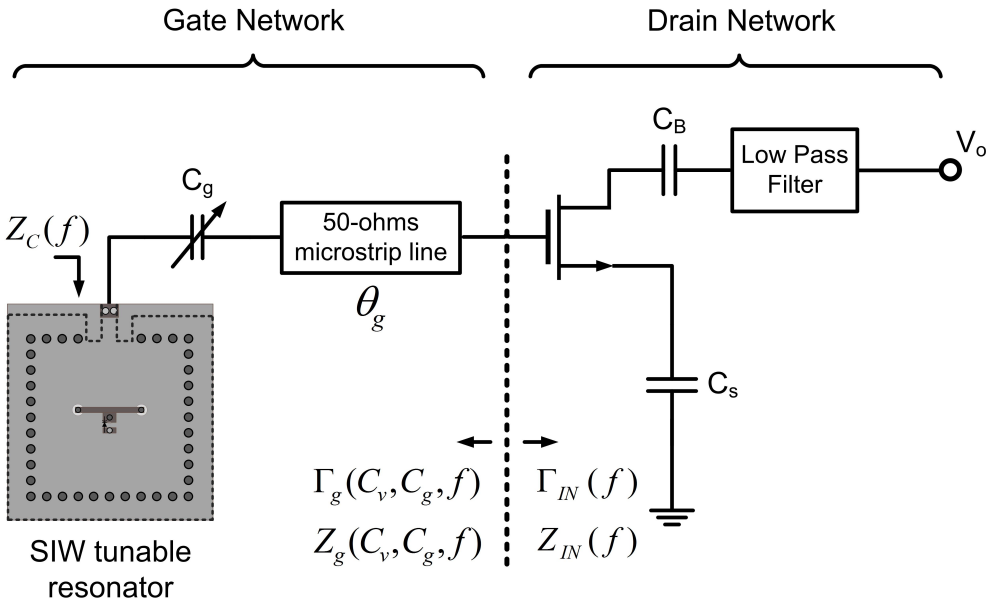

Fig. 2.23: Topology of the negative resistance reflective-type oscillator.

2.4.3.2 Gate Network

As mentioned before, the gate network has three sections. The SIW tunable cavity resonator (Fig. 2.20), the variable capacitor C_g, and the microstrip line with the electrical length θ_g (Fig. 2.23). The combination of these three should present a load $[Z_g(C_v, C_g, f)]$ that satisfies the oscillation conditions at all desired oscillation frequencies. The validity of the oscillation conditions can be studied by comparing the phase and magnitude of $|\Gamma_{IN}(f)|$ and $|\Gamma_g(f)|$. Fig. 2.25 shows that different oscillation frequencies are achieved with different microstrip line electric lengths (θ_g), while having different resonator states (different C_v values). This figure indicates that for two different conditions (C_v= 0.7, 2.4 pF) significantly different electrical lengths (θ_g=12.5◦, 18◦) are needed to guarantee the oscillation. It is noteworthy that different electrical lengths, θ_g=12.5◦, 18◦ at 2.3 and 1.78 GHz shown in Fig. 2.25 are related to two different physical line lengths. In order to achieve a wide oscillation

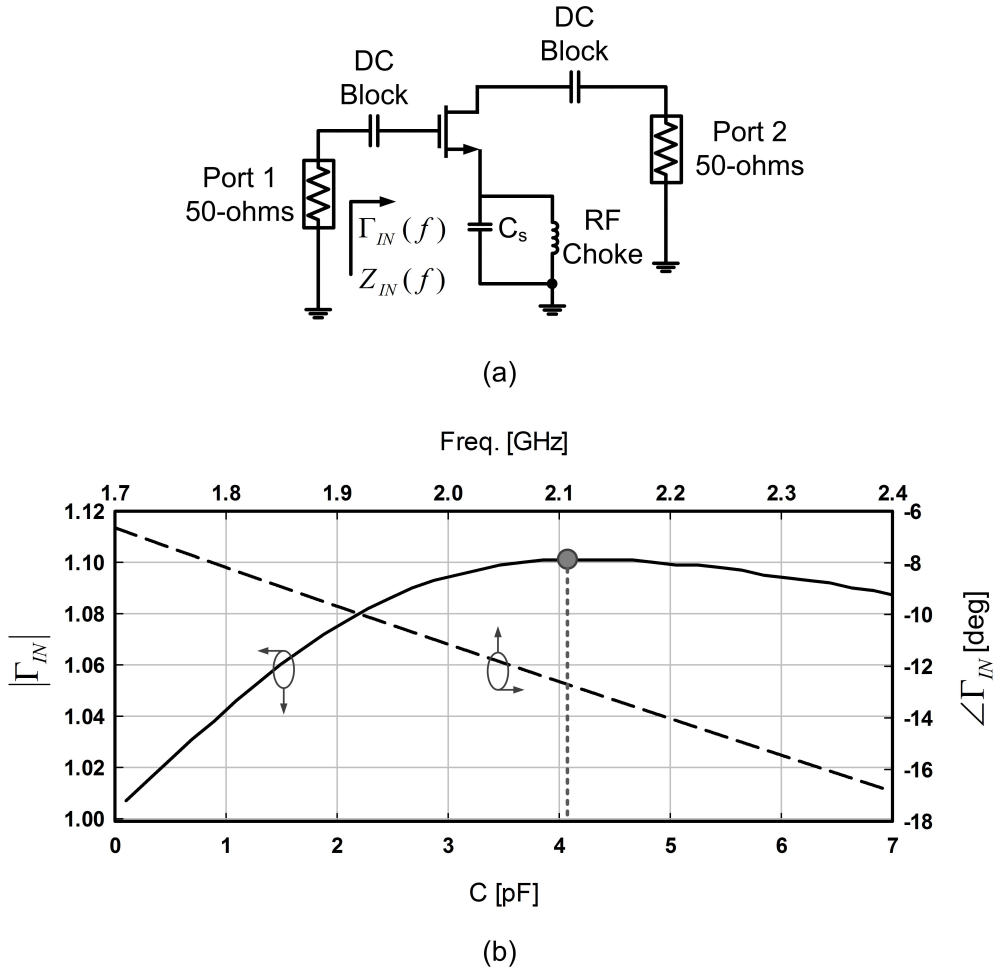

Fig. 2.24: (a) Simplified circuit topology used for the determination of C_s. (b) Different values of $|\Gamma_{IN}|$ with respect to C_s at f_0=2.2 GHz (left and bottom axes) and $\angle\Gamma_{IN}$ with respect to frequency for $C_s = 4$ pF (right and top axes).

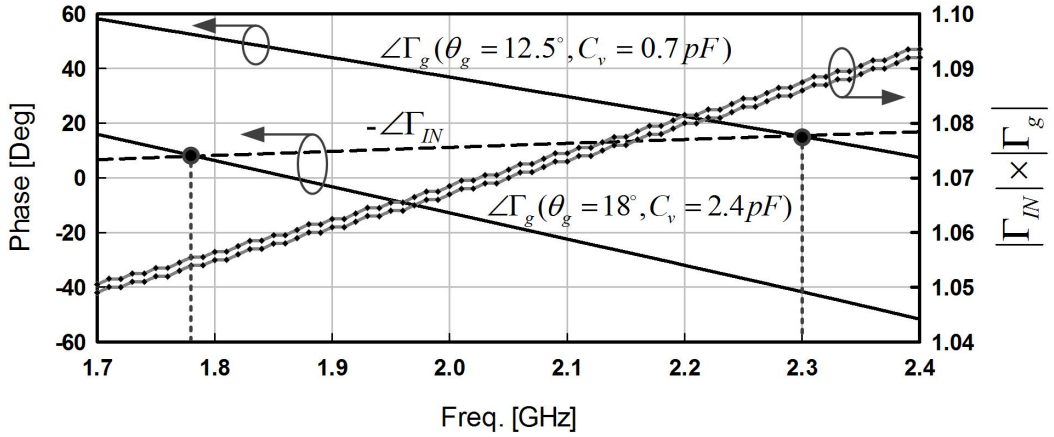

Fig. 2.25: The oscillation conditions (2.4) and (2.5) for different microstrip line lengths (θ_g) for two different cases of C_v=0.7 pF and C_v=2.4 pF.

range using a single microstrip line, another tunable element (C_g) is needed to negate the mandatory variations for the microstrip line section. In order to better explain the effect of C_g, different values of $\angle\Gamma_g(f)$ for various combinations of C_v and C_g are shown in Fig. 2.26(a) for fixed microstrip line length of 2.5 mm. As a result, the variable capacitance C_g, guarantees the oscillation condition (2.5) for all the targeted frequencies using a single line structure. The intersections between $\angle\Gamma_g(f)$ and $-\angle\Gamma_{IN}(f)$ (possible oscillation frequencies) are shown for 4 different C_v and C_g values. As can be seen, the tuning range of 1.8–2.2 GHz is achieved for 0.7 pF $< C_v <$ 2.4 pF and 0.7 pF $< C_g <$ 5 pF. Fig. 2.26(b) shows $|\Gamma_{IN}| \times |\Gamma_g(C_v, C_g, f_0)|$ for the same 4 different values of C_v, C_g in Fig. 2.26(a). As can be seen, condition (2.4) is also valid for the oscillation range of interest.

2.4.3.3 Drain Network

The drain network of the oscillator consists of a DC block capacitor (C_B), and a low-pass filter which is used for harmonic suppression at the output of the designed oscillator (Fig. 2.23). A three-pole elliptic low-pass filter is employed and imple-

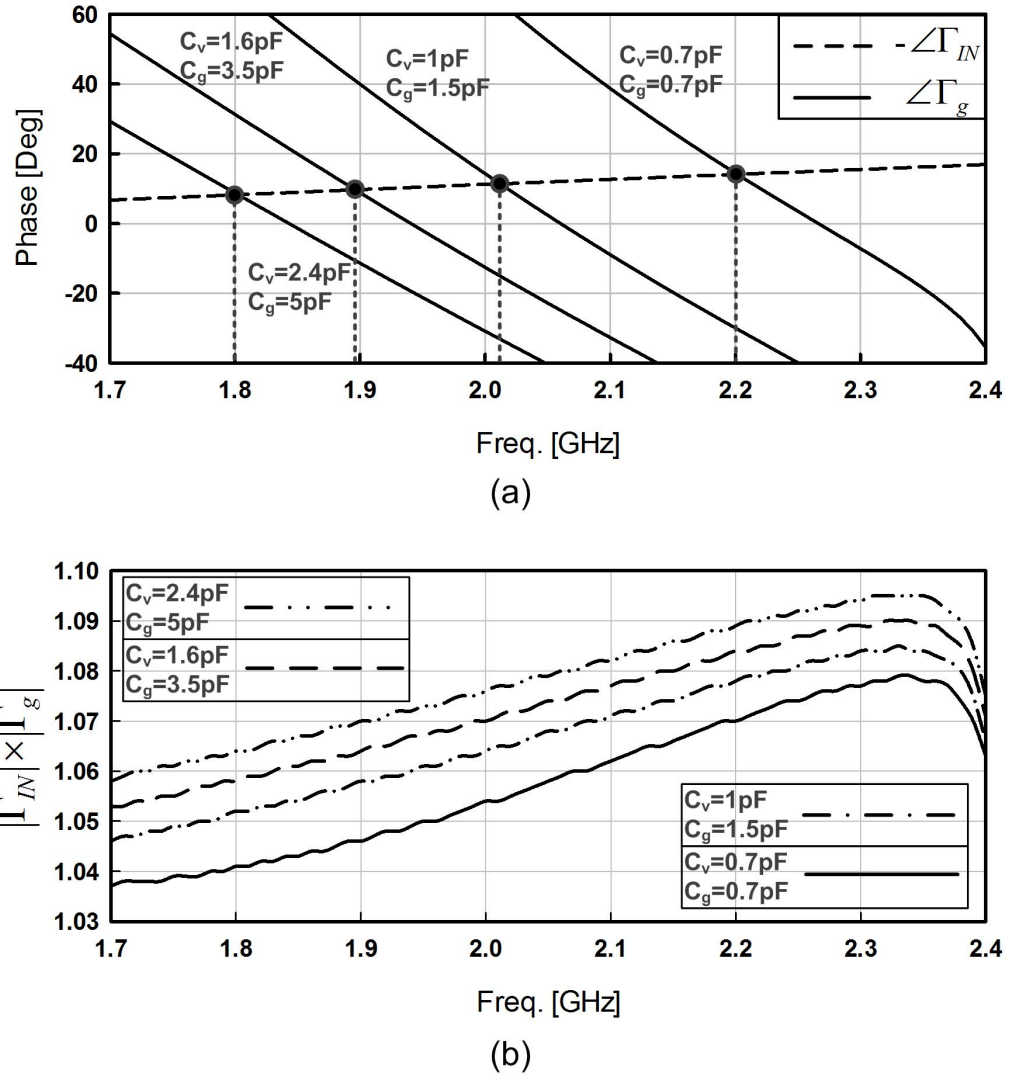

Fig. 2.26: (a) $\angle\Gamma_g$ compared to $\angle\Gamma_{IN}$ to validate the oscillation condition in (2.5) for different values of C_v and C_g and constant microstrip line length of 2.5 mm. (b) Oscillation condition validation in (2.4) as a function of frequency for different values of C_v and C_g.

mented using surface mount inductors and capacitors. In order to make sure the filter works properly while implemented within the VCO circuit; (1) the filter input port needs to be matched to the output impedance of the VCO instead of 50-ohms using ADS, and (2) full-wave simulations are required to take into account the effects of traces and connection pads on the performance of the filter using HFSS. Fig. 2.27(a) shows the filter topology designed using ADS. The final layout of the designed VCO is illustrated in Fig. 2.27(b). The filter layout has some modifications compared to the topology shown in Fig. 2.27(a). Some of the components are modified in the layout because of the additional parasitic effects of the traces and pads; as a result, L_3 is completely removed in the final layout. Fig. 2.28 shows the performance of the initial filter designed in ADS along with the modified filter designed using HFSS. As can be seen, an attenuation of better than -20 dB is achieved for frequencies higher than 3 GHz. This guarantees 2^{n}d and higher harmonic suppression level of at least 20 dB.

2.4.4 Fabrication, Measurements, and Discussion

2.4.4.1 Fabrication

The SIW-based tunable VCO is fabricated using the RogersRT/Druid 6010 ($\epsilon_r = 10.2, tan\delta = 0.0023$) substrate for both layers of the structure (cavity resonator and biasing layers) [47]. The biasing circuit along with all the traces and the mounting pads are etched on the upper side of the biasing layer, and the cavity resonator top wall with the openings is etched on the other side of this layer. The top vias are drilled in this step through the biasing layer. Afterwards, the cavity bottom-wall is etched on the backside of the cavity resonator layer, while the other side is totally removed. The backside of the biasing layer is then bonded to the upper side of the cavity resonator layer using the Rogers RO4450B pre-preg material ($\epsilon_r = 3.3, h = 0.09$ mm). Finally,

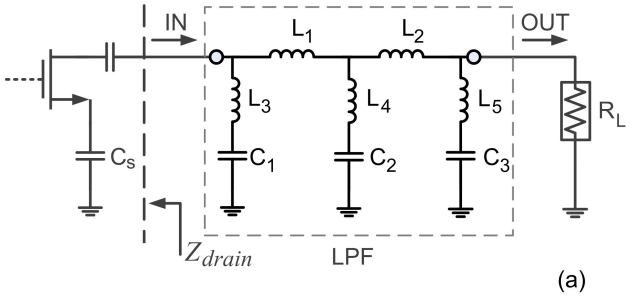

(a)

	Initial	Modif.		Initial	Modif.
L_1	3.9nH	2.6nH	L_5	0.35nH	0.25nH
L_2	3.5nH	3.2nH	C_1	2pF	0.5pF
L_3	0.5nH	-	C_2	2.6pF	1.4pF
L_4	0.8nH	0.55nH	C_3	1pF	1pF

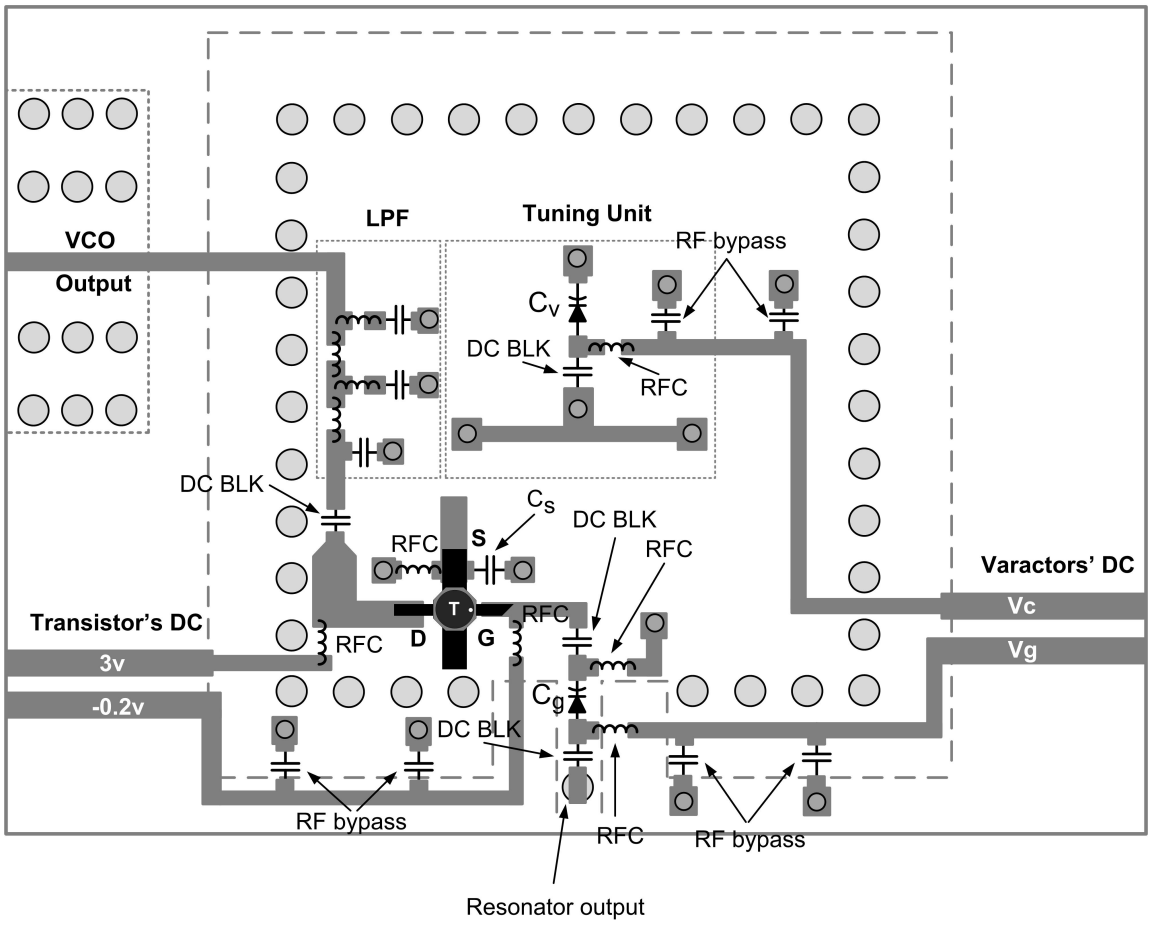

(b)

Fig. 2.27: (a) Initial filter topology and components' values. (b) Final layout of the designed VCO.

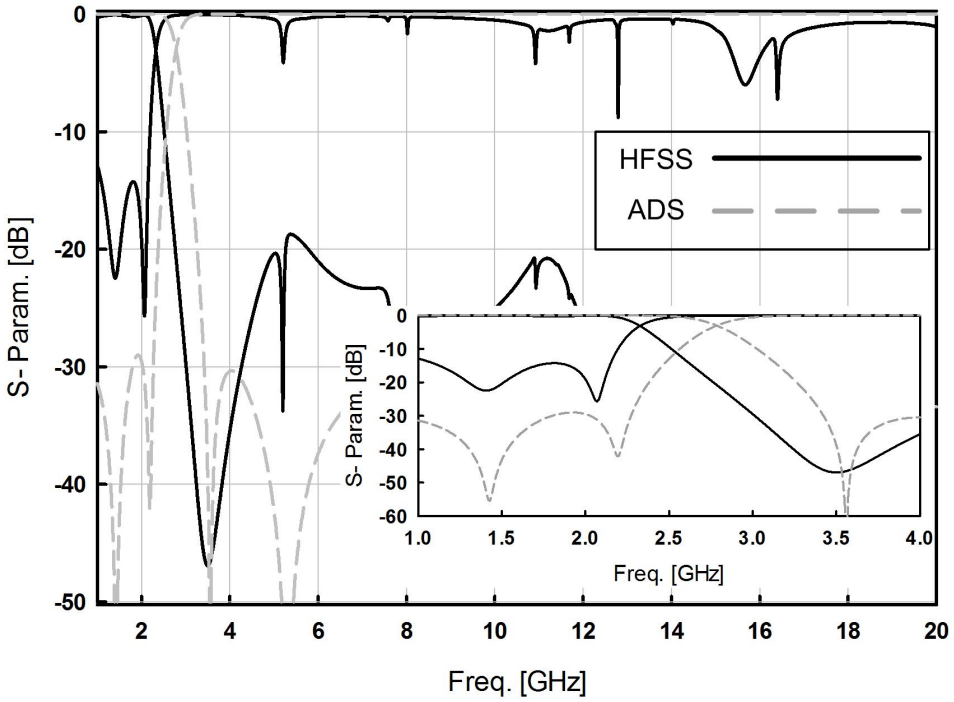

Fig. 2.28: Low-pass filter response (both ADS and full-wave HFSS results are shown). An inset of only the pass-band response is also shown for clarification.

the through vias are drilled through the entire structure. High performance varactor diodes from Skyworks, the pHEMT transistor, and biasing components are mounted on the mounting pads on the biasing layer. The biasing circuit used in [[60], Fig. 8(a)] is also used as the biasing network of the varactor diodes here. The value of all the DC block capacitors is 18 pF, and the value of all the RF-choke inductors is 56 nH in Fig. 2.27(a). In order to ensure that the pre-preg material and the biasing circuit's effects on the performance of the cavity resonator are negligible, they are considered in the 3D full-wave simulations of the resonator.

2.4.4.2 Experimental Result

The realized VCO shown in Fig. 2.29 has been measured using a spectrum analyzer (Agilent E4446A) to characterize its oscillation frequency, tuning range,

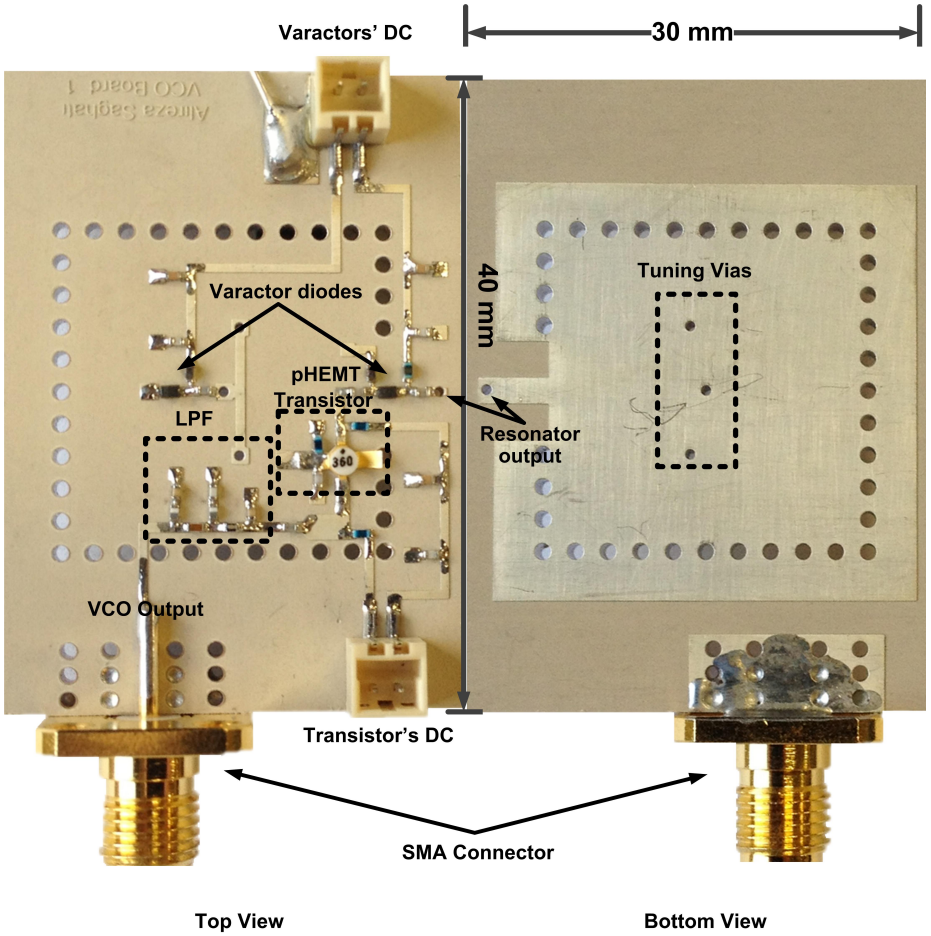

Fig. 2.29: Fabricated 1.7–2.2 GHz SIW tunable VCO.

output power, second harmonic suppression, and phase noise.

As mentioned before, the frequency of oscillation in the proposed VCO depends on two different capacitance values of C_v and C_g, where the former is used for coarse tuning and the latter for fine tuning. The measurements are repeated for all the combinations of C_v and C_g to cover the VCO's entire tuning range. As a result, five different values for C_v are used.

Fig. 2.30 shows different measured oscillation frequencies along with the VCO output power variations versus different values of C_v and C_g. As shown in Fig.

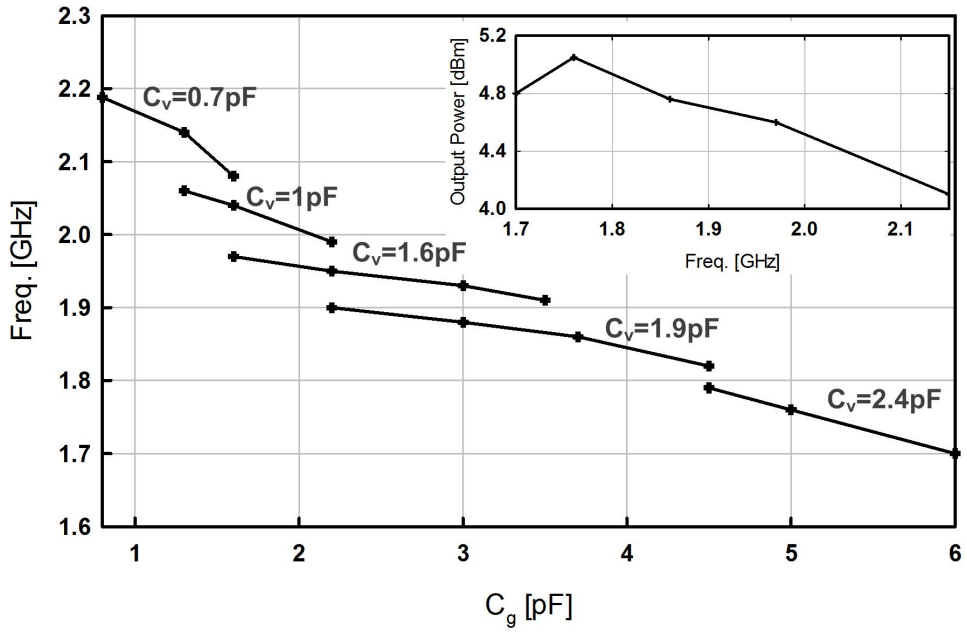

Fig. 2.30: Measured oscillation frequencies of the SIW VCO with respect to the changes in C_g and C_v. The inset figure shows the VCO output power for four different frequencies (the cable loss of 1.5 dB is excluded).

2.27(b), the applied bias voltages to the pHEMT transistor are V_d= 3 v, and V_g= -0.2 v. The current consumed by the transistor is I_d=17 mA. As a result the power consumption is ∼51 mW. The tuning range of the VCO is 1.7–2.2 GHz (∼26% based on a 1.95 GHz center frequency) while having a minimum output power of 4.1 dBm excluding measured cable loss of 1.5 dB.

Measured phase noise of the VCO at an offset of 100 kHz is shown in Fig. 2.31 for the entire tuning range. As can be seen, the phase noise lower than 109 dBc/Hz at a 100 KHz offset is achieved. Fig. 2.31 also shows the second harmonic suppression level compared to the fundamental oscillation frequency for the entire range, and a harmonic suppression level of better than 28 dBc is achieved. The measured output spectrum of the SIW VCO is shown in Fig. 2.32 for four different operating frequencies. Also the phase noise diagram for f_0=2.2 GHz is shown in Fig. 2.33. A

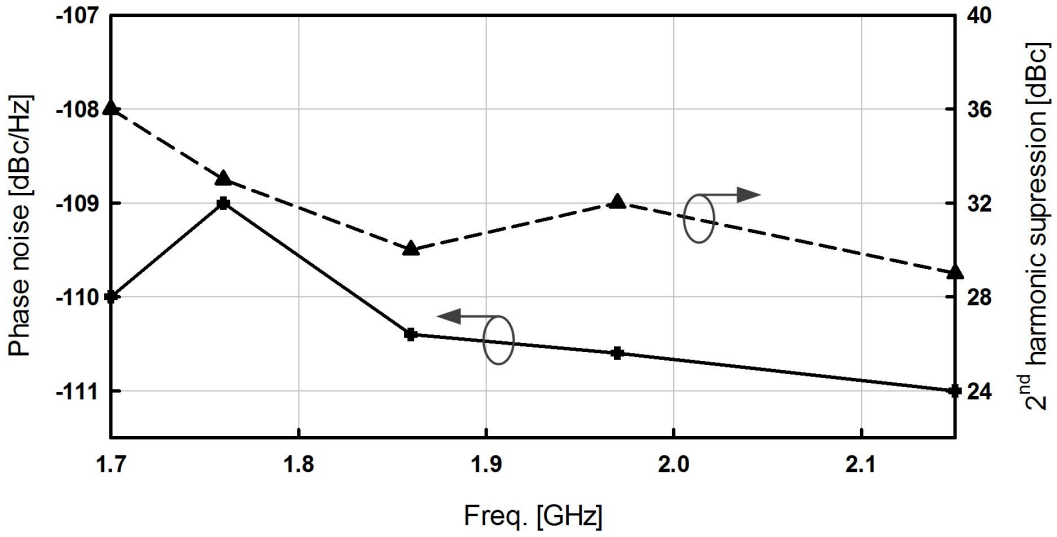

Fig. 2.31: Phase noise and second harmonic suppression for four different frequencies.

phase-noise better than -111 dBc/Hz at an offset of 100 kHz is achieved in this case.

2.4.5 Conclusion

A 1.7–2.2 GHz low phase-noise SIW VCO is presented. The design of the widely tunable SIW resonator is based on inserting 3 via posts into the cavity resonator while connected to a varactor diode. As a result, using the loading effect of the varactor diode a wide tuning range of 1.8–2.4GHz for the SIW resonator is achieved. The designed SIW resonator is then utilized in a reflective VCO topology in order to achieve a tuning range of 1.7–2.2 GHz (26%). Due to the high Q of the SIW resonator over the entire tuning range a low phase-noise of at least -109 dBc/Hz at a 100 kHz offset is achieved for the SIW VCO. The size of the SIW VCO is limited to the size of the SIW cavity resonator, resulting in a very compact SIW VCO. Measured results for the SIW VCO are presented and are in good agreement with simulations. Also, a comparison table is provided which shows improvement in tuning range, phase noise, and size reduction.

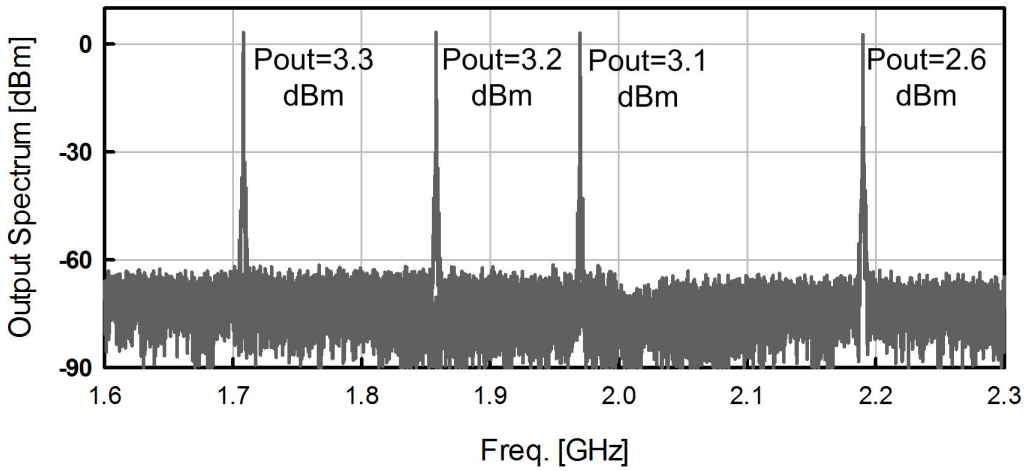

Fig. 2.32: Measured output spectrum of the SIW VCO for four different C_v and C_g combinations.

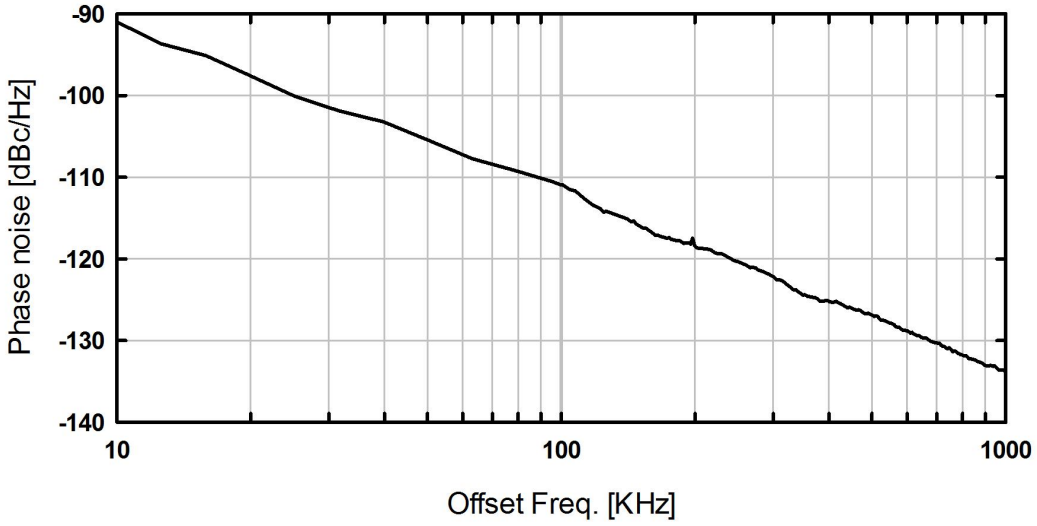

Fig. 2.33: Measured phase noise of the SIW VCO for the 2.2 GHz oscillation frequency.

3. MICROFLUIDICALLY-TUNABLE MICROWAVE DEVICES*

In this chapter, liquid-based microwave tuning devices are proposed. Using a unique method of implementation, the capacitive loading effect of liquid-metal bridges is used to shift the operating frequnecy of microwave devices such as resonators, filters, and antennas. A costume measurement system is employed to evaluate the power-handling capabilities of liquid-based tuning methods for the first time. Using an infra red camera the temperature of a filter is monitored as the input power applied to it is increased. In the second, third, and forth sections, tunable and miniature antennas and filters are proposed. For all cases, prototypes are fabricated and measured to validate the proposed designs.

3.1 A Miniaturized Microfluidically-reconfigurable CPW Bandpass Filter with Maximum Power-handling of 10-Watt

3.1.1 Introduction

Recently there has been an increased interest in tuning microwave resonators and filters using liquid metal [63–67]. This tuning method is found promising for high power RF applications because of its highly-linear behavior [63]. Also incorporating soft materials using simple technologies can result in conformal or wearable tunable microwave circuits [64]. In [63], broadside coupled split ring resonators are used where one of the open loop resonators is constructed from liquid metal. Thus, by gradually removing the metal from the resonator area tuning of 650–870 MHz is achieved. Khan *et al.* have used liquid metal (EGaIn) to change the band-stop properties of a microstrip filter by reshaping its open stub resonator in discrete states [64]. In [65], by filling in different defected ground structure (DGS) lattices, the cut-off frequency of a low-pass filter is tuned while a wide stop-band is maintained.

Different methods are used to embed the liquid channel structure into the circuit. Milling cut-outs in the Rogers dielectric layers and Scotch^{TM} tape are used in [63] to stabilize the Polytetrafluoroethylene (PTFE) tubes. In [64], copper ground plane is used as the base for the Polydimethylsiloxane (PDMS) structure including the liquid channel, and [65] uses two-sided polymide tape (thickness= 0.3 mm) to bond and seal the channel located on top of the circuit's dielectric board.

The major idea behind the tuning methods in [63–65] is based on physically reshaping the resonator or the ground plane using liquid metal. One other tuning/switching approach is introduced in [66], in which the authors used Galinstan on top of a coplanar waveguide (CPW) transmission line as a capacitive 2–100 GHz microelectromechanical systems (MEMS) switch to short the RF path. This approach

is then modified in [67] by employing a 30 μm spin-coated PDMS layer instead of the 180 nm Teflon coating. This way the distance between the liquid metal and the RF path is increased to reactively load CPW resonators resulting in both filter frequency tuning and miniaturization. Additional or same channels can be used for constant flow of low dielectric constant liquids such as Teflon on top of the filter for other applications as well as tuning. For instance, in [68], such micro-channel structures are used for cooling high power passive and active microwave devices.

Liquid metals are not the only fluidics used for tuning microwave resonators and filters. In [69], two metalized glass plates are moved above two open-loop resonators using the flow of Teflon solution inside the microfluidic channels. By moving these metalized glass plates over the open ends of each resonator, the amount of capacitive loading varies, which results in tuning the filter frequency response. Using this method a tuning range of 0.9–1.5 GHz (1.66:1) is presented. Plastic screws and clams are used to hold the micro-channel structure and printed circuit board (PCB) together. In [70], a microfluidic channel is placed inside a 60 mil cavity below a bandpass microstrip filter. By injecting either DI water or acetone, two different pass-band frequencies can be obtained for the filter in response to the change in the dielectric constant number. The filter achieves a switching range of 1.5:1.

In this section, a microfluidically-reconfigurable two-pole CPW filter is proposed. A similar method was first proposed by the authors in [67] to tune microwave resonators (tuning range of 1.4:1 for the CPW resonator). The method is based on loading each filter resonator with three different Galinstan channels (a non-toxic eutectic alloy of Galium, Indium, and Tin with $\sigma = 3.46 \times 10^6$). Using symmetric configurations of filled and empty channels, the loading capacitance on top of resonators changes, and the pass-band frequency of the CPW filter is tuned within the range of 3.4–5.5 GHz. Loading each CPW resonator with liquid metal reduces the

phase velocity as will be discussed later. Due to this slower phase velocity in the loaded regions, a miniaturization is also achieved as the filter at its lowest operating state is 40% smaller than a non-loaded CPW filter working at a similar frequency. To verify the proposed *tuning method* is more suitable for high-power applications, in comparison with conventional tuning methods based on semiconductor, and RF-MEMS devices, a customized high-power measurement setup is utilized to measure the power handling properties of the filter. To the best of authors' knowledge, this is the first verification of liquid tuning microwave filters for high-power applications with maximum power handling of $\sim$ 20 W for short-duration excitation conditions and 10 W for high-average-power excitation conditions. However, since the only limiting factor is observed to be the high temperature of the structure for high-average-power excitation conditions with power levels of more that 10 W, using the filter for higher input power levels may become feasible by using the aid of a heat sink. As this verification shows the feasibility of this tuning method in high-power applications, it motivates future work with more power management considerations in both the fluidics and filter design for a tunable filter with higher power tolerance.

3.1.2 Filter Design

3.1.2.1 Topology

Fig. 3.1 and Fig. 3.2(a) show the layout and circuit model of the microfluidically-reconfigurable two-pole CPW filter, respectively [71, 72]. The filter is designed based on Rogers RT/duroid substrate (ϵ_r = 10.2, tanδ = 0.0023) [47]. In order to avoid Galinstan from sticking to channel walls, a Teflon solution is used as a lubricant (Teflon AF 400S2-100-1, 1% Teflon powdered resin dissolved in 3M FC-40 from DuPont[1]). A PDMS structure including six micro-channels is employed to locate the

[1]Dupont Teflon AF Solution. [Online]. http://www2.dupont.com/Teflon.

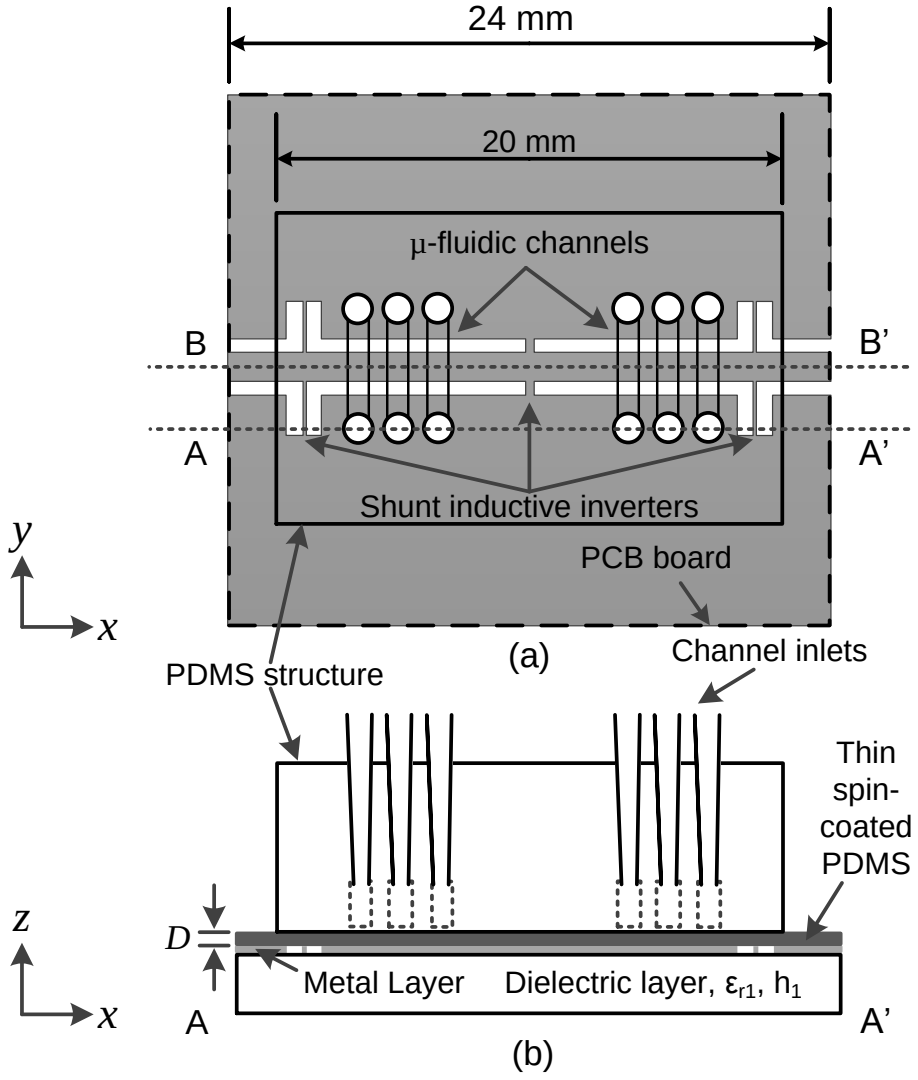

Fig. 3.1: Layout of the digitally-tuned two-pole CPW filter. (a) Top view. (b) A-A' cross section.

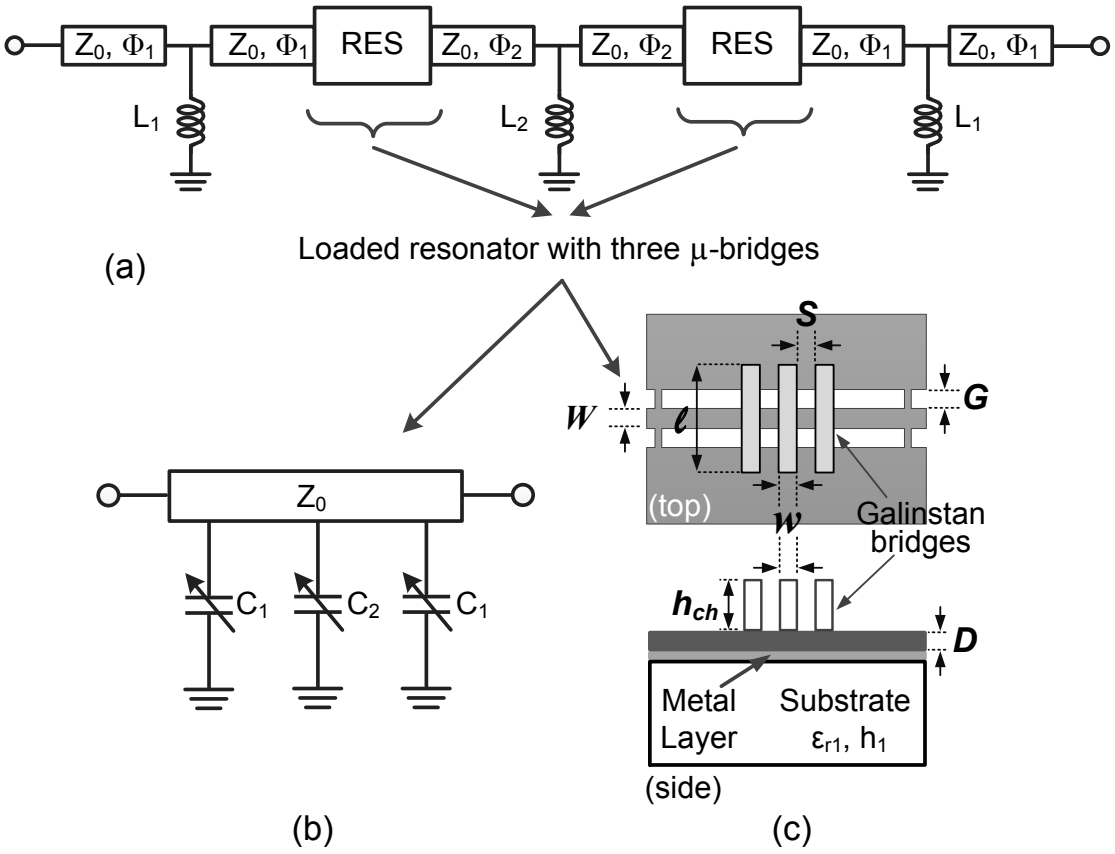

Fig. 3.2: (a) Circuit model of a two-pole loaded CPW resonator tunable filter. (b) Circuit model for the CPW resonator loaded with three μ-bridges. (c) Layout of the CPW loaded resonator (top and side views).

Galinstan bridges on top of the CPW resonators. The PDMS structure is bonded to the filter circuit board using a very thin [$D = 30$ μm, as shown in Fig. 3.1(b)] spin-coated PDMS ($\epsilon_r = 2.68$, $\tan\delta = 0.015$) layer. The thickness of this layer controls the vertical distance between the resonator and the Galinstan bridges. This height is a critical parameter in adjusting the tuning range and the filter miniaturization as will be discussed in the following subsection.

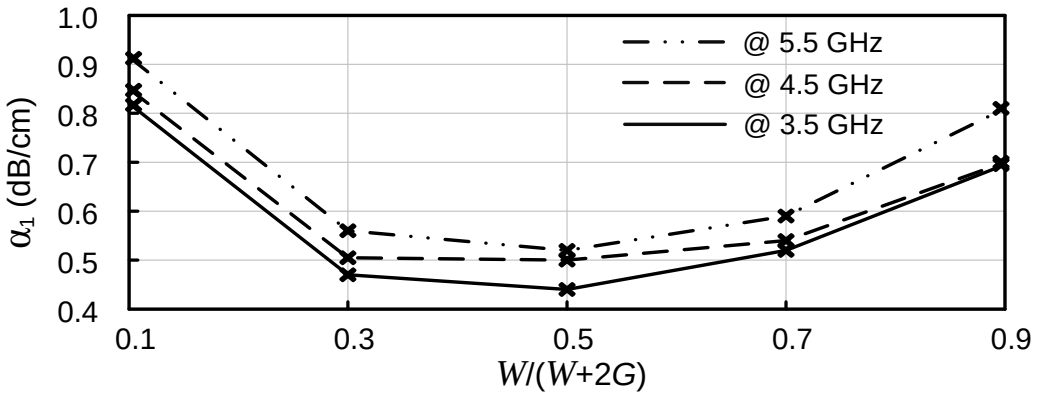

Fig. 3.3: Simulated attenuation constant of a CPW line with $W + 2G = 2$ mm and for different ratios of $W/(W + 2G)$ at 3.5 GHz, 4.5 GHz, and 5.5 GHz.

3.1.2.2 Resonator Design

The resonator is based on 18 μm-thick copper with CPW dimensions of 0.5/1/0.5 mm [G/W/G in Fig. 3.2(c)] and a 1.27 mm thick Rogers RT/duroid 6010 substrate. The dimensions of the CPW resonator are chosen to minimize the conductor losses [73]. The attenuation constant of a CPW line with $W+2G = 2$ mm and for different ratios of $W/(W+2G)$ is found using Sonnet [74] simulations and plotted in Fig. 3.3. It can be seen that choosing $W/(W + 2G)$ anywhere between 0.3 and 0.6 minimizes the attenuation constant of the CPW line while the characteristic impedance of the CPW line varies within the range of 64–44 Ω. As a result, $Z_{0,CPW}$ is chosen to be 50 Ω. By doing so, designing the input and output inverters becomes easier due to the symmetric structure.

Using three micro-channels, three different Galinstan bridges are placed on and around the middle of the CPW resonator symmetrically to achieve a slower phase velocity in the loaded region (Fig. 3.2(b), and (c)). A frequency down shift occurs due to this capacitive loading. By filling and emptying these three micro-channels with liquid metal, the resonator can be tuned. Except for the middle bridge, the other

two are filled with Galinstan (ON State) or Teflon (OFF state) in pair. This way, the standing-wave voltage on the loaded resonator is symmetrical and the maximum voltage level always occurs at the middle point of the resonator [71, 72].

The loaded resonator operating frequency is mainly related to four parameters. The length (l) and width (w) of each Galinstan bridge, the spacing between the bridges (S), and the vertical distance between the bridges and the CPW resonator (D) determined by the thin spin-coated PDMS layer. To better discern the effect of each parameter, the loaded resonator is simulated using HFSS [43] for different values of l,D,w, and S when all channels are filled with Galinstan.

The resonant frequency of a loaded CPW resonator is plotted against the changes of l, and D for initial fixed values of $w = 0.2$ mm, $S = 0.2$ mm in Fig. 3.4(a). The values of l, and D are chosen based on: (1) the largest frequency shift possible when loaded with Galinstan, and (2) the fabrication constraints for the spin-coated PDMS thickness. As a result, based on the information shown in Fig. 3.4(a), and the fact that smaller values for D result in higher sensitivity of the filter performance to fabrication errors, the parameters $l = 5$ mm, $D = 30$ μm are chosen for the filter design. Fig. 3.4(b) shows the resonant frequency of the loaded resonator versus w and S while the other two parameters are fixed this time. As can be seen, the resonant frequency variation increases when either w, and l or both increase or D decreases. However, the changes due to varying S are minor. Thus, the value of S is mainly limited by fabrication constrains. Final values of $w = 0.8$ mm, and $S = 0.8$ mm are chosen for the resonator. The goal of the above study is to achieve the highest possible tuning range. However, if high tuning resolution or equal spacing of the tuning states are of interest, a different sort of study is needed. Up to this point, the analysis is based on similar liquid metal length for the center and side bridges. By having different lengths for these three channels (still similar length for the side

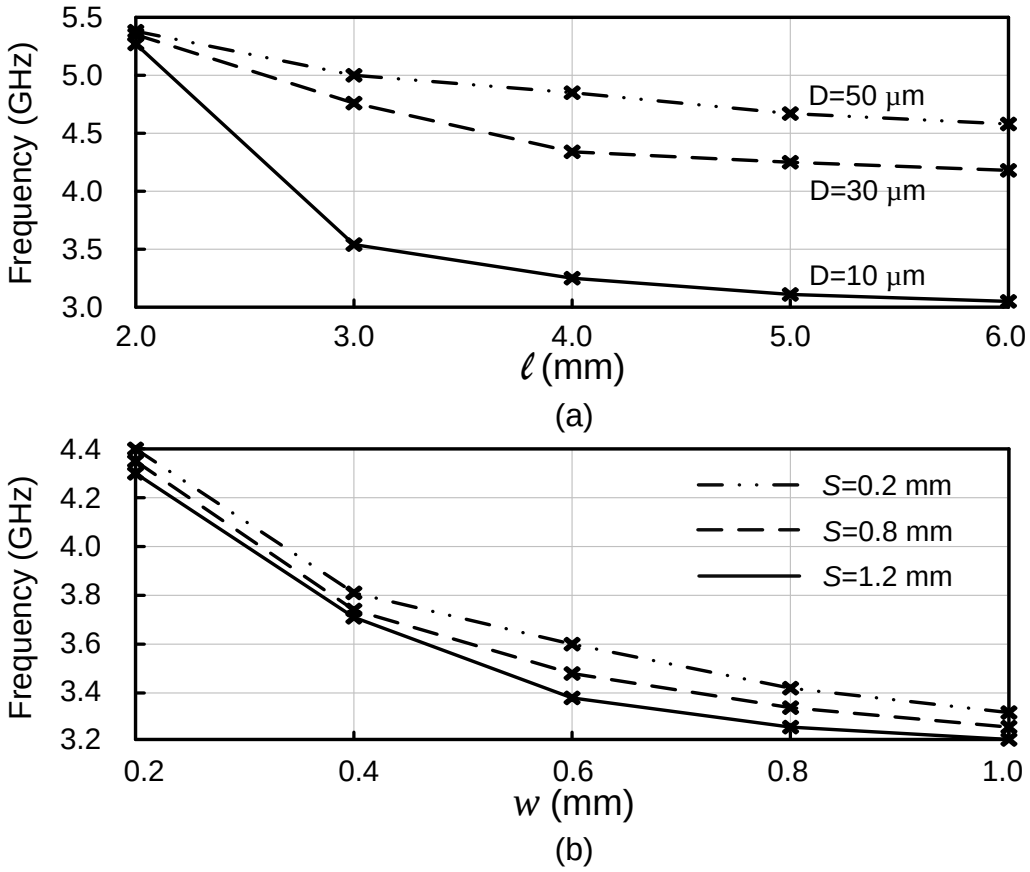

Fig. 3.4: Simulated resonant frequency of the resonator shown in Fig. 3.2(c) when all channels filled with liquid metal, with respect to (a) l, and D with fixed $w = 0.2$ mm, and $S = 0.2$ mm, and (b) w, and S with fixed $l = 5$ mm, and $D = 30$ μm chosen from (a).

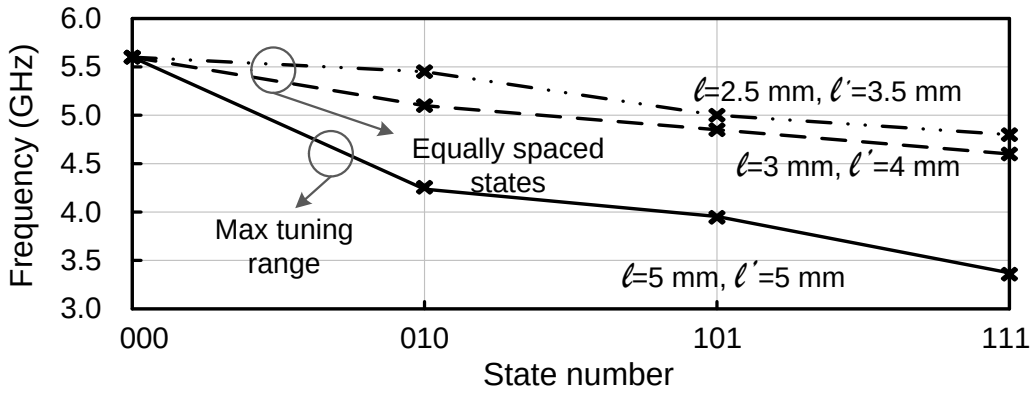

Fig. 3.5: Simulated tuning range of a resonator with respect to different bridge lengths or different tuning resolutions ($l = 2.5, 3, 5$ mm, $l' = 3.5, 4, 5$ mm).

Table 3.1: Simulated Resonant Frequency and Unloaded Quality Factor of One Reconfigurable Loaded Resonator.

State number	000	010	101	111
Frequency (GHz)	5.5	4.1	3.7	3.4
Q_U	102	93.5	88.6	83.3

channel pairs), both the tuning range and tuning resolution can be controlled. Fig. 3.5 shows different tuning ranges for three different possible length groups (l and l' refer to the lengths of the center and two side bridges, respectively). As can be seen, by decreasing the length of the channels, the tuning resolution increases while tuning range decreases. According to Fig. 3.5, using different lengths, and by employing more tuning bridges, a widely-tuned filter with a higher tuning resolution is also achievable.

In the rest of this section, the resonator with the identical bridge lengths is considered to achieve the highest possible tuning range. Table 3.1 shows the final simulated center frequency and unloaded quality factor (Q_U) for the resonator with $w = 0.8$ mm, $S = 0.8$ mm, $l = l' = 5$ mm, and $D = 30$ μm.

The height of the micro-channels is not a critical parameter and does not influence the resonance frequency or Q of the resonator. As a result, this parameter is mainly determined by the fabrication constrains to avoid blocked channels and is chosen to be $h_{ch} = 400$ μm.

3.1.2.3 Complete Filter Design and Simulations

Two loaded CPW resonators (overall 6 bridge channels) are coupled using shunt inductive inverters in order to form a two-pole 5% 0.1 dB ripple Chebyshev-like BPF. The CPW line comprising the resonator has the same characteristic impedance as of the input/output line ($Z_{0,CPW} = 50$ Ω). The design procedure in [71] results in input and output inverters with $L_0 = 0.65$ nH and interstage inverters with $L_1 = 0.2$ nH

at 5.5 GHz [circuit model is shown in Fig, 3.2(a)]. The series transmission lines with negative lengths due to inverters are absorbed into the unloaded regions of each resonator ($\Phi_1 = -41°$, and $\Phi_2 = -14.5°$ at 5.5 GHz) [72]. The shunt inverters are realized using narrow inductive lines connected between the center feed-line and the ground planes shown in Fig. 3.1(a). For the input/output inverters as the inductor value is large, the inductive lines are extended in the ground plane. The exact dimensions for each inductive inverter is found using full-wave simulations in HFSS.

In order to better understand the effect of the Galinstan bridges on the filter performance, the E-field distribution and current density on the CPW filter for the possible filled/empty channel configurations of the 4 states are shown in Fig. 3.6. As can be seen, by locating each Galinstan bridge over the filter resonators, significant E-field concentration occurs underneath each bridge. This is due to the capacitive loading effects of each Galinstan bridge. To further investigate this phenomenon, Fig. 3.7 shows the E-field strength in the $z-$direction and along the B-B' line in Fig. 3.1 and this time at a height of $D = 15$ μm. The E-field strength comparison between state 000 and the states in which at least one channel is filled with Galinstan (010, 101, and 111) is shown. It is observed that at the Galinstan bridge location, the E_z magnitude is at least 25 dB stronger. This high strength field concentration below the Galinstan bridges represents a capacitive loading and hence, a slower phase velocity in the loaded region, which ultimately means lower operating frequency for the filter.

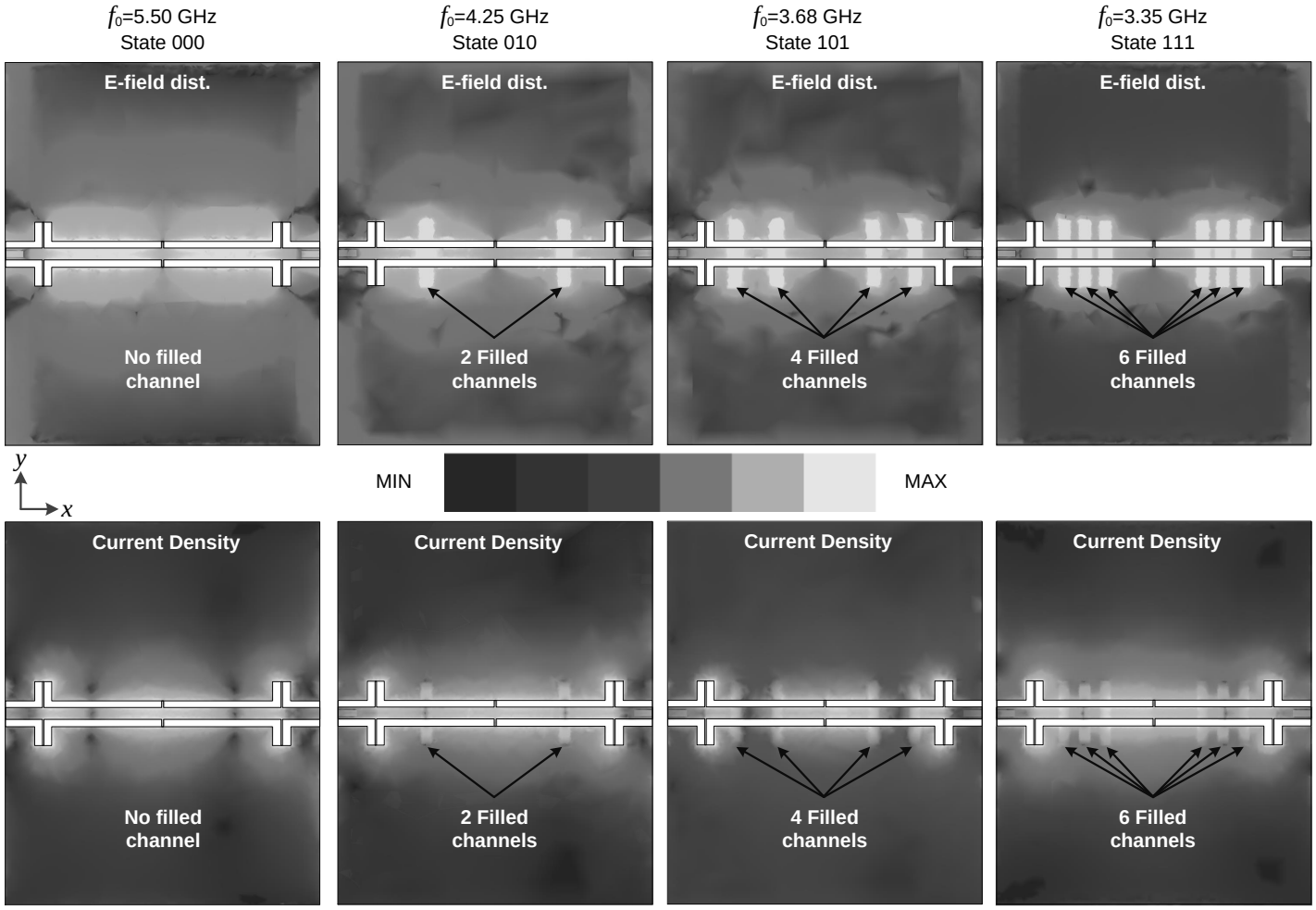

Fig. 3.6: Simulated electric field distribution and current density on the CPW filter for different filled/empty configurations (i.e. states 000, 010, 101, and 111).

Fig. 3.8 shows the simulated S-parameter results for the filter. An insertion loss of 2.4–4.8 dB is observed in the range of 3.4–5.5 GHz. The higher loss at lower frequencies is due to the higher loss factor (lower Q) for a loaded CPW resonator in response to the higher concentration of E-fields in the loaded regions.

3.1.3 Fabrication and Measurements

3.1.3.1 Fabrication

Filters are fabricated using 3D printer and standard soft lithography techniques as shown in Fig. 3.9(a). The circuit boards are fabricated using common PCB technology (Step 1). A 3D template (also mold) is designed in Solidworks[2] and printed layer by layer using a Stereolithography 3D printer named Envisiontec Perfactory Micro (Step 2). The picture of micro-mold is shown in Fig. 3.9(b) and this mold is reusable. The 3D printer makes the fabrication of device faster, easier and cheaper. The mold is cleaned using isopropyl alcohol (IPA) and left in heating oven at 65° C for at least 24 hours to remove any chemicals. PDMS solution is prepared by mixing Sylgard 184 (from Dow Corning) resin and curing agent in 10:1 ratio. PDMS solution is then poured over the micro-mold and de-gassed to remove air bubbles using a vacuum desiccator. PDMS is cured in heating oven at 65° C for two hours and peeled from the mold (Steps 3, 4). As a result, PDMS structure contains the channels, while the inlets/outlets are made by punching holes through the PDMS. A 30 μm thin layer of PDMS is spin-coated directly on the PCB circuit board and cured on hot plate at 65° C for 2 hours (Step 5). The PDMS structure by molding and the thin PDMS layer on PCB board are permanently bonded after oxygen plasma treatment [75] (Step 6). The alignment marks are used on PDMS structure and the circuit board to properly align channels over the substrate. Channel in-

[2]Solidworks 3D CAD, Dassault Systemes SOLIDWORKS Corp.. Waltham, MA, USA, 2014.

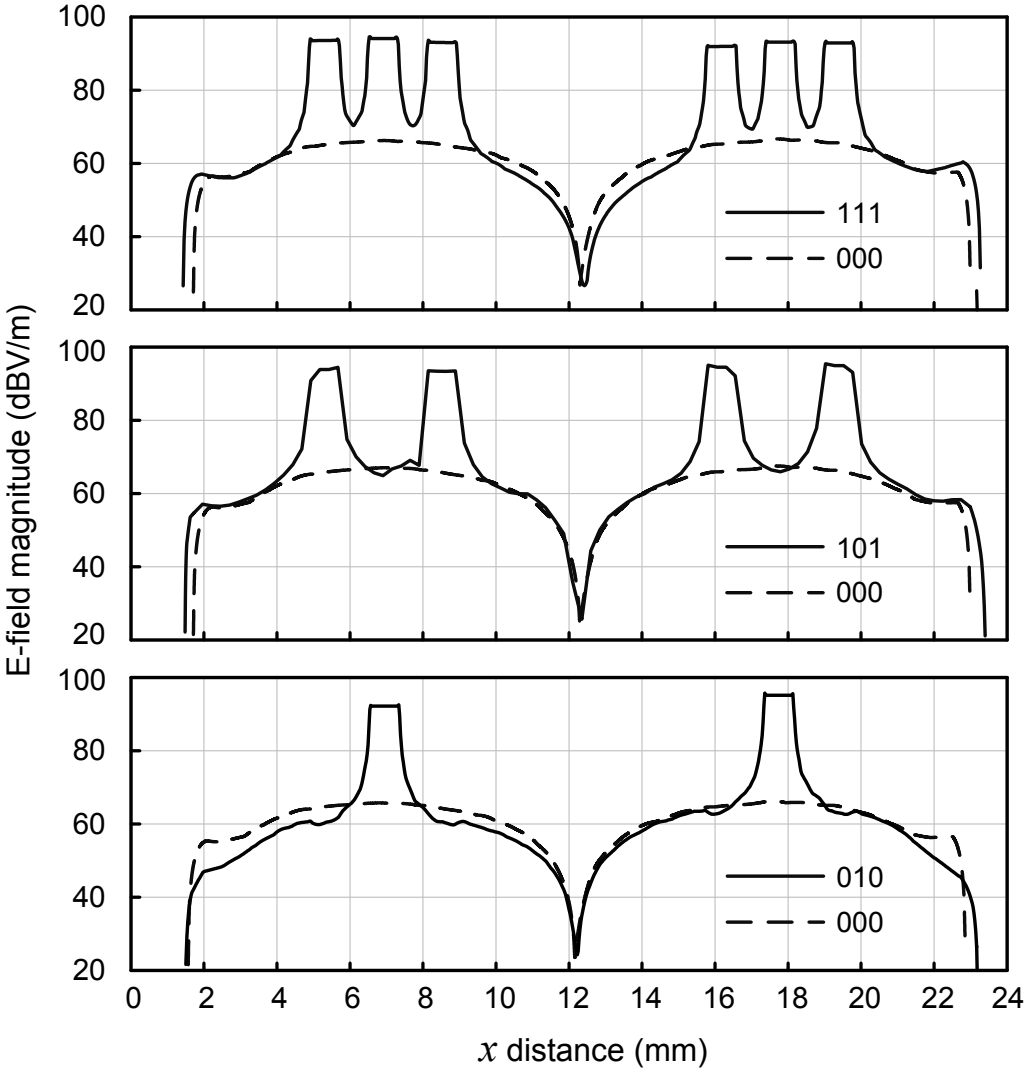

Fig. 3.7: E-filed strength in the $z-$direction and along the B-B' line (shown in Fig. 3.1), and at height of $D = 15$ μm. The curves are obtained using full-wave simulations in HFSS.

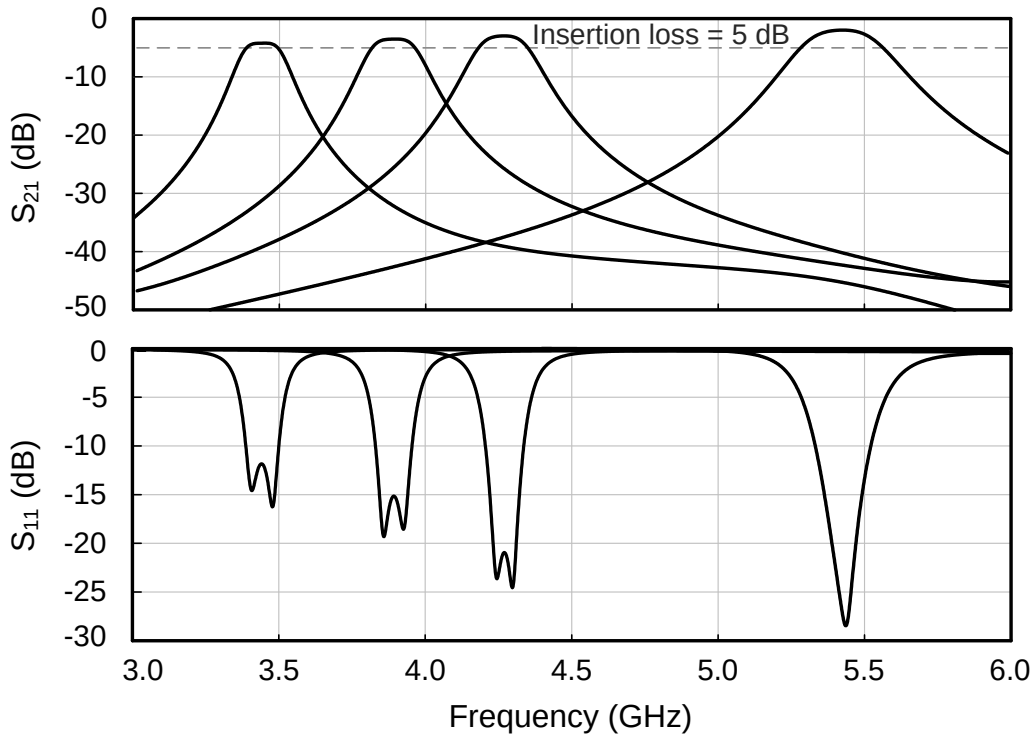

Fig. 3.8: Simulated S-parameter results for the proposed filter.

lets/outlets are connected to flexible tubing to inject/remove Teflon and Galinstan solution (Step 7). Two reusable syringes are used to inject/rinse the micro-channels with Galinstan/Teflon, respectively.

3.1.3.2 Experimental Results

The fabricated prototype of the filter [Fig. 3.10(a)] is measured using 3680 Antritsu universal test fixture and a 2-port network analyzer (Agilent N5230A). Fig 3.10(b) shows magnification of channels' configuration for the four measured states. The measured S-parameter results are shown in Fig. 3.11. The insertion loss is 5 and 2.6 dB at 3.4 and 5.5 GHz, respectively. The return loss is higher than 15 dB over the entire tuning range. The tuning range of the filter is 3.4–5.5 GHz (FTR=$f_2/f_1 = 1.6$). Also, Fig. 3.12 shows the wideband filter response for the low-

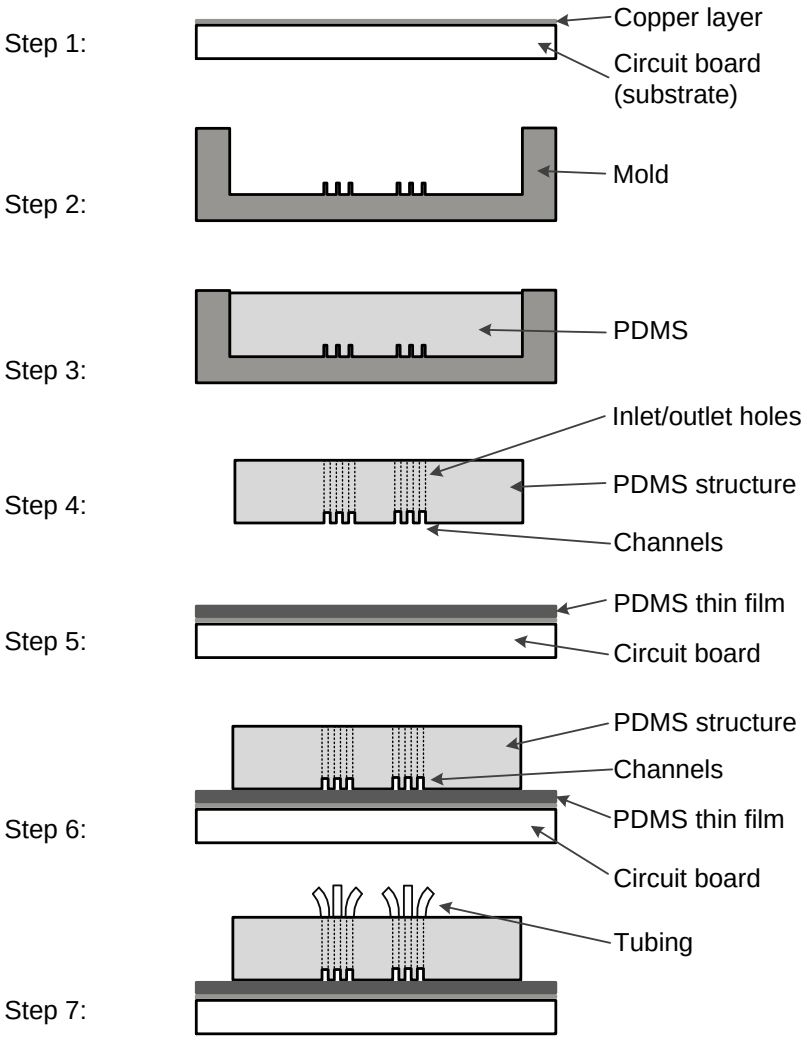

Fig. 3.9: (a) Step-by-step process showing side view for fabrication of miniaturized fluidic devices using 3D printed mold and soft lithography. (b) A template (mold) printed using 3D printer with small features for channels and alignment.

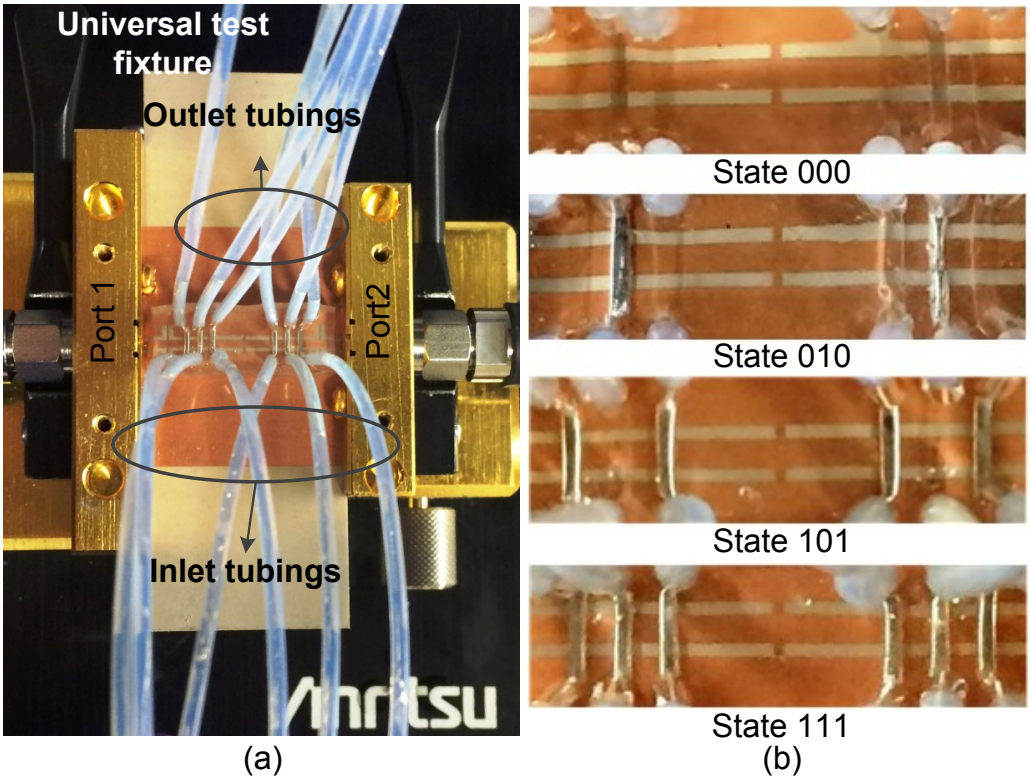

Fig. 3.10: (a) Fabricated filter prototype under test. (b) Magnification of micro-channels' configurations for different states.

est (000) and highest (111) states. The filter shows out-of-band rejection of better than 30 dB up to and even higher than the second harmonic for the lowest state, and better than 18 dB for the highest state. The measured center frequency and insertion loss of the filter are shown in Fig. 3.13(a) for each of the different 4 states. The measured relative BW of the filter for each state is presented in Fig. 3.13(b) and is in agreement with the simulation results. The filter shows an almost constant relative BW ($5 \pm 0.35\%$) over the tuning range.

3.1.3.3 Power Handling Characterization

The use of liquid metal tuning for high-power microwave applications was first demonstrated in [76] using a fluidically tunable frequency selective surface (FSS)

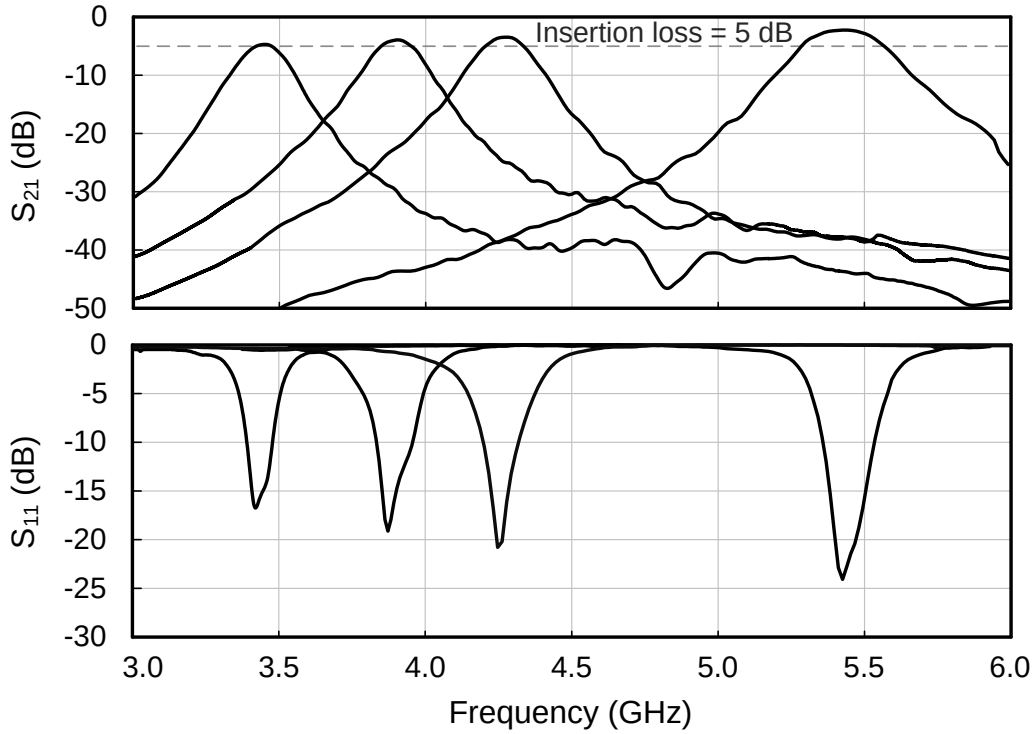

Fig. 3.11: Measured S-parameter results for the proposed filter.

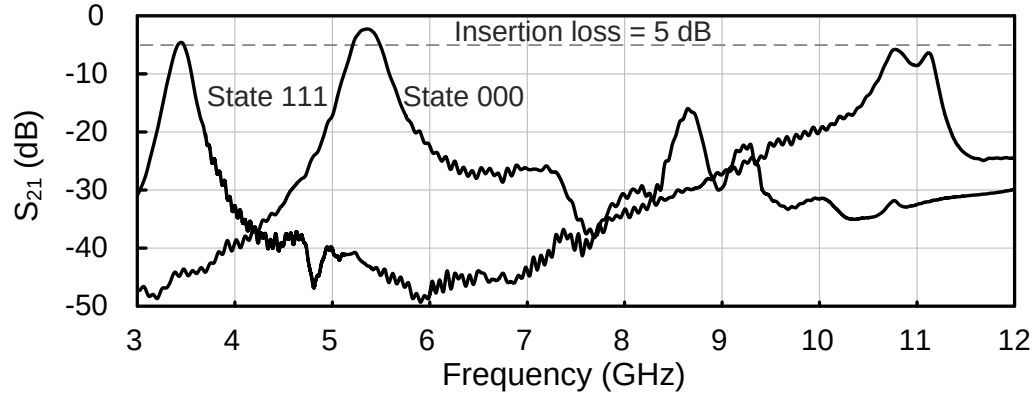

Fig. 3.12: Measured wideband response of the proposed filter for the lowest(000) and highest (111) operating states.

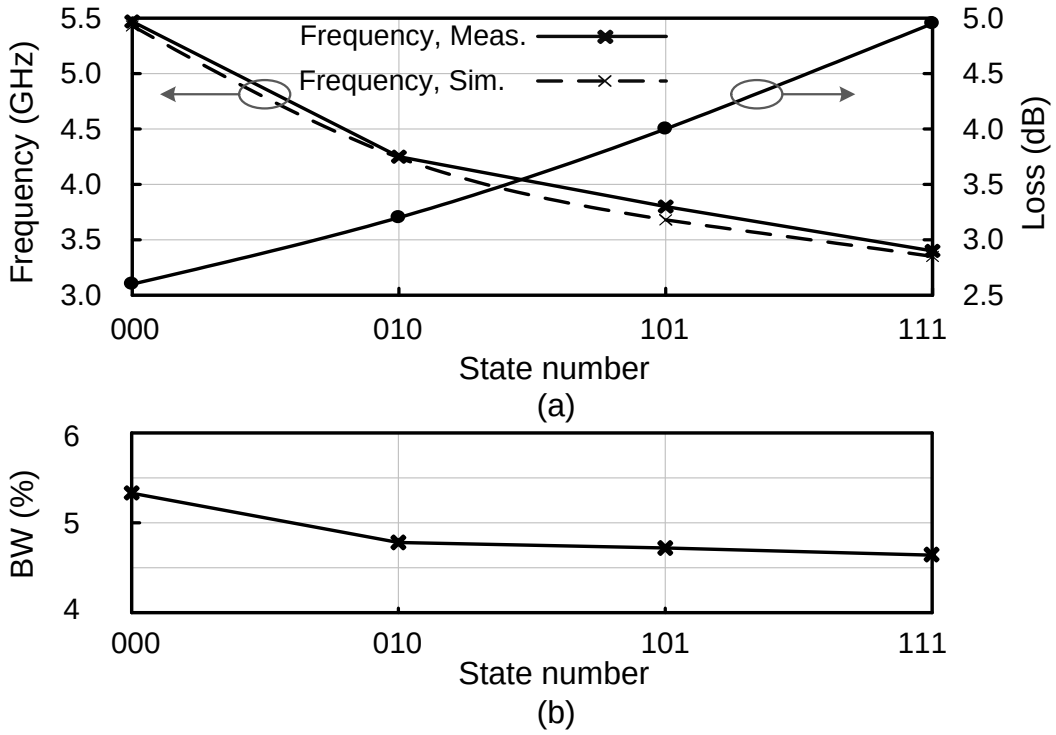

Fig. 3.13: (a) Measured center frequency and loss. (b) Measured relative bandwidth of the 4-filter responses.

structure. Since fluidically tunable microwave devices are linear mechanical structures they were expected to remain linear for short-duration high-peak-power excitations. However, neither the short-duration high-peak-power nor the high-average-power excitation characterization of the proposed fluidically tunable FSS device was provided in [76].

Nonlinear nature of a tuning structure is not the only parameter altering the response of the microwave structure when dealing with high-average-power input signals. The insertion loss of the microwave structure results in a subsequent loss of energy in form of heat. Depending on the value of average input power and the filter's insertion loss, the amount of thermal heating varies. If heated enough, the physical dimensions of the microwave filter, the tuning elements, or both might increase. Due to this thermal heating expansion the effective reactive loading of the liquid metal bridges can alter. Ultimately, this translates into change in the frequency response of the filter.

In order to address the power handling capabilities of the proposed tunable CPW filter, a similar setup to the one used in [1] and as shown in Fig. 3.14 is used. The power amplifier (PA) used in the high-power setup is a 45 dB gain power amplifier (Mini-Circuits ZHL-16W-42+S) with maximum output power of 16 W and P_{SAT} of $\sim$20 W at its 3 dB compression point. The output of the PA is protected using an isolator constructed using a high-power circulator (MECA-CS-3.000) with its 3rd port terminated in a 25 W power-tolerable 50 Ω load (MECA-407-7). The VNA frequency sweep amplified signal by the PA then passes through the filter-under-test and is attenuated by a 40 dB attenuator (Mini-Circuits BW-S30W20+ in series with BW-S10W20+) before entering the VNA's 2nd port. The insertion loss of the circulator, attenuator, and cables in addition to the gain of the PA are measured without the filter in the setup and are calibrated out from the measured S_{21} where

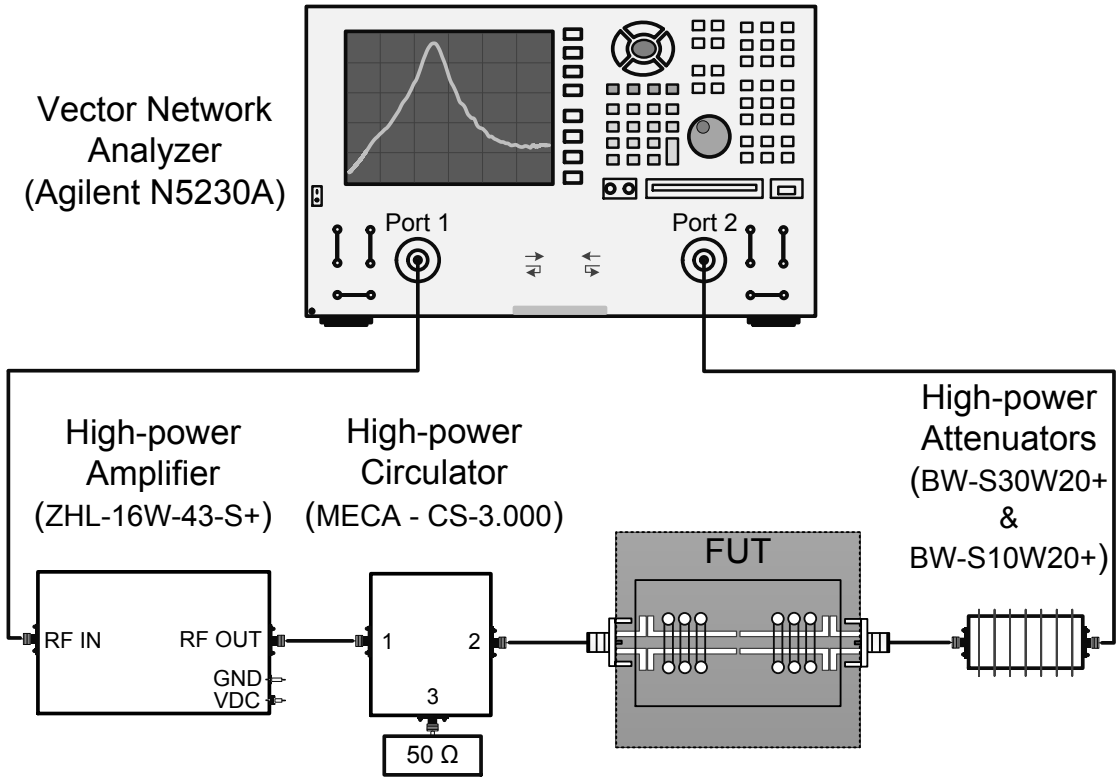

Fig. 3.14: Measurement setup for power-handling characterization of the proposed filter based on [1].

the filter is in the setup. SMA connectors were used for the power-measurements as the 3680 Antritsu universal test fixture cannot tolerate powers levels of more than 2 W. With this sort of setup measuring the reflection coefficient of the filter is not possible and thus is not presented here [1]. Inlet and Outlet tubings are removed from the structure after the Galinstan injection to make the structure more visible to the IR thermal imager.

Two different sweep setups for the VNA are used. First, the VNA's sweep time is set to be as short as 6 msec for a frequency span of 800 MHz (3.1–3.9 GHz) divided into 201 points. Therefore, the filter is excited at each of these 201 frequencies for a very small fraction of time. Also, for some of the frequencies the input signal is

rejected as the frequency span of the VNA is wider than the 10 dB bandwidth of the filter. Accordingly, this setup can reveal any possible issues caused by short-duration high-peak-power conditions such as deformation related to the Galinstan bridges. However, to study the high-average-power excitation conditions another frequency sweep setup is required. Fig. 3.15(a) shows the S_{21} response of the filter at state 111 and for different short-duration input power levels of 25, 35, 38, 40, 42, 42.5, and 43.2 dBm. The last two power levels are the PA's 1 dB and 3 dB compression point output power levels. Thus, the max power level that can be applied to the filter input is limited by the measurement equipment. The 1 dB and 3 dB compression effects are subtracted from the measured S_{21} results for these two input-power-levels. As can be seen in Fig. 3.15 (a), the filter shows very similar response for input-power levels of up to $\sim$21 W. In terms of any sort of visible physical deformations, no issues were observed by the authors during the measurement.

To study the high-average-power conditions, the sweep time of the VNA is increased such that the VNA takes 410 sec to sweep the frequency completely over a span of 600 MHz (3.1–3.7 GHz) divided into 41 points. The frequency span range for this setup is decreased to avoid huge reflections for the frequencies with a reflection of more than 10 dB. This way the filter is exposed to a high-level input power over the entire span range and there won't be frequencies at which the filter cools down since there is no significant reflection. The FLIR E-60 infrared (IR) camera is placed over the filter-under-test to monitor the temperature of the filter for different input-power-levels. Detailed multi-physics simulations using COMSOL [77] are performed to estimate the maximum temperature of the filter at different input-power-levels. This data is then used toward choosing the correct VNA sweep-time to provide the filter enough time to reach to its max temperature. The S_{21} results shown in Fig. 3.15(b) are the filter response for different input-power-levels and at the temperatures

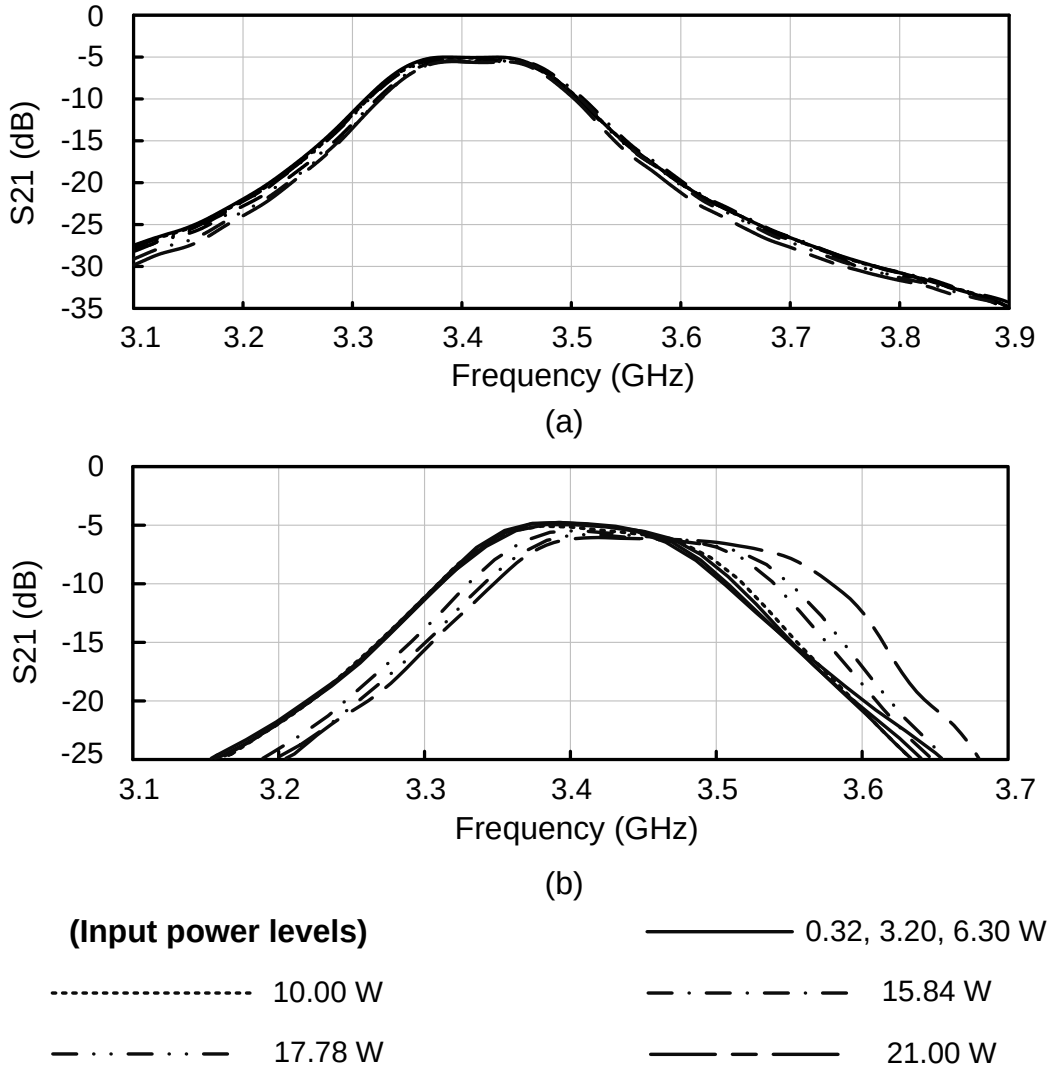

Fig. 3.15: Measured S_{21} of the filter at state 111 for 7 different input power levels for (a) short-duration excitation condition (6 msec over a frequency span of 800 MHz), and (b) high-average-power excitation conditions (410 sec over a frequency span of 600 MHz) and at temperatures shown in Fig. 3.16.

shown in Fig. 3.16. For input-levels lower than 10 W the S_{21} results are very similar and unchanged. A 0.3% variation in BW is seen for the 10 W. The results show that for input-power-levels of higher than 15.84 W at which the filter temperature becomes greater than 80° C the filter response is deviated.

The possible reason for this shift in frequency [see Fig. 3.15(b)] can be expansion of some of the elements, change in dielectric constant of Rogers dielectric or the PDMS structure, and/or change in conductivity due to thermal heating. Dimensional variations of different filter structures are studied using HFSS in order to estimate the reason for this frequency deviation. Since the expansion of PDMS will result in wider channels, even very small changes in PDMS physical dimensions shift down the frequency of the filter. Hence, PDMS expansion is less likely to occur. For the Galinstan, however, the situation is different. Expansion of an invariant amount of Galinstan may cause the Galinstan to start moving in the channel and due to surface adhesion part of it might move out of the channel area on top of the CPW resonator. The result of this probable phenomena can be slightly narrower Galinstan width inside the channel. The effect of this hypothesis has been simulated in HFSS and the results show that for slightly narrower Galinstan width inside the channels, the filter center frequency is increased. While the authors assume this to be the most-likely aftermath of thermal heating, finding the exact reason of the frequency shift at higher temperatures needs precise material, stress/strain, and heat transfer studies and experiments. However, loss of the filter is the main cause for the temperature increase in the filter structure, which ultimately results in response deviations. As a result, in the following section, it is discussed how each material used in the filter structure contributes to the loss of the filter. This way, it can be better understood how to increase the power handling tolerance of the filter even more.

Also, since the response deviations for the higher input-power-levels are caused

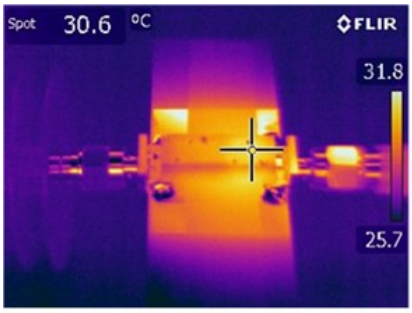

Input power = 0.32 W

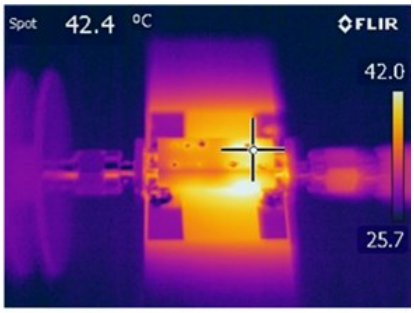

Input power = 3.20 W

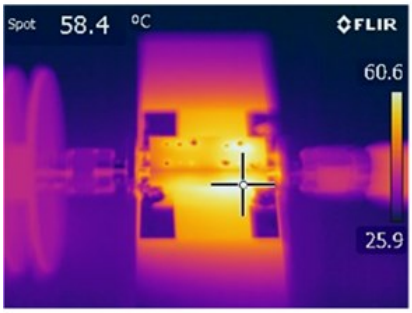

Input power = 6.30 W

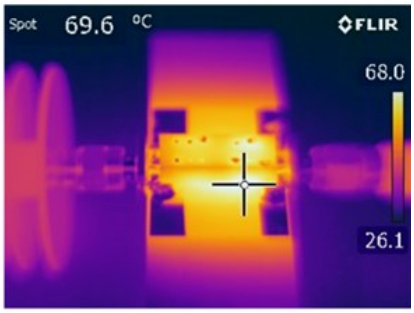

Input power = 10.00 W

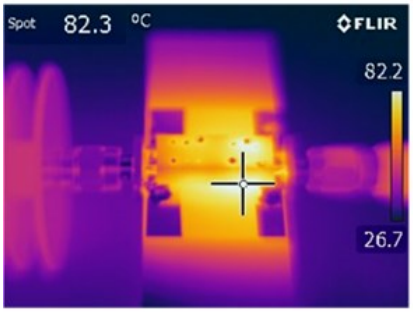

Input power = 15.84 W

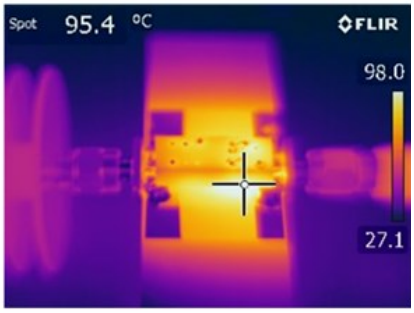

Input power = 17.78 W

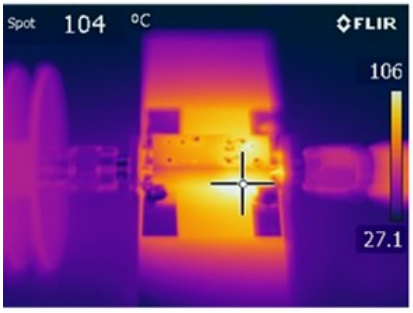

Input power = 21.00 W

Input power	Temp MAX
0.32 W	31.8 °C
3.20 W	42.0 °C
6.30 W	60.6 °C
10.00 W	68.0 °C
15.84 W	82.2 °C
17.78 W	98.0 °C
21.00 W	106.0 °C

Fig. 3.16: Measured steady state temperature of the filter for different input power levels at state 111. The input port of the filter is on the the right side in all IR-photos.

by thermal heating of the filter, with aid of a heat sink the filter might be used for even higher input-average-power excitation conditions.

3.1.3.4 Nonlinear Characterization

A setup similar to the one in [71] is used to measure the third-order intermodulation components of the microfluidically-reconfigurable CPW filter. For each tuning state, a two-tone signal was applied to the filter within the filter pass-band with a separation of 1 kHz (or 1 MHz), and the third-order intermodulation products were measured using the Agilent-E4446A spectrum analyzer. As was expected from the highly-linear nature of the filter and the reconfiguration method employed, the third-order intermodulation level was below the noise level of the spectrum analyzer used for all the operating states[3]. Consequently, it is impossible to measure the IIP_3 of such a linear passive filter for any of the operating states using the common test setups in literature. Indeed, it can be concluded that the IIP_3 of the filter is always > 65 dBm, which is very hard to measure. Such a conclusion is made for similar filters employing MEMS switches in [41, 71, 72], and it is shown that the intermodulation products in circuits employing mechanical-tuning[4] components are very hard to measure.

3.1.4 Discussion

As any other emerging technology, there are some practical concerns regarding fluidics-based microwave tuning. In this section, some of these concerns are addressed based on authors modeling and measurement experience. First a detailed loss budget Table is used to discusses the loss of the filter in detail, thermal studies of the filter

[3]As long as the RF mixer of the spectrum analyzer is not saturated by the input signal with a maximum power-level of 15 dBm.

[4]Both microfluidic-based and RF MEMS devices are considered mechanical based components in contrast with semiconductor ones.

under high-power conditions are provided. This way the main limiting factor in further increasing the power tolerance of the filter is found. Afterwards, discussions over concerns such as durability, switching speed, and repeatability are presented.

3.1.4.1 Loss Budget of the Microfluidically-reconfigurable Filter

While the high-power measurements presented in the previous section prove the high-power tolerance capabilities of this tuning method, they cannot help with understanding where most of the power is lost inside the filter, and whether there can be something done to reduce the loss and thus the temperature increase. Knowing such information would help to improve the filter design, in order to employ this tuning method for even higher input power levels. Thus, a detailed loss budget information of the filter is needed to understand the contribution of each material to the total loss of the filter. This information is tabulated in Table 3.2 using full-wave simulations of the filter in COMSOL. By performing simulations, once considering no loss for any material and another time considering loss for a particular one, its contribution to loss is found.

The largest contributor to the loss is the PDMS structure, and second largest is the copper/substrate loss. The SMA connector loss is also included in the simulations and is a part of the reflected/radiated loss. As the filter is designed at 5.5 GHz, the filter parameters and dimensions are best matched to satisfy the desired values at 5.5 GHz. As a result, the loss of the filter degrades as it is tuned to lower frequencies, even in the case of loading using lossless materials.

This information suggests that either by decreasing the PDMS loss tangent (currently $\tan\delta = 0.015$), or by using a different topology in a way that the EM fields are more isolated from the PDMS structure, part of the loss which is related to PDMS can be lowered/minimized. For example, same tuning method can be applied to an

SIW filter by which a much lower loss in comparison with the presented filter can be achieved [78]. Lower loss for the filter, ultimately means higher power tolerance capabilities.

In order to better understand where the power is lost and how the filter is heated up in the high-average-power excitation conditions, Fig. 3.17 shows the temperature, and the Isothermal contours inside the filter structure. As can be seen, the highest temperature is where the fields are maximum, at which the Galinstan bridges are located. Lowering the loading effect of the Galinstan bridges by relocating these bridges, decreases the temperature gradient in the area where Galinstan bridges are located inside PDMS. Less loading of the resonator means lower insertion loss and as a result smaller heat dissipation in both Galinstan and PDMS. This translates into a filter capable of handling higher power levels than 10 W. However, at the same time, less loading means less frequency tuning. Hence, there is a trade-off between the tuning range and the power handling capabilities of the filter. A similar trade-off also exists between the size of the filter and the power handling capabilities. By increasing the size of the filter, filter's maximum tolerable power increases. However, this comes with the price of sacrificing miniaturization which might be equally important in the case of a portable transmitter system.

3.1.4.2 Repeatability, Reliability, and Durability

The repeatability of this reconfiguration method needs to be addressed, as there have been issues reportedly with Galinstan being oxidized inside the channel [66,67]. While it is true that the outer layer of Galinstan oxidizes quickly, Teflon can be used in order to coat this outer layer and avoid the oxidization process. This method is used previously and is shown to be effective in terms of minimizing the residues left behind in the channels [66]. In order to address this issue, two micro-channels filled

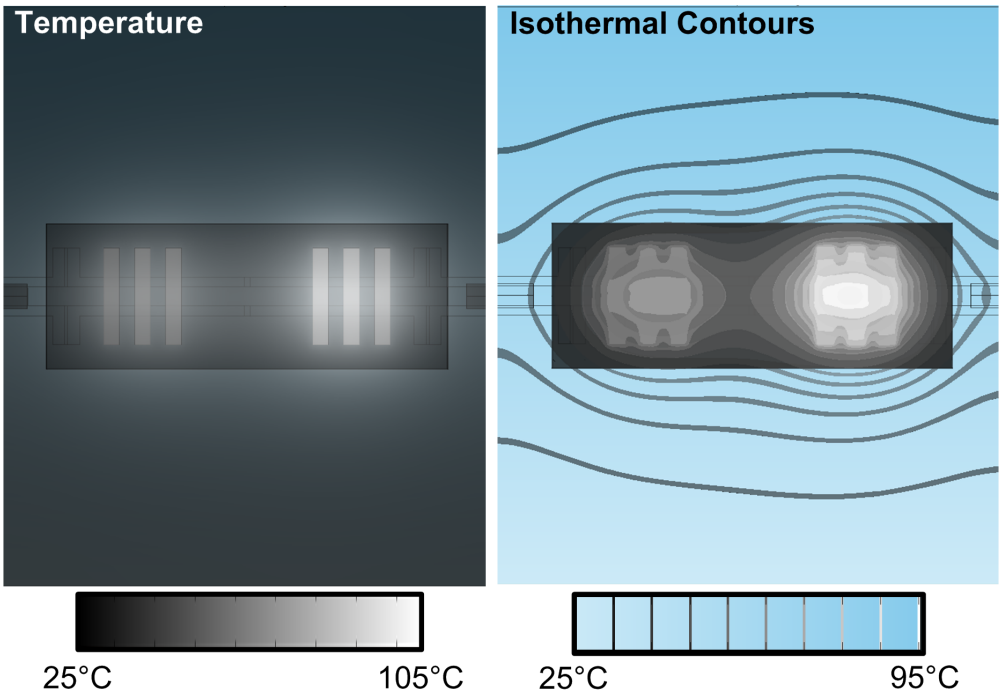

Fig. 3.17: Simulated temperature of the structures' materials (left) and the Isothermal contours within the structure (right). The graphs are generated using COMSOL simulations and under an input power of 21 W applied through the right port.

Table 3.2: Simulated Loss Budget of the Microfluidically-reconfigurable CPW Filter. Loss Values are All Stated in dB. The PDMS Structure is the Largest Contributor to the Loss

State number	Frequency (GHz)	Reflected/Radiated	Copper/Substrate	Galinstan	PDMS	Total Loss
000	5.50	0.10	1.05	0.00	**1.20**	2.35
010	4.25	0.10	1.30	0.10	**1.55**	3.05
101	3.68	0.20	1.40	0.40	**1.80**	3.80
111	3.35	0.20	1.70	0.60	**2.30**	4.80

with Galinstan in state 010 were evacuated by a rinse of Teflon solution and refilled with Galinstan for 5 times. Each time both measured results of the non-filled and filled states were compared with the original ones[5] and no significant difference was observed. Hence the method seems to be an effective one at least for experimental purposes, or the applications in which the switching speed is not of concern.

One other issue is reliability of the filter exposed to input signals with continuous high-power levels at the loaded states. As mentioned before, Fig. 3.16 shows that for the case in which the input power is ∼10 W the temperature of the filter increases up to $\sim 70°C$. However, Galinstan changes its physical state either at temperatures $< -19°C$ or $> 1300°C$. This suggests that even at temperatures as high as $\sim 100°C$, there won't be any change in physical properties of Galinstan. The filter channels at state 111 were emptied from Galinstan easily using Teflon rinse and no issues such as stiction of Galinstan after being exposed to high-power conditions were observed. Also it is noteworthy that the distorted filter response at power levels higher than 15 W as shown in the previous section, will move back to normal once the high-power excitation condition is removed.

Also, in order to examine the durability of the reconfiguration method presented, the fabricated prototype with the channels filled at the configuration of state 111

[5]Originally non-filled and the state 101 after first filling.

were left on the measurement bench at room temperature for a 30 days period of time. After this time laps, the filter measured S-parameter results did not differ from the initial results shown in the previous section. Also, the channels were successfully evacuated using pressurized air followed by a rinse of Teflon solution. Fresh Galinstan was injected into the channels and no significant difference in measured results was observed.

3.1.4.3 Switching Speed

Generally, one of the most important issues regarding the liquid-based tuning is the switching/tuning speed. The semiconductor/MEMS switches can perform at switching speeds in the order of ∼1–100 ns/1–300 μs, respectively. However, the liquid-based methods have a much lower speed (In the order of couple of seconds). It has been shown in [79] that even by using micro-pumps the speed of this method is significantly lower due to the kinetic operation of the pumps. However, in the same paper, the semiconductor-based and fluidics-based methods are compared from other aspects as well and it is shown that the liquid-based method has bold advantages in terms of size, electrical power consumption, and efficiency. This suggests that this method can be useful in applications where the switching speed is not that of concern.

Also, more recently, a new method for moving Galinstan inside the micro-channels was presented in [34, 80] where a single voltage is used to move Galinstan faster (0.8 mm/s) and easier than the pressure driven methods. The advantage of this method is that once the liquid metal and the electrolyte are injected into the channel there won't be any other injections needed. Thus the switching speed in this method is only limited to the movement speed of the liquid metal inside the channel and not the injection time. This method is based on continuous electrowetting

of Galinstan inside the micro-channels and can be utilized with the same micro-channel topology proposed in this section. As presented in [34, 80], by the aid of an electrolyte, and just a single excitation voltage the liquid metal moves inside the channel without any residues left behind. The drawback of this method, however, is that the electrolyte itself is a lossy material and further increases the insertion loss of the filter. Ultimately higher insertion loss would reduce the power handling capabilities of the filter. As a result, it is very important to make considerations in choosing the location of the electrolyte well when designing such filters.

3.1.5 Conclusion

A microfluidically-reconfigurable CPW band-pass filter is introduced. The liquid metal Galinstan is used to load the CPW resonator in order to achieve both miniaturization and reconfigurability. Tuning range of 3.4–5.5 GHz using four different states is achieved for the filter. Measurements verify that the proposed filter is suitable for power applications with input power levels as high as 10 W without any considerable change in S_{21} results. To the best of author's knowledge, this is the first verification of liquid tuning microwave filters for high-power applications.

3.2 Miniature and Reconfigurable CPW Folded Slot Antennas Employing Liquid-metal Capacitive Loading

3.2.1 Introduction

Due to the ever increasing frequency band requirements of modern portable wireless systems, the antenna solutions for these need to have small form factor while covering multiple frequencies. An ideal remedy in such systems is a miniature antenna with the frequency tuning/switching capability over multiple bands.

Folded slot antennas have four times smaller input impedance than slot antennas. As a result, they are easier to match to 50Ω, and have wider bandwidth in comparison to microstrip antennas. Due to their larger metal surface they have very low conductive loss, resulting in high efficiency [81]. The existing work in the area of miniaturized *CPW-fed slot* antennas includes employing E-shaped feeding structures instead of the conventional T-shaped ones [82], using stepped impedance resonators [83], slit or strip loading of the slot [84], using reactive terminations and truncated bilateral ground plane [85], and loading the radiating slot antenna using interdigital capacitors [86]. Among these, the highest size reduction factor is ∼60% [82, 84]. None of the above mentioned methods is applied to the *original CPW folded slot* antenna introduced in [81].

Also, despite the advantages of CPW folded slot antennas over slot and microstip antennas, their use as reconfigurable/tunable antennas is hindered due to their geometrical limitations. For instance, in [87], the frequency of a CPW folded slot antenna is switched in the limited range of 5.25–5.775 GHz using p-i-n diodes. Capacitive loading using lumped elements similar to what is presented in [35] for slot antennas seems to be more challenging to apply to CPW folded slot antennas due to their geometry. Also, due to the same reason, the miniaturization methods

presented in [82–86] seem not to be very efficient to achieve a miniature widely-tunable/switchable antenna. Accordingly, exploring a wide-range tuning/switching method applicable to the miniature versions of this type of antennas seems to be interesting.

More recently, the use of liquid metal in the design of tunable/reconfigurable antennas has become popular [88–92]. This tuning method has two main advantages over the conventional tuning elements such as p-i-n diodes [60], varactors [35] and MEMS switches [37]. First, since this technique is highly linear, it is promising for high power RF applications. Second, employing soft materials using common technologies can result in flexible and wearable tunable antennas [64]. The existing works in the area of liquid metal tunable antennas employ various approaches to achieve tunability. For example, in [88], a fixed amount of liquid metal is trapped inside a PDMS structure. By stretching the PDMS structure, the physical length of the metallic part is increased. Accordingly, the frequency of the antenna is decreased. In [89], the parasitic director and reflector elements are made movable by the aid of liquid metal mercury (Hg) to steer the beam of a circular Yagi-Uda array. In [90], a monopole antenna is introduced. The monopole antenna is formed using a channel filled with liquid metal and by changing the physical length of the antenna using pumps different operating frequencies are achieved. In [91], a microchannel is placed perpendicularly on top of the slot antenna. By filling the channel with eutectic gallium-indium (EGaIn), it acts as a non-ideal RF-shortening switch and decreases the physical length of the slot antenna. The result is a higher operating frequency for the antenna. However, due to the parasitics of the switching method, another non-desired mode is also excited at a lower frequency. In [92], an extension of liquid metal is added to the fixed printed patch antenna to increase the patch size and decrease the operating frequency.

The major idea behind the tuning methods in [88–92] is either based on physically reshaping the antenna elements, or using the liquid metal as a shortening switch. One other approach is based on using the liquid metal as a reactive load on top of the antenna resulting in both miniaturization and switching/tuning [93].

Liquid metals are not the only fluidics used for tuning antennas. In [94, 95], micro-channels on top of an annular slot antenna are used to place different dielectric liquid materials on top of the antenna. Loading the antenna with different dielectric constants shifts both frequency bands of a dual band slot antenna in [94]. By re-designing the channel configurations, independent tuning of each band is also achieved in [95].

This section investigates the application of liquid metals in both miniaturization and tuning of CPW folded slot antennas. This method was first proposed by the authors in [93] to switch the frequency of a folded CPW slot antenna in the range of 2.6–5.8 GHz. Here, in the miniature version, two micro-channels filled with Galinstan load the antenna to form a high-strength Electric field between the Galinstan bridges and the CPW slot antenna. This results in reactive loading of the antenna and shifting down the operating frequency. The Galinstan bridges are completely sealed up afterwards to achieve a miniature CPW folded slot antenna with a miniaturization factor of 85%. In the reconfigurable version, two pairs of the micro-channels are used to load the antenna. By using different configurations of filled and empty channels three different frequencies of 2.4 GHz, 3.5 GHz, 5.8 GHz are achieved. To the best of author's knowledge, this is the first presentation of a microfluidically-loaded miniaturized antenna and the most compact CPW folded slot antenna with a very wide switching range.

3.2.2 Liquid-Metal-Loaded Miniature Antenna

3.2.2.1 Antenna Topology

Fig. 3.18 presents the layout of a microfluidically-loaded CPW folded slot antenna. The antenna is based on a 1.53 mm thick Taconic TLY substrate ($\epsilon_r = 2.2$, $\tan\delta = 0.0009$). Two micro-channels are placed on top of the CPW folded slot antenna using two separate PDMS structures. In order to avoid the stiction of Galinstan to the walls of micro-channels, a Teflon solution is used as a lubricant to locate the Galinstan into its desired location (Teflon AF 400S2-100-1, 1% Teflon powdered resin dissolved in 3M FC-40 from DuPont). The PDMS structures are bonded to the antenna circuit board using a very thin [D = 30μm as can be seen in Fig. 3.18(b)] spin coated PDMS ($\epsilon_r = 2.68$, $\tan\delta = 0.004$) layer. Physical dimensions of the Galinstan bridge, its location, and the spin coated layer thickness control the antenna miniaturization as will be studied in the following.

3.2.2.2 Reactive Loading Using Galinstan Bridges

The first resonant frequency of a non-loaded CPW folded slot antenna can be found by [81]

$$f_0 = \frac{c}{(p\sqrt{(\epsilon_r + 1)/2})} \tag{3.1}$$

where c is the speed of light in free space, p is the perimeter of the folded slot antenna [81], and ϵ_r is the substrate permittivity. Equation (3.1) underestimates the results of full-wave simulations by a few percents as the effect of the CPW feed line is not taken into account [81]. The feedline slightly reduces the perimeter of the folded slot antenna, resulting in a higher resonance frequency. Thus, once the approximate design parameters are found using (3.1), 3D full-wave simulations must be used to achieve the exact resonance frequency of interest. A CPW folded slot

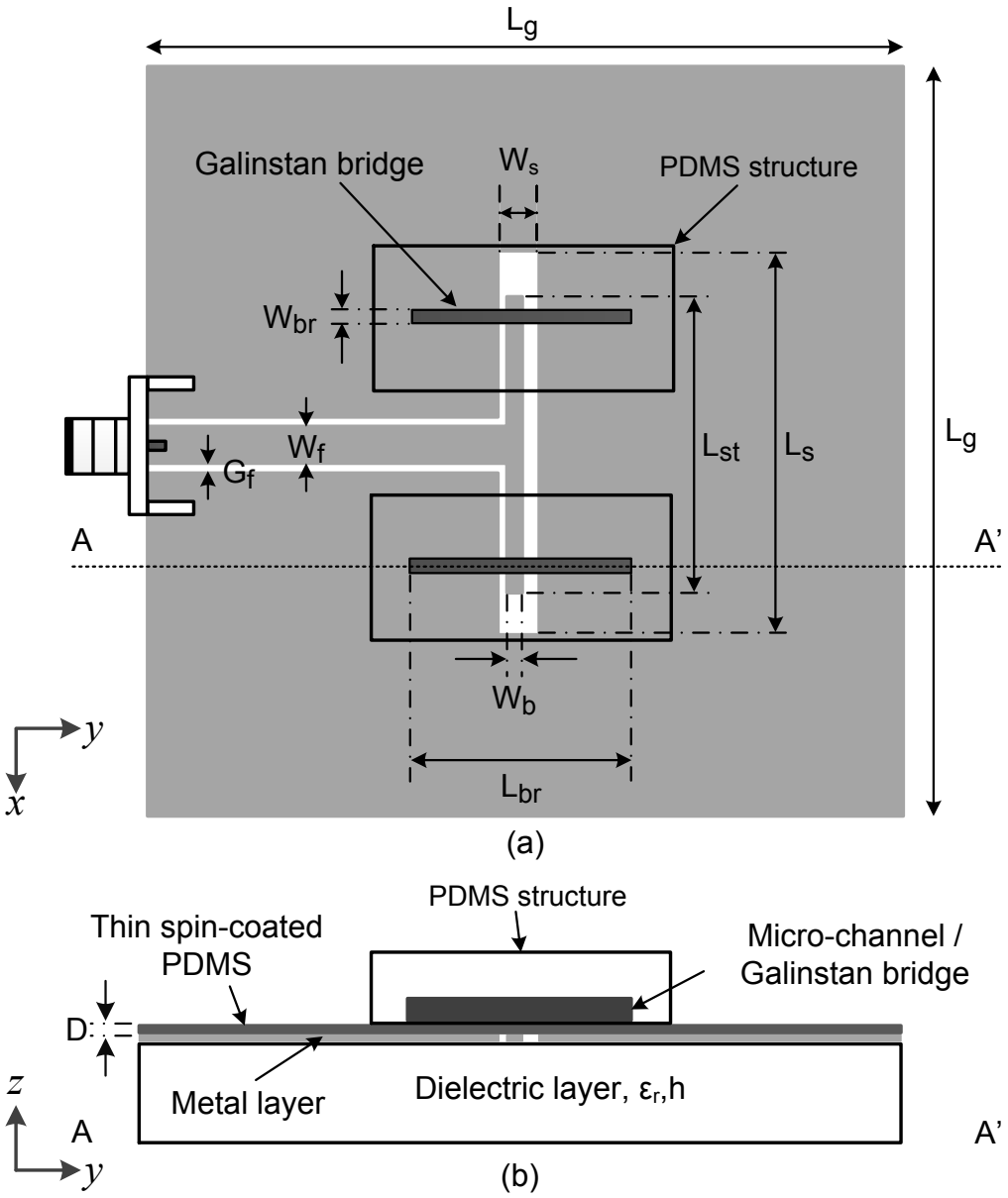

Fig. 3.18: Topology of a CPW folded slot antenna loaded with two micro-channels. (a) Top view. (b) A-A' cross section.

Table 3.3: CPW Folded Slot Antenna Parameters.

L_g	40 mm	W_s	2 mm	L_{br}	12 mm
L_s	20 mm	W_b	0.5 mm	W_{br}	0.8 mm
L_{st}	18 mm	W_f	2.35 mm	G_f	0.15 mm

antenna is designed based on (3.1) and full-wave simulations using HFSS [43] to achieve a resonance frequency of ∼5.8 GHz without any loading. Parameters W_f and G_f are sized to provide a CPW feedline with $Z_{0,CPW} = 50\Omega$. The dimensions of the designed antenna are shown in Table 3.3.

Since the length of the Galinstan bridges is finite, each bridge can be modeled as a quasi-TEM transmission line with length L_{br} and width W_{br} as shown in Fig. 3.19(a), and (b). The TL model of one Galinstan bridge is shown on the B-B' cross section view of the channel's physical layout for a better perception. As can be seen, the PDMS spin coated layer acts as the dielectric layer for the Galinstan TL. Due to the small height of the PDMS spin coated layer (D = 30μm), and its low dielectric constant ($\epsilon_r = 2.68$), the input impedance of the TL is expected to be very small. Based on the physical dimensions of the Galinstan channel, the method in [73] is used to estimate the characteristic impedance of the Galinstan TL (Z_{0CH}). Consequently, knowing the length and intrinsic impedance of these TLs, their effects on the antenna can be studied. In order to do so, TL model of each Galinstan bridge is inserted into the TL model of a CPW folded slot antenna and the final model shown in Fig. 3.19(c) is used. However, this model does not take into account the effect of the antenna feed structure, the PDMS structures (except the spin coated layer) and the radiation characteristics, which all affect the resonance frequency of the antenna. Nonetheless, the results achieved using this method are in good agreement with the ones obtained from full-wave simulations as will be discussed later.

The intrinsic impedance of the CPW folded slot antenna is calculated based

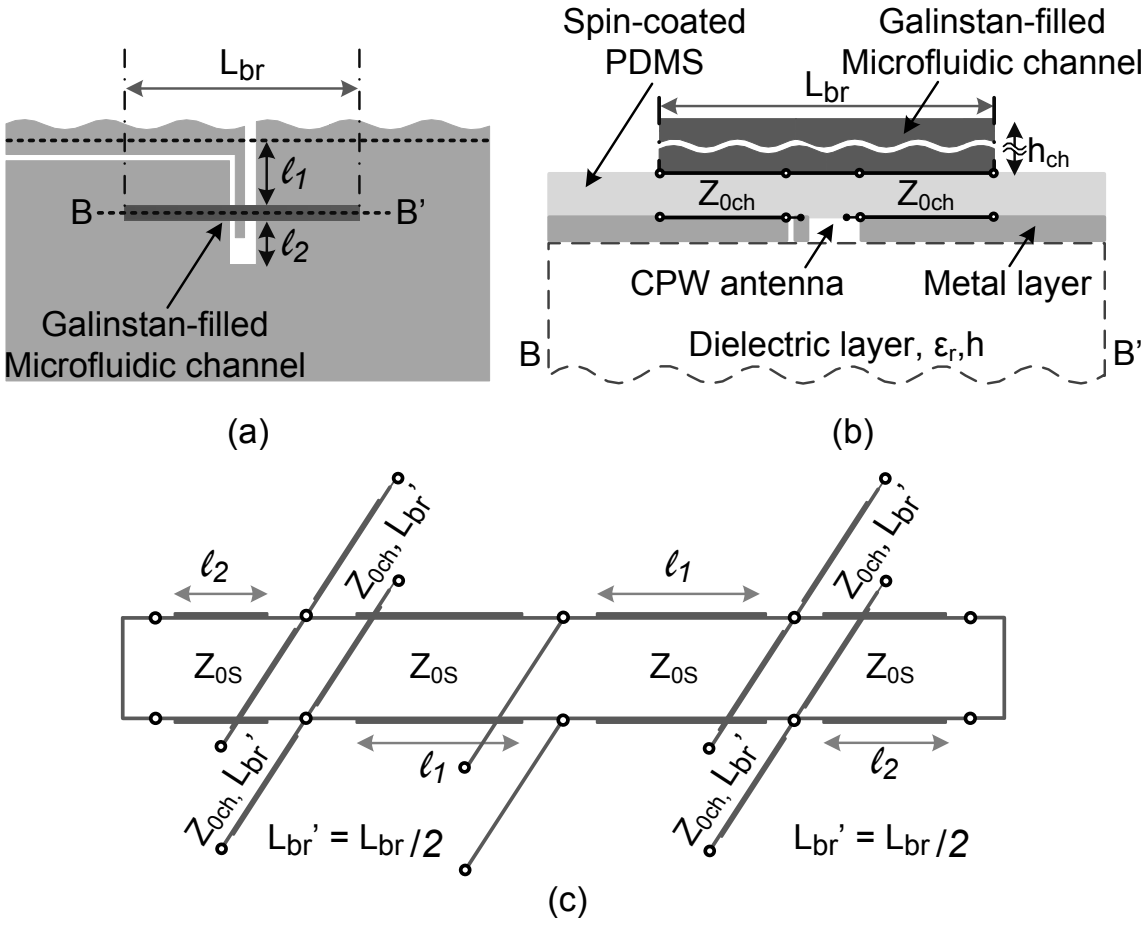

Fig. 3.19: (a) Top view of a Galinstan bridge over a CPW folded slot antenna. (b) The TL model of the Galinstan bridge overlaid on the B-B' cross section view of the Galinstan bridge. (c) The TL equivalent model used for the Galinstan loaded CPW folded slot antenna shown in Fig. 3.18.

on [73, 81]. The input impedance of the two open-ended stubs, seen by the CPW folded slot antenna can be controlled by changing the length of the Galinstan bridges.

In order to better discern the effect of the Galinstan bridges on the performance of the antenna, the TL model shown in Fig. 3.19(c) is simulated for different bridge lengths and locations using Agilent's ADS circuit simulator [62]. The TL model simulation results in Fig. 3.20(a) show that decreasing the length of the Galinstan bridge results in lower capacitive loading and thus less frequency down shift. The dependence of the first resonance frequency of the CPW folded slot antenna to the height of the spin coated PDMS layer is also examined in Fig. 3.20(b) using the TL model simulations. In order to do so, the intrinsic impedance of the transmission line constructed using the Galinstan bridge was calculated using [73] for three different spin coated layer thickness (D) values. This data shows that by decreasing this height, and as a result, by decreasing the intrinsic impedance of the Galinstan bridge TL, the capacitive effect of the Galinstan bridges on the antenna increases; hence, higher frequency down shift occurs. Fig. 3.20 also shows that by increasing the distance between the slot edge and the Galinstan bridge (l_2), the loading effect of the Galinstan bridges increases. This is mainly due to the fact that by increasing l_2 the loading bridges are located closer to the center of the slot antenna where the E-field distribution has its maximum value. While maximizing this parameter will result in the maximum frequency down shift, there is a trade-off between this factor and the gain of the antenna which is also affected by the Galinstan bridges.

These effects can be better justified by looking at the Galinstan bridge TL model's circuit equivalent. Using the model presented in [96], a simple microstrip line can be modeled by two shunt capacitors and an inductor in series (see Fig. 3.21). The slot antenna is neglected for this purpose as it only adds two series capacitor and does

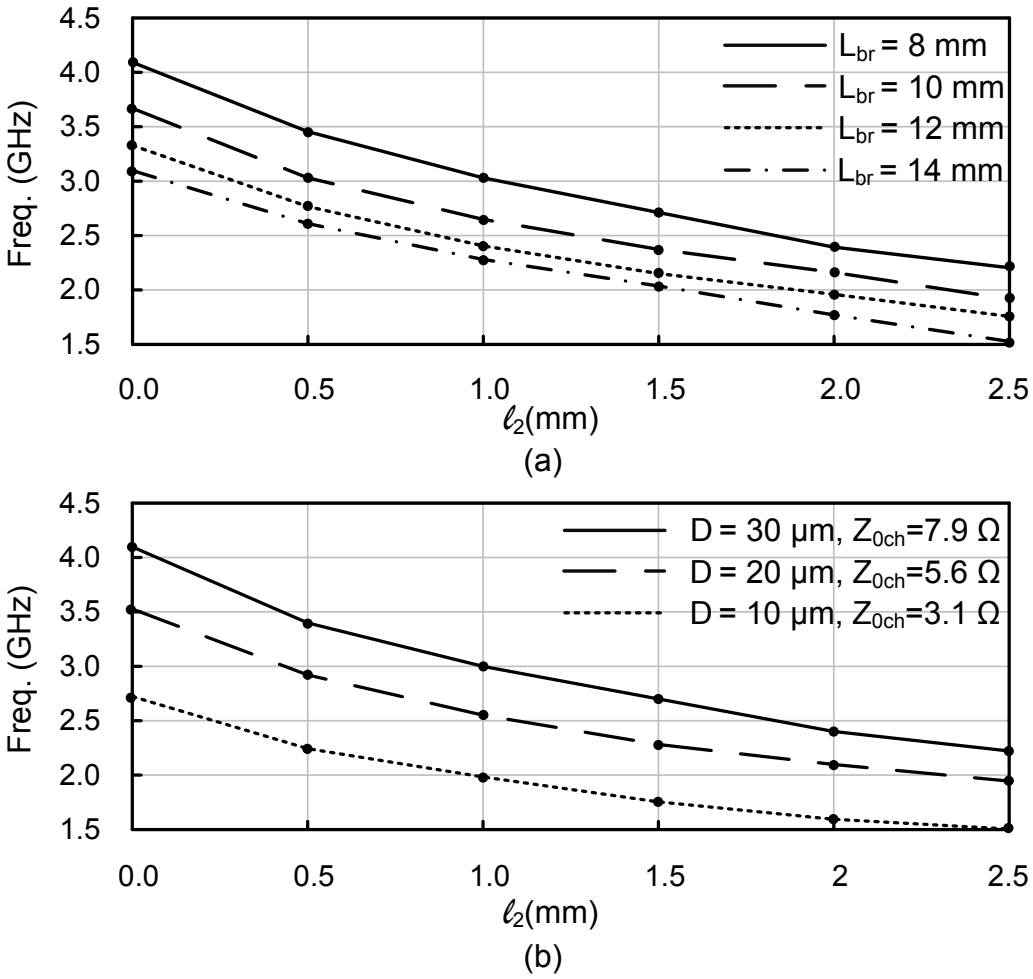

Fig. 3.20: First resonance frequency of a CPW folded slot antenna loaded with two Galinstan bridges as shown in Fig. 3.18. (a) for different bridge lengths when D= 30 μm, and (b) for different PDMS spin coated heights [D as shown in Fig. 3.18(b)] when L_{br} = 8 mm. The curves are obtained from ADS circuit simulations of the TL model shown in Fig. 3.19(c) (l_1= 19.2, 18.7, 18.2, 17.7, 17.2, and 16.7 mm).

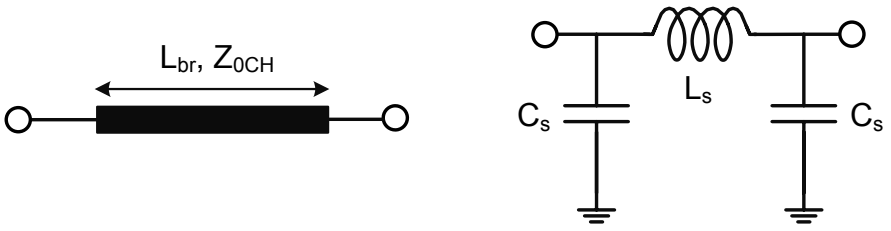

Fig. 3.21: Schematic and equivalent-circuit model of the Galinstan bridge TL.

not affect the parallel capacitor (C_s) values[6] [96]. The values of the inductor and both capacitors then can be found using

$$L_s = \frac{\mathrm{Z_{0ch}} sin\theta}{\omega} \qquad \text{(H)} \tag{3.2}$$

and

$$C_s = \frac{1 - cos\theta}{\omega \mathrm{Z_{0ch}} sin\theta} \qquad \text{(F)} \tag{3.3}$$

where $\mathrm{Z_{0ch}}$ is the characteristic impedance of the Galinstan bridge TL, θ is the electrical length of the Galinstan TL, and ω is the angular frequency. Equations (3.2) and (3.3) show that while by decreasing $\mathrm{Z_{0ch}}$, the series inductor value decreases, the capacitors values increases. This analysis suggests that Galinstan bridges can be used instead of lumped capacitors to achieve miniaturization and tuning for CPW folded slot antennas since they are compatible with the geometry of CPW folded slot antenna.

To obtain better approximations for the resonance frequency of the Galinstan loaded antenna and also to verify the results achieved from ADS circuit simulations,

[6]These small series capacitors introduce a resonance for the bridge at a much higher frequency than the antenna operating frequency as the full-wave simulations show. Accordingly, for studying the capacitive loading effects of the Galinstan bridge only the shunt capacitors are important. In fact, the model is only used to determine the effect of bridge dimension changes on the value of C_s. Hence, the gap under the bridge can be neglected.

full-wave simulations of the structure in HFSS (for different values of L_{br}, W_{br}, and D) are also performed. Fig. 3.22 shows the frequencies of the first resonance of a CPW folded slot antenna (Fig. 3.18) with dimensions tabulated in Table 3.3. Fig. 3.22(a) shows the variations in resonance frequency of the antenna with respect to the changes in the length of the Galinstan bridge (L_{br}) and its distance from the edge of slot antenna (l_2). As can be seen, the full-wave simulation results agree with the ones obtained from circuit simulations using the TL model [see Fig. 3.20(a)]. Fig. 3.22(b) examines the dependence of the resonance frequency to the variations in the spin coated layer thickness (D), and the width of the Galinstan bridge (W_{br})[7]. Both increasing W_{br} and decreasing D result in a smaller Z_{0ch} for the Galinstan bridge TL. Accordingly, a lower resonance frequency is expected due to higher capacitive loading of the Galinstan bridge.

3.2.2.3 Galinstan-loaded Miniature Antenna

The information in the previous subsection is used toward designing a miniature antenna based on a pair of Galinstan bridges. As shown in Fig. 3.20 and 3.22, decreasing the distance between the Galinstan bridge and CPW feed line (l_1) results in an increased frequency down-shift. To achieve the maximum miniaturization factor l_1 should then be minimized (l_2 should be maximized). However, a larger miniaturization factor is not the only effect of decreasing l_1. Fig. 3.23 shows the surface current distribution on top of the CPW folded slot antenna, and the magnitude of E-field distribution (E_y is the dominant field component) in the plane of slot conductor edge [C-C' cut in Fig. 3.23(a)] for the cases of unloaded and Galinstan-loaded antennas, respectively. As can be seen, the maximum E-field distribution is around the center of the slot. Locating the Galinstan bridges on the CPW folded slot antenna causes

[7]Notice that l_2 is set to zero for this plot in order to better discern the effects of D and W_{br} on the resonance frequency of the antenna.

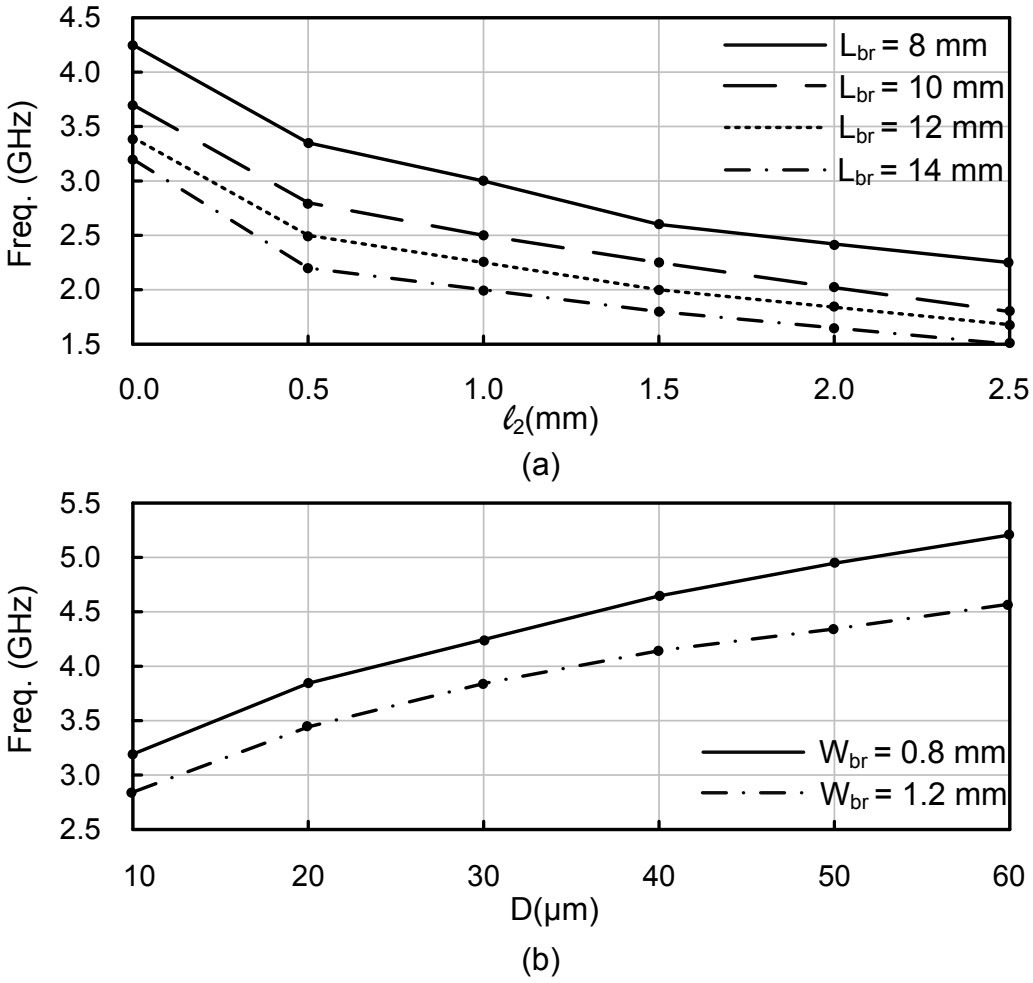

Fig. 3.22: First resonance frequency of a CPW folded slot antenna loaded with two Galinstan bridges as shown in Fig. 3.18. (a) For different bridge lengths when D= 30 μm, and (b) different PDMS spin coated heights [D as shown in Fig. 3.18(b)] and different bridge widths (W_{br}) when L_{br} = 8 mm, and l_2 = 0 mm. The curves are obtained using full-wave simulations in HFSS.

the surface currents to detour a longer distance to encompass the CPW folded slot antenna. This longer path for the surface currents results in a lower resonance frequency. However, placing them too close to the center of the antenna will manipulate the E-field distribution in the region which is mainly responsible for radiation. This translates into low radiation gain and in the case of locating the Galinstan bridge pair at the center of the antenna results in very poor radiation. Therefore, there is a trade-off between the miniaturization factor and gain of the antenna while decreasing l_1. Fig. 3.24 shows both simulated realized gain and miniaturization factor of the antenna relative to the changes in l_2[8]. By increasing l_2 (decreasing l_1) by 4 mm miniaturization factor increases by 6%. However, gain of the antenna drops down to -4 dBi.

While the limitation in excessively decreasing l_1 is gain degradation, increasing $\mathrm{L_{br}}$ more than a certain value will cause a non-ideal RF short to occur. Since the Galinstan bridge is an open-ended transmission line as discussed in section II-*B*, making $\mathrm{L_{br}}$ close to $\lambda_g/2$ at the frequency of resonance causes the slot antenna to see two open-ended $\lambda_g/4$ stubs. This translates into a fictitious RF short seen by the slot antenna. While this might be useful in the case of switching the operating frequency to a higher state[9], it doesn't result in miniaturization since the operating frequency increases by switching.

In order to better understand the effect of $\mathrm{L_{br}}$ on the antenna resonance frequency, Fig. 3.25 shows the simulated $\mathrm{S_{11}}$ results for three different lengths of the loading Galinstan bridges. For $\mathrm{L_{br}}$ =0 mm, the first resonance frequency is located at $f_{0,0} \approx 5.8$ GHz, which is the one for a non-loaded CPW folded slot antenna with the

[8]Note that $l_1 + l_2 + \mathrm{W_{br}} = \dfrac{\mathrm{L_s}}{2}$.

[9]As shown in [91], in the case of using the $\lambda_g/2$ liquid metal bridge as an RF-shortening switch, this method is not an effective one due to the lower mode caused by parasitics.

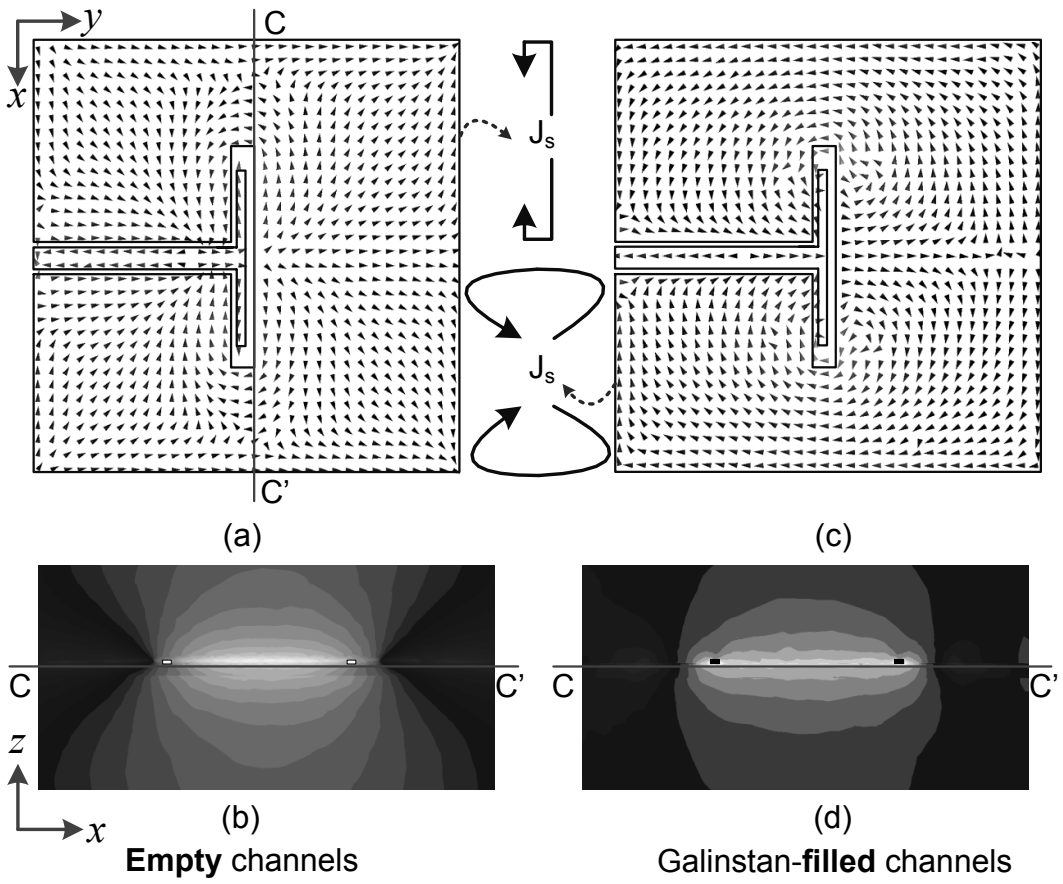

Fig. 3.23: Simulated vector surface current distribution on the CPW folded slot antenna and the magnitude of electric field distribution in the plane of slot conductor edge (C-C') for (a), (b) Empty, and (c), (d) Galinstan-filled channels. The Galinstan bridges are not shown in (c) for better visibility.

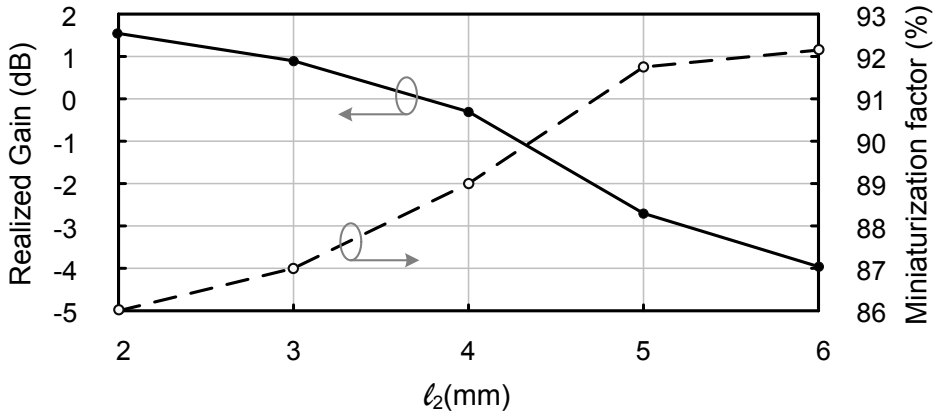

Fig. 3.24: Miniaturization factor and realized gain variations with respect to changes in l_2 (L_{br} = 12 mm).

parameters in Table 3.3. The second resonance of the antenna is located at $f_{1,0} \approx 18$ GHz, which shows a wide out-of-band rejection range for CPW folded slot antennas. For the case of $L_{br} \approx \lambda_g/4$, as discussed above, the antenna has a first resonance frequency of $f_{0,\lambda_g/4} \approx 1.8$ GHz, and the second well-matched resonance frequency is located at $f_{1,\lambda_g/4} \approx 17.5$ GHz. This shows that using the Galinstan bridge loading method for miniaturization, further improves the natural wide range out-of-band rejection characteristics of the CPW folded slot antennas. For the case where the length of the Galinstan bridge is increased to $\sim \lambda_g/2$, however, the two modes of the antenna are very close to each other. Since in the real implementation l_2 =1.7 mm, the CPW folded slot antenna in this cases is shortened at both ends and the effective length of the antenna is ∼3.4 mm shorter. Although, for the case of ideal RF shorts the only excited frequency would be the one located at $f_{1,\lambda_g/2} \approx 7$ GHz, Galinstan non-ideal short excites another mode at $f_{0,\lambda_g/2} \approx 6$ GHz. This behavior becomes more critical when a wider switching range is needed (i.e. larger l_2 which results in a shorter effective length). In such scenario, $f_{0,\lambda_g/2}$ and $f_{1,\lambda_g/2}$ will become isolated, causing the antenna to become a dual-band one with a lower out-of-band rejection

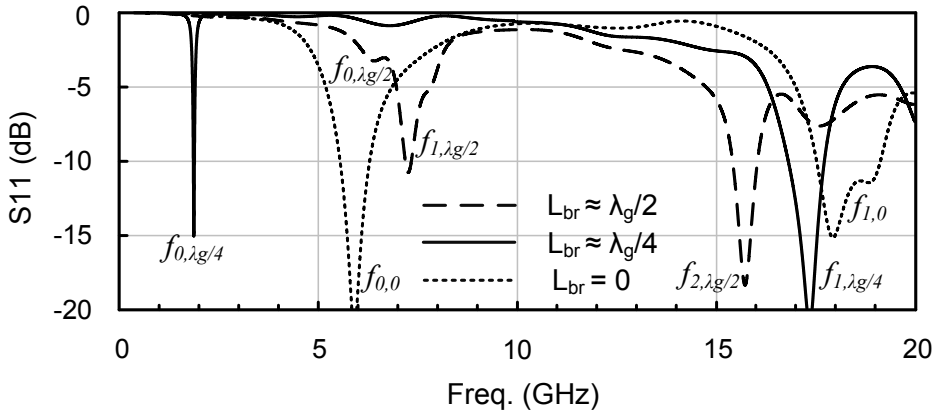

Fig. 3.25: Effect of changing L_{br} on the first resonance and out-of-band rejection (selectivity) of the antenna (l_2=1.7 mm).

range since another resonance frequency also appears at $f_{2,\lambda_g/2} \approx 16$ GHz (see Fig. 3.25).

Based on the above discussion, $l_1 = 7.5$ mm and $L_{br} = 12$ mm are chosen to provide an operating frequency located at 1.8 GHz and gain of 1.7 dBi (∼-0.45 dBd). Fabrication procedure for the miniature antenna will be thoroughly explained later. Fig. 3.26 shows the fabricated prototype of the miniature antenna. The Galinstan bridges are realized using two PDMS structures and the channels are sealed completely so that the antenna can be used as a fixed miniaturized CPW folded slot antenna.

The input reflection coefficient of the fabricated miniature antenna is measured using an Agilent N5230A calibrated vector network analyzer (VNA). The simulated and measured S_{11} results of the antenna are shown in Fig. 3.27. The antenna shows matching of better than -18 dB for its resonance frequency of 1.9 GHz. There is a 4% error in the resonance frequency of the antenna in comparison with the simulation results. This error can possibly occur due to fabrication errors and inaccuracies such as the tolerance in the exact dielectric constant value, thicknesses of both the

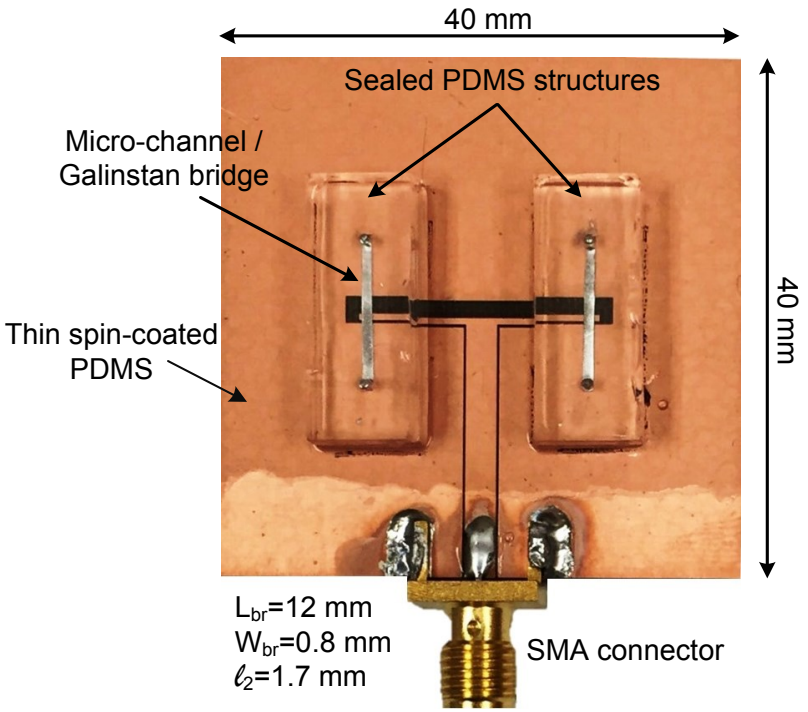

Fig. 3.26: Fabricated miniaturized CPW folded slot antenna.

substrate and the PDMS structures, thickness of the spin coated PDMS layer, and micro-channels' width. The accuracy in fabrication is limited to the accuracy of the 3D printer and the alignment method. As a result, either by increasing the fabrication accuracy or by making the design more robust to these tolerances, such errors can be avoided. For the case of the proposed prototype, the authors have employed parametric simulations with fine adjustments of different material properties such as dielectric constant and layers' thicknesses and found the main reason of this frequency shift to be the thickness of the spin-coated layer.

The radiation characteristics of the miniature antenna are measured in a standard anechoic chamber at the operating frequency. The measured normalized co- and cross- polarized radiation patterns of the antenna in two principal cut planes are shown in Fig. 3.28 for the operating frequency. The measured maximum gain of

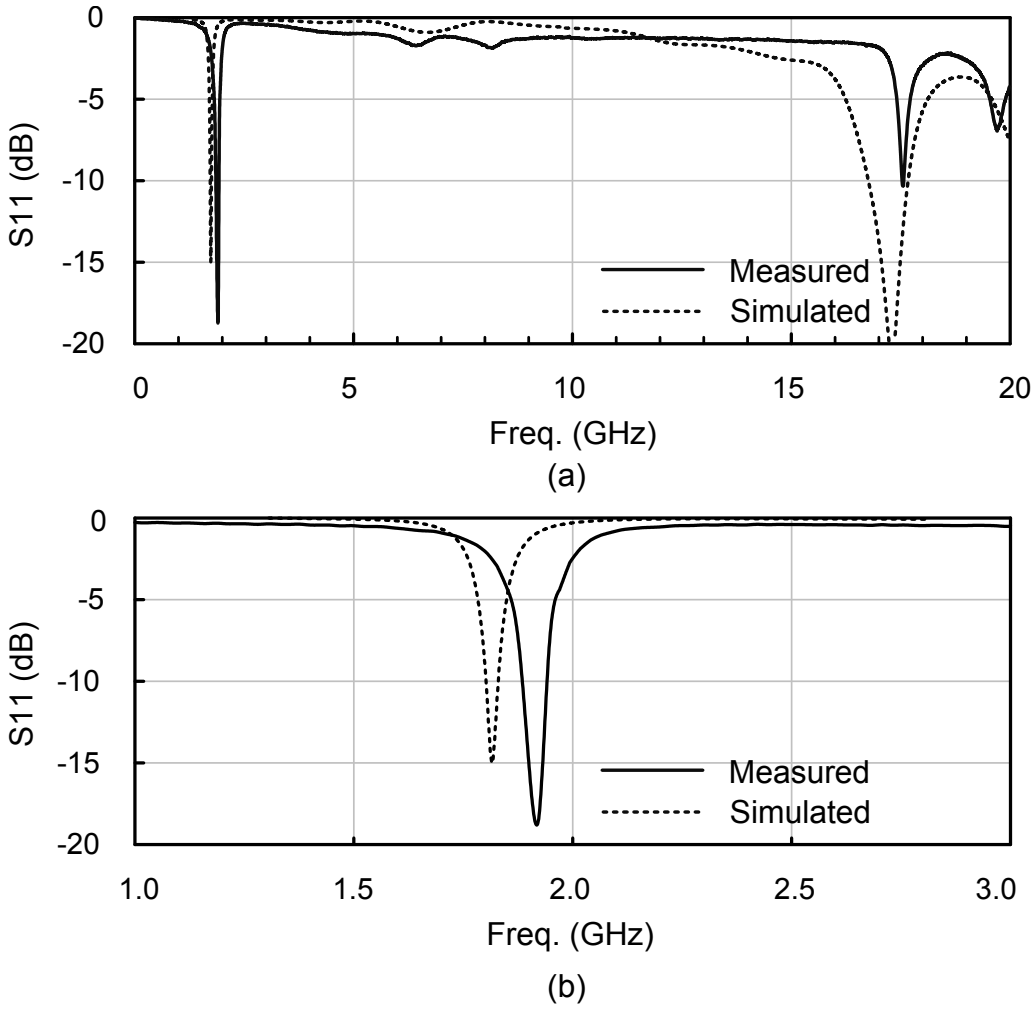

Fig. 3.27: Measured and simulated S_{11} results of the prototype antenna for the frequency range of (a) 0-20 GHz, and (b) 1-3 GHz.

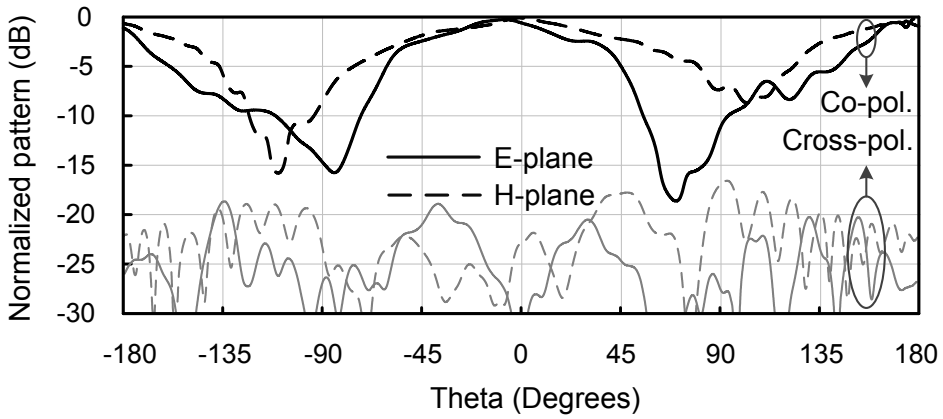

Fig. 3.28: Measured normalized radiation pattern of the miniature CPW folded slot antenna at 1.9 GHz.

the antenna at its resonance frequency is 1.2 dBi (-0.95 dBd). Pattern purity (i.e. the difference between the co- and cross- polarized level) of better than 17 dB is observed.

3.2.3 Miniature Reconfigurable Antenna

A reconfigurable version of the antenna is obtained by replacing the fixed pair of Galinstan bridges in the miniature antenna with two pairs of micro-channels that can be filled or emptied. As shown in the previous section, this technique enables a very low operating frequency with the next mode appearing at least 15 GHz higher. This suggests that very wide switching range can be achieved using a reconfigurable micro-channel structure. The antenna is based on a 1.53 mm thick Taconic TLY substrate (ϵ_r = 2.2, tanδ = 0.0009), and the same layout shown in section II for the miniature version. Fig. 3.29 shows the channel configuration of the switchable antenna version with two pairs of micro-channels. Based on the design procedure explained in section II (Fig. 3.20, and 3.22), the dimensions L_{br}, W_{br}, S_{br}, and l_2 (Fig. 3.29) are chosen to provide three resonance frequencies at 2.4 GHz, 3.5 GHz,

and 5.8 GHz[10]. These three frequencies refer to the states in which the outer pair of channels is filled with Galinstan (State 3), the inner pair of channels is filled with Galinstan (State 2), and all channels are empty (State 1), respectively. The state in which all channels are filled with Galinstan is excluded from the functional states since the frequency obtained by this state is very close to the frequency obtained in State 3[11]. The reason for choosing these three frequencies in particular is to demonstrate the ability of the antenna and the tuning method to obtain any band of interest within the range of 1.8-5.8 GHz. As discussed before, the resonance frequency of the antenna depends on the physical dimensions of the CPW folded slot, and physical dimension and location of Galinstan bridges. Therefore, the proposed operating frequencies can easily be scaled to any other band of interest. In fact, since the proposed miniaturization/switching method does not have the biasing circuit limitations such as the ones for MEMS switches or semiconductor components [60], it can be easily applied to higher frequencies as well using a more precise fabrication and alignment method.

Fabrication procedure for the CPW reconfigurable antenna will be thoroughly explained in the next section. Fig. 3.30 shows the fabricated prototype of the reconfigurable antenna along with the magnification of the micro-channels' configuration for different states. The Galinstan bridges are realized using two separate PDMS structures. For the reconfigurable version after sealing the Galinstan bridges, Inlet and outlet tubings are inserted in order to configure the micro-channels for different states. By filling or emptying these micro-channels, three different states can

[10]To do so, the parameter S_{br} is used to control the lowest frequency of the antenna AKA state 3. Notice that $S_{br}+W_{br}+l_2=l_2'$ and that fabrication constrains are also taken into account in choosing S_{br}. Accordingly, l_2, and l_2' are chosen using the information in Fig. 3.20, and 3.22.

[11]Notice that if a higher tuning resolution (i.e. more state numbers) is needed the number of channels can be increased. However, shorter channels must be used so that the loading obtained by each channel will be small. In such case the maximum loading effect is achieved by filling all the channels with Galinstan and not using a single Galinstan-filled pair.

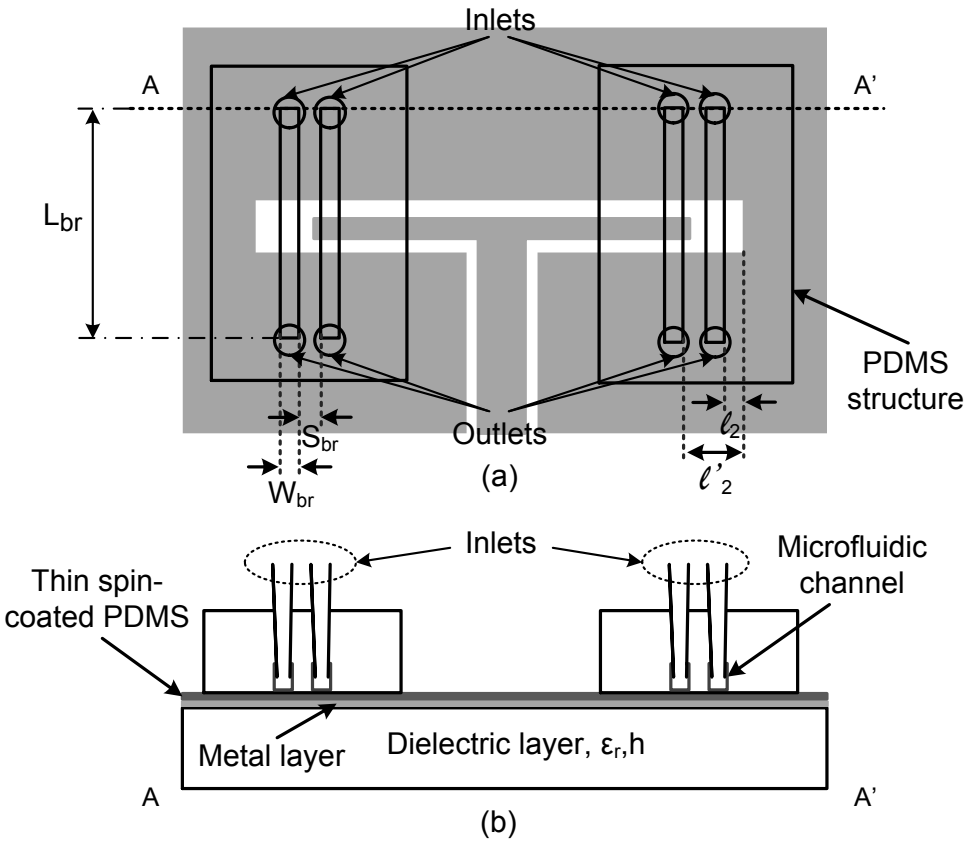

Fig. 3.29: Topology of the micro-channels' configuration for the reconfigurable antenna version. (a) Top view. (b) A-A' cross section.

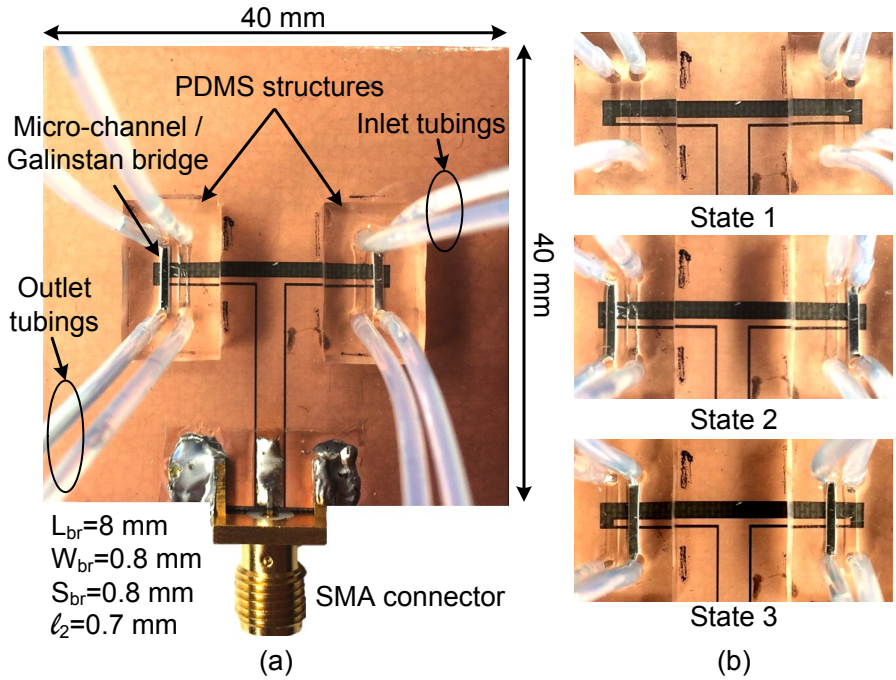

Fig. 3.30: (a) Fabricated reconfigurable CPW folded slot antenna. (b) Magnification of micro-channels' configuration for different states.

be achieved.

The tubes are first filled all the way with Teflon. Once the tubes and the micro-channel are filled up with Teflon, Galinstan is injected into the tube and micro-channel. The correct amount of Galinstan is calculated using the volume of the micro-channels based on the dimensions of each micro-channel. Then a micro-liter scaled syringe is used for Galinstan injection. This Galinstan chunk is pushed using Teflon solution until it is placed completely inside the micro-channel and on top of the folded slot antenna. Since Galinstan is injected into the micro-channels manually and through the inlet tubings, this question may arise that what happens if more liquid metal than the exact volume needed is injected into the tubings. One result might be further loading of the CPW slot antenna. However, the orientation in which the tubings are inserted into the micro-channels won't let excess Galinstan to be close

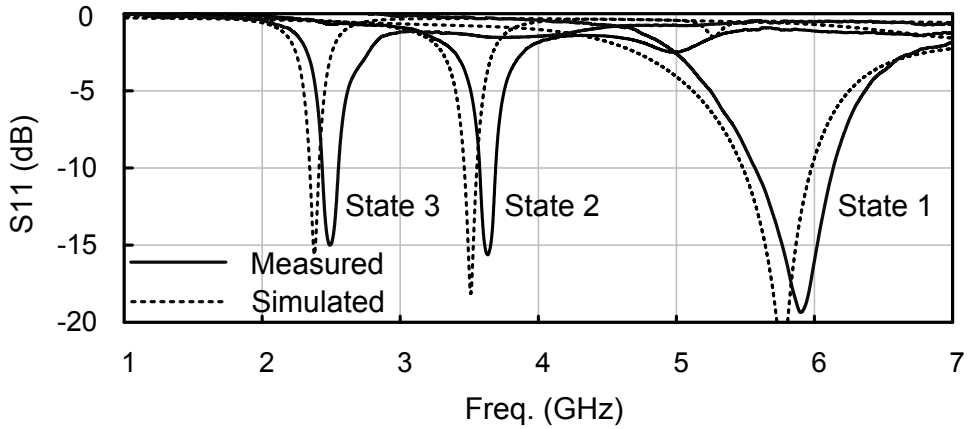

Fig. 3.31: Measured and simulated S_{11} results of the prototype reconfigurable CPW folded slot antenna.

enough to the antenna. Since the height of the micro-channels is ∼400 μm, excess Galinstan will be placed at least ∼400 μm away from the CPW folded slot antenna. As shown in Fig. 3.22, for D more than 50 μm, the frequency shift is negligible. Hence, the frequency of operation won't be affected by the excess Galinstan. One other issue that may occur is radiation perturbation. It is important for the excess Galinstan not to form a liquid wire with a length longer than $\lambda/10$ at the frequency of operation, as this may lead to radiation perturbation. Since at the lowest operating frequency this length is ∼12 mm, the accuracy of manual injection is sufficient to avoid this issue.

The input reflection coefficient of the fabricated antenna for all the three states is measured using an Agilent N5230A calibrated vector network analyzer (VNA). Fig. 3.31 shows the simulated and measured S_{11} of the proposed reconfigurable antenna (shown in Fig. 3.30).

The radiation characteristics of the reconfigurable version antenna are measured in a standard anechoic chamber for the highest and lowest frequencies as the most extreme cases. The measured normalized co- and cross- polarized radiation patterns

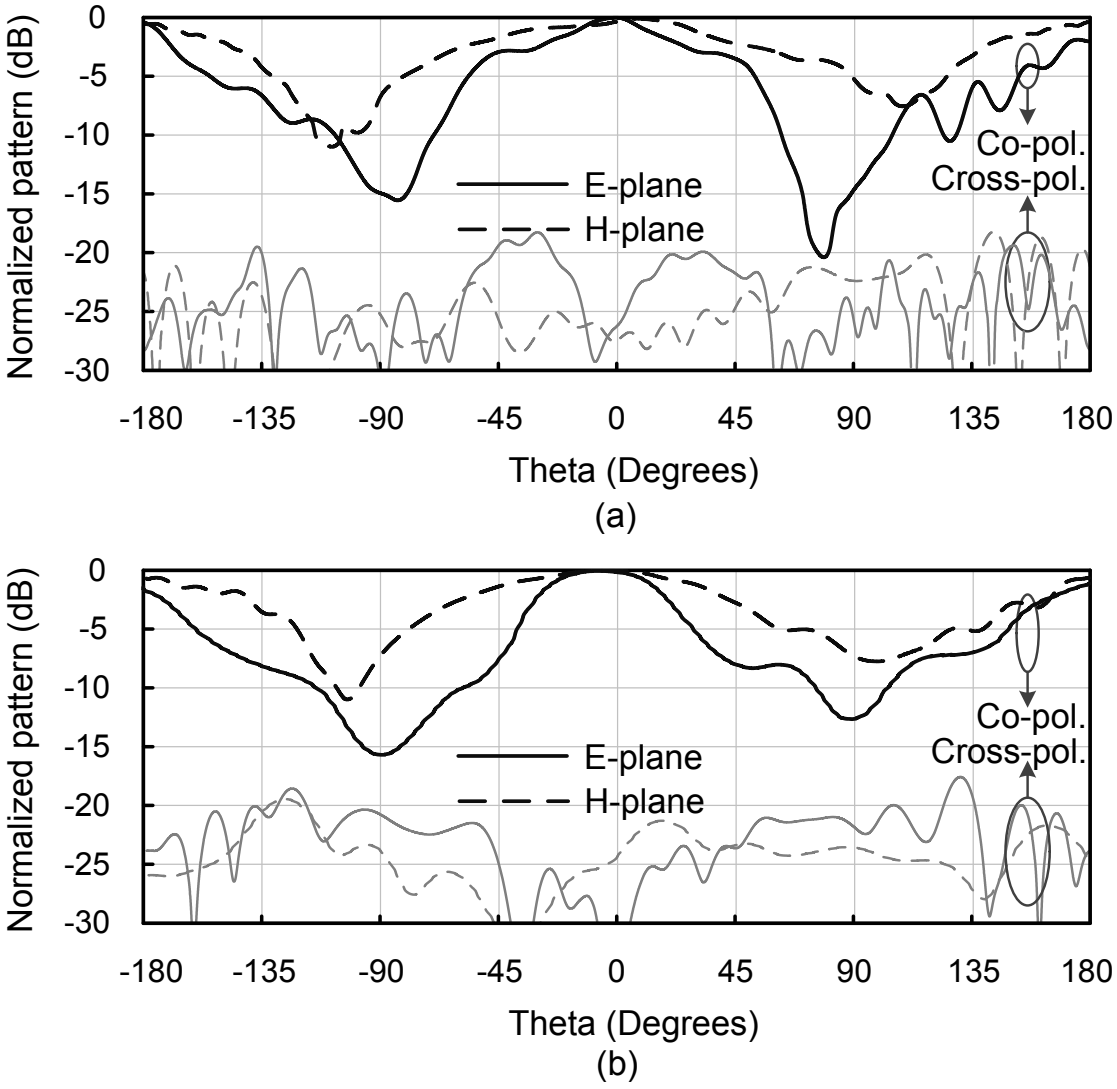

Fig. 3.32: Measured normalized radiation pattern of the reconfigurable CPW folded slot antenna at (a) State 3–2.4 GHz, (b) State 1–5.8 GHz.

of the antenna in two principal cut planes are shown in Fig. 3.32(a), and (b) for states 3 and 1, respectively. As can be seen, antenna shows a similar both sided radiation pattern at both states. The measured maximum gain of the antenna at the states 1, and 3 is 3.55, and 2.4 dBi, respectively. The reason for the gain drop is the miniaturization achieved at state 3. Pattern purity (i.e. the difference between the co- and cross- polarized level) of better than 20 dB is observed.

3.2.4 Fabrication Procedure

Fabrication of antennas is done using standard soft lithography techniques and 3D printer. Following steps are used to realize the designed antennas, as shown in Fig. 3.33.

3.2.4.1 The Miniature Antenna

The circuit boards for this design are fabricated using PCB technology [see Fig. 3.33(a)-Step 1]. Two 3D templates are designed in Solidworks and printed layer by layer using a 3D micro printer (Step 2). Two separate molds are used for this design to obtain a complete PDMS structure. One mold is used to make the lower half of the PDMS substrate with channels, and the other mold is used to fabricate the upper half of the PDMS substrate which is flat and provides a seal for the inlets and outlets. Each mold is cleaned using isopropyl alcohol (IPA) and left in oven at 65°C for at least 24 hours to remove any chemicals. Before using the 3D printed mold for the first time, it is coated with very small amount of T2492, (tridecafluoro-1,1,2,2-tetrahydrooctyl)-1-trichlorosilane, from UCT Inc. [97]. This coating prevents PDMS from sticking to the mold and allows cured PDMS to be peeled easily from the surface. PDMS solution is prepared by mixing Sylgard 184 (from Dow Corning) resin and curing agent in 10:1 ratio. PDMS solution is then poured over the micro-mold and de-gassed to remove air bubbles in PDMS solution using a vacuum desiccator. PDMS is cured in the oven at 65°C for two hours and peeled from the mold (Steps 3, 4).

Then the lower PDMS structure contains channels, and the inlets/outlets are made by punching holes through the PDMS. The upper PDMS structure is a flat piece and is used as it is. A 30 μm thin layer of PDMS is spin-coated directly on the PCB circuit board and cured on hot plate at 65°C for 2 hours (Step 5). The lower PDMS structure obtained by molding and the thin PDMS layer on PCB board are permanently bonded after oxygen plasma treatment. Manual alignment marks are made on the circuit board to properly align the lower PDMS structure and channels over the substrate (Step 6). Galinstan is directly injected into the channels using a manual syringe (Step 7). The upper PDMS structure is bonded to the lower PDMS structure containing Galinstan by applying a small amount of PDMS solution between both the layers. The whole structure is placed in oven for 2 hours to cure all PDMS and form a single PDMS structure (Step 8). Finally, the PCB circuit board is connected to an SMA connector for measurements. To do so, a small part of the spin-coated PDMS layer is peeled off using cutter and rubber gloves. Also, removable tape can be used on the board at the input port location to shape the spin-coated layer in a way that soldering the SMA connector later won't be an issue. Laser cut may be used in case more accurate cut-outs are needed.

3.2.4.2 The Miniature Reconfigurable Antenna

The circuit boards for this design are also fabricated using common PCB technology (Step 1). The 3D templates are printed using the same 3D micro printer (Step 2). The cleaning and molding procedures are same as mentioned before (Steps 3, 4). As a result, PDMS structure contains the channels, while the inlets/outlets are made by punching holes through the PDMS. A 30 μm thin layer of PDMS is spin-coated directly on the PCB circuit board and cured on hot plate at 65°C for 2 hours (Step 5). The PDMS structure by molding and the thin PDMS layer on PCB board are perma-

nently bonded after oxygen plasma treatment (Step 6). Manual alignment marks are made on the circuit board to properly align PDMS structure and channels over the substrate. Channel inlets/outlets are connected to flexible tubing to inject/remove Teflon solution and Galinstan (Step 7). The circuit board is then connected to an SMA connector after peeling off a small part of the spin-coated PDMS.

3.2.5 Discussion

There are some practical concerns regarding antenna tuning using liquid metals as an emerging technique. In this subsection, some of these concerns are qualitatively addressed based on the author's observations and measurement experience.

3.2.5.1 Durability

There may be questions regarding the durability of the liquid metal used, especially in the case of the miniature version where the Galinstan bridge may have to stay inside the channel for a longer period of time. To realize whether the miniature antenna employing the Galinstan bridges is durable enough or not, the antenna prototype is measured over time. For this purpose, the proposed antennas were left on the measurement bench at room temperature for a 21 days period. After this time lapse, the antenna measured S-parameter results did not differ in any significant manner from the initial results shown in the previous section. This statement is also true for the case of the reconfigurable antenna. However, in this case, durability of Galinstan inside the channel should not be a problem since the micro-channel can always be refilled with fresh Galinstan.

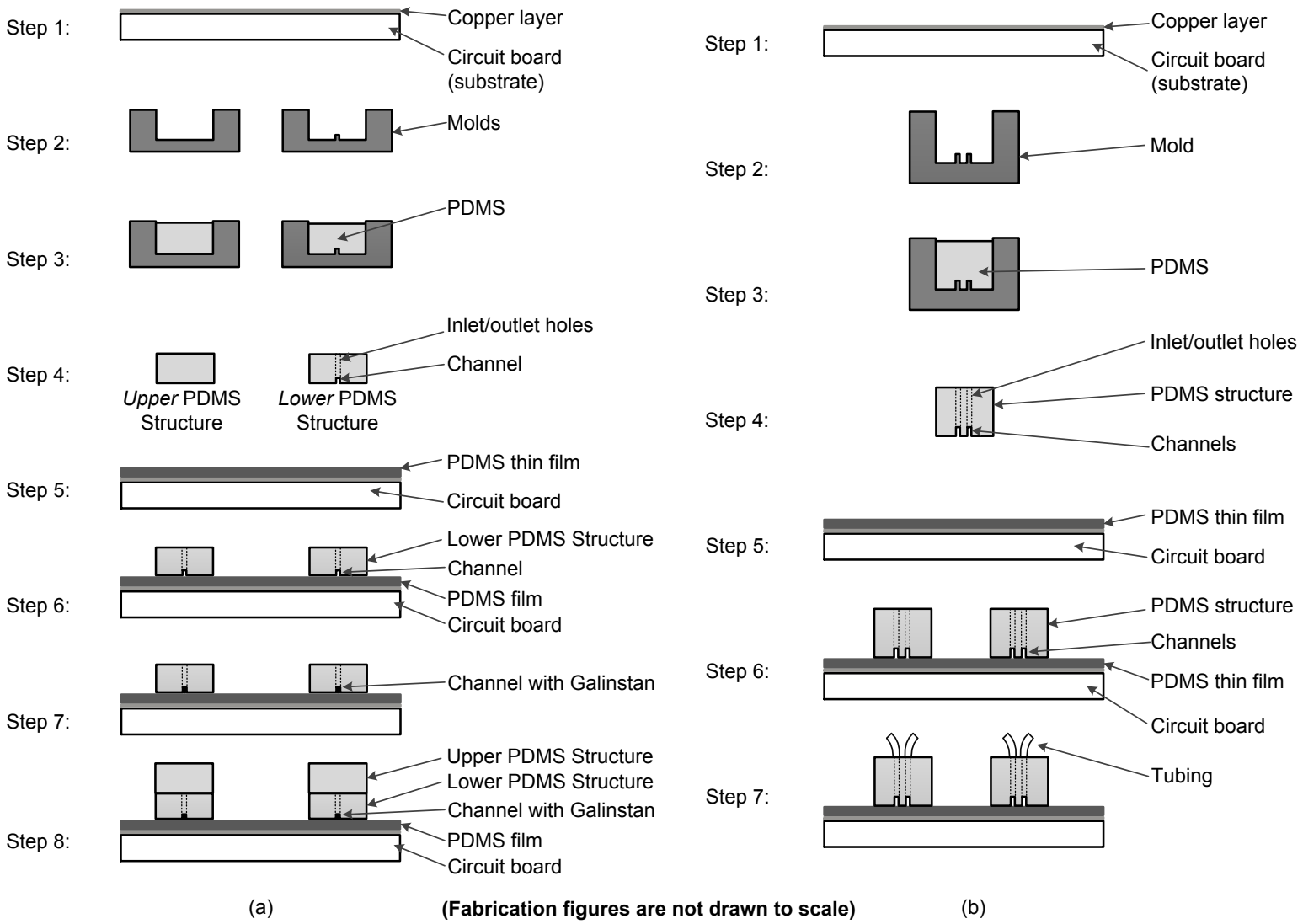

Fig. 3.33: Step-by-step process showing side view for fabrication of the (a) Galinstan-loaded miniature antenna, and (b) Miniature reconfigurable antenna.

3.2.5.2 Repeatability

In terms of reconfiguration repeatability for the miniature reconfigurable version, two micro-channels that are filled with Galinstan in State 3 [see Fig. 3.33(b)] were evacuated by a rinse of Teflon solution and refilled with Galinstan for 10 times. Each time both measured results of the State 1, and 3 were compared with the original ones shown in the previous section. Since no residues were left in the channels after evacuation for the repeated measurements, the results did not show any difference from the ones presented for the originally empty channels case presented in the previous section.

3.2.5.3 Switching Speed

Generally, one of the most important issues about liquid-based tuning methods is the switching speed. While semiconductor-based switches can perform at speeds in the order of $\sim 1\mu$s, the liquid-based methods have a much lower speed. A detailed comparison of an antenna switched by both systems is done in [79], which shows that even by using micro-pumps, these systems show a significantly lower speed. However, these two switching methods are also compared in terms of efficiency, radiation pattern, and electrical size and it is mentioned that the liquid-based method has bold advantages which can be useful in the applications where switching speed is not of concern. This issue also motivates further research on electrically controllable liquid-based switchable/tunable antennas. Such a system should be capable of moving the liquids inside the channels continuously and based on a single voltage applied.

3.2.5.4 Power Handling

Finally, one of the most important advantages of liquid-based techniques is the significant improvement achieved in power-handling using these devices in compari-

son with the ones realized based on RF-MEMS or semiconductor components. Recently, authors realized a miniature reconfigurable filter [please refer to *section 3.1*], which can be used for input RF powers of up to ∼20 W for short-duration excitation conditions and 10 W for high-average-power excitation conditions with no significant difference in performance of the filter. Due to the nature of antennas and the fact that performing such high-power characterization of antennas require a controlled environment [76], the authors defer performing such characterization for the implemented antennas to a future publication.

3.2.6 Conclusion

Liquid metal Galinstan is used to develop microfluidic-based fixed and switchable capacitors. Since these capacitors are completely compatible with the geometry of CPW folded slot antennas, they are used toward introducing both miniature (85% reduction of the antenna area) and miniature reconfigurable (2.4-5.8 GHz) CPW folded slot antennas. Due to the switching abilities of the Galinstan bridge at higher order modes, while loading capacitively at the lower frequencies, the antenna shows a significant (larger than ∼15.5 GHz) out-of-band rejection. This feature is used toward designing a reconfigurable antenna with a very wide switching range (2.5:1). Design methodology, TL circuit model of the antenna, fabrication process, and experimental results are presented and discussed in detail. All states show similar radiation pattern shapes and a pattern purity better than 17 dB for all bands of operation is also observed. To the best of author's knowledge, this is the first presentation of a microfluidically-loaded miniaturized antenna and the most compact CPW folded slot antenna with a very wide switching range.

3.3 A Microfluidically-reconfigurable Dual-Band Slot Antenna With a Frequency Coverage Ratio of 3:1

3.3.1 Introduction

Fluidics have been used recently in different ways to tune antennas as an alternative to conventional methods [34, 88, 90, 91, 95]. Using fluidics-based tuning methods comes with three major advantages. First, since the method is based on highly linear elements, it is expected to be capable of handling high-power RF inputs [76]. Second, employing soft materials using common technologies can result in flexible and wearable electronics [64]. Third, liquid metal elements are capable of retaining their physical changes after removing the actuation force, whether it is a pressure driven force or an electrically actuated one. This is not the case for semiconductor and MEMS devices, where often a continuous actuation voltage is needed to maintain the non-baseline performance states [34]. The existing work in the area of liquid-based tunable antennas includes changing the length of the antenna in [88, 90], using the liquid metal channel as a non-ideal RF shortening switch [91], and using dielectric liquid materials as a superstrate which loads the antenna [95]. Another method is based on using the liquid metal as a reactive load on top of the slot antenna. The method was first introduced in [98] to tune both bands of a dual band slot antenna using four different micro-channels. The entire frequency range between the two bands, however, is not covered by the antenna in [98].

This section describes a method to obtain independent reconfiguration of both frequencies of a dual-band slot antenna in a way that the entire frequency range of 1.8-5.4 GHz is covered by the antenna. Five liquid metal bridges on top of two slot antennas are employed. By using different configurations of filled and empty channels different combinations of the two operating frequencies are achieved. The

tuning range of the second band is extended by employing an additional micro-channel for coarse tuning. The antenna achieves a discrete tuning ratio of 1.7:1 for both bands and an overall coverage range of 3:1. The antenna and micro-channels are fabricated using common PCB techniques and 3D molding, respectively. These two structures are bonded to each other using a thin spin-coated layer of PDMS. Due to the highly linear nature of the elements used to tune the antenna and the fact that the liquid metal plugs don't need continuous force to retain their position, the proposed antenna can be useful for the applications in which linearity, power handling, and power consumption are of concern. Also, the proposed tuning method can be applied to a more flexible PCB substrate to obtain flexible widely reconfigured antennas.

3.3.2 Microfluidically-reconfigurable Antenna

3.3.2.1 Antenna Topology

As illustrated in Fig. 3.34, the microfluidically reconfigurable antenna is designed based on a Rogers RT/duroid 5880 substrate (ϵ_r = 2.2, $tan\delta$ = 0.0009) with a thickness of 0.8 mm. Five micro-channels are placed on top of the dual-band slot antenna using two separated PDMS (ϵ_r = 2.68, $tan\delta$ = 0.004) structures. While the first slot is reconfigured using two micro-channels, the second one is tuned by the aid of three channels. The reason for this difference is that a broader absolute bandwidth needs to be covered using the second slot antenna. The liquid metal used is a non-toxic alloy of Gallium, Indium, and Tin, also known as Galinstan (σ=2.30$\times$10^6 S/m) [34]. In order to avoid Galinstan from sticking to channel walls, a Teflon solution is used as a barrier between the Galinstan surface and the PDMS walls (Teflon AF 400S2-100-1, 1% Teflon powdered resin dissolved in 3M FC-40 from DuPont). The PDMS substrates are bonded to the slot antennas PCB board using

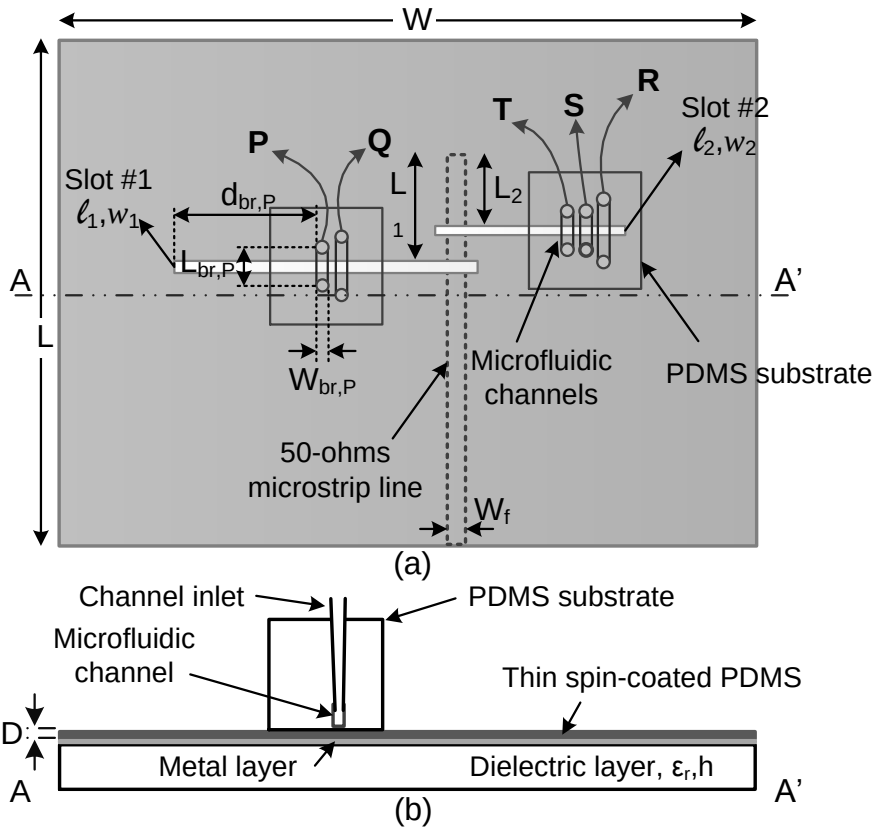

Fig. 3.34: (a) Top view (not to scale) of the microfluidically-reconfigurable dual-band slot antenna. (b) A-A' cross section view of the antenna.

Table 3.4: Dimensions (mm) of the Dual-band Slot Antenna†.

L	80	W	90	l_1	39.1	l_2	23
$w_1 = w_2$	1.5	h	0.8	L_1	13.7	L_2	9
$L_{br,P}$	4	$L_{br,Q}$	6	$L_{br,R}$	4	$L_{br,S}$	4
$L_{br,T}$	6	$W_{br,j}$	0.8	W_f	4	$d_{br,P}$	19
$d_{br,Q}$	21	$d_{br,R}$	0.5	$d_{br,S}$	2	$d_{br,T}$	4

†$L_{br,j}$, $W_{br,j}$, and $d_{br,j}$ refer to the length, width, and offset distance of each micro-channel, respectively. $j = P, Q, R, S, T$ as shown in Fig. 3.34(a).

a thin [D=60μm as shown in Fig. 3.34(b)] spin coated PDMS layer. The frequency shift for each slot antenna is controlled by four parameters. The length, width, and location of the micro-channels, and the height of the spin-coated layer as it controls the distance between the Galinstan bridges and the slot antennas. A microstrip line on the backside of the substrate is shared by both slots for excitation. A slot antenna is chosen for its superior tuning ability [36]. In order to match the slot antennas to the 50-ohms line, the theory of off-centered microstrip-fed slot antennas, and design methods for multi-band slot antennas are used [36]. To do so, each slot length $l_i (i = 1, 2)$ is initially set to be $\sim \lambda_{gs}/2$. The microstrip offsets (L_i) are both set at $\sim \lambda_g/4$. λ_{gs} and λ_g are the slot, and microstrip line guided wavelengths at the desired resonance frequencies, respectively, and are found using the methods in [73]. Once the parameters' values are estimated, 3D full-wave simulations must be used to achieve the exact resonance frequencies of interest. The slots opposite orientation is for having the lowest mutual coupling between the slots [36]. The non-loaded dual-band slot antenna is designed to have two bands of operation of 3.2, and 5.4 GHz, respectively[12]. Final dimensions of the proposed antenna are tabulated in Table 3.4.

[12]Note that the PDMS substrates are considered in the full-wave simulations for adjusting the baseline state's frequencies as they have a capacitive loading effect on the slot antennas.

3.3.2.2 Reactive Loading Using Galinstan Bridges

Each of these micro-channels when filled with Galinstan has a finite length. As a result, it can be modeled by a transmission line with a length of L_{br}, and width of W_{br} [91]. The PDMS spin-coated layer acts as the dielectric layer for the Galinstan transmission line. Due to the low dielectric constant of PDMS ($\epsilon_r = 2.68$), and the small height of this layer (D=60μm), the characteristic impedance of the TL is very small.

The bridges used for loading the antenna are much smaller than $\sim \lambda_g/2$. As a result, the slot antenna will see two very short portions of open-ended TL which translate into two capacitive loads. By controlling the length, width, and height of the PDMS spin-coated layer, this capacitive loading value varies. Increasing the Galinstan bridge length to be close to $\sim \lambda_g/2$ at the frequency of resonance, causes the slot antenna to see two open-ended $\sim \lambda_g/4$ TLs. This is equal to RF shortening the slot antenna, because it sees each open-ended $\sim \lambda_g/4$ TL portion as an RF short. However, since the liquid metal channel does not physically contact the ground plane, as shown in [91] another mode at a lower frequency also appears due to parasitics. Accordingly, employing the $\sim \lambda_g/2$ long Galinstan bridge is proven not to result in an ideal RF switch. Consequently, in this section the Galinstan bridges are used as switchable capacitors (i.e. shorter than $\lambda_g/2$ channels).

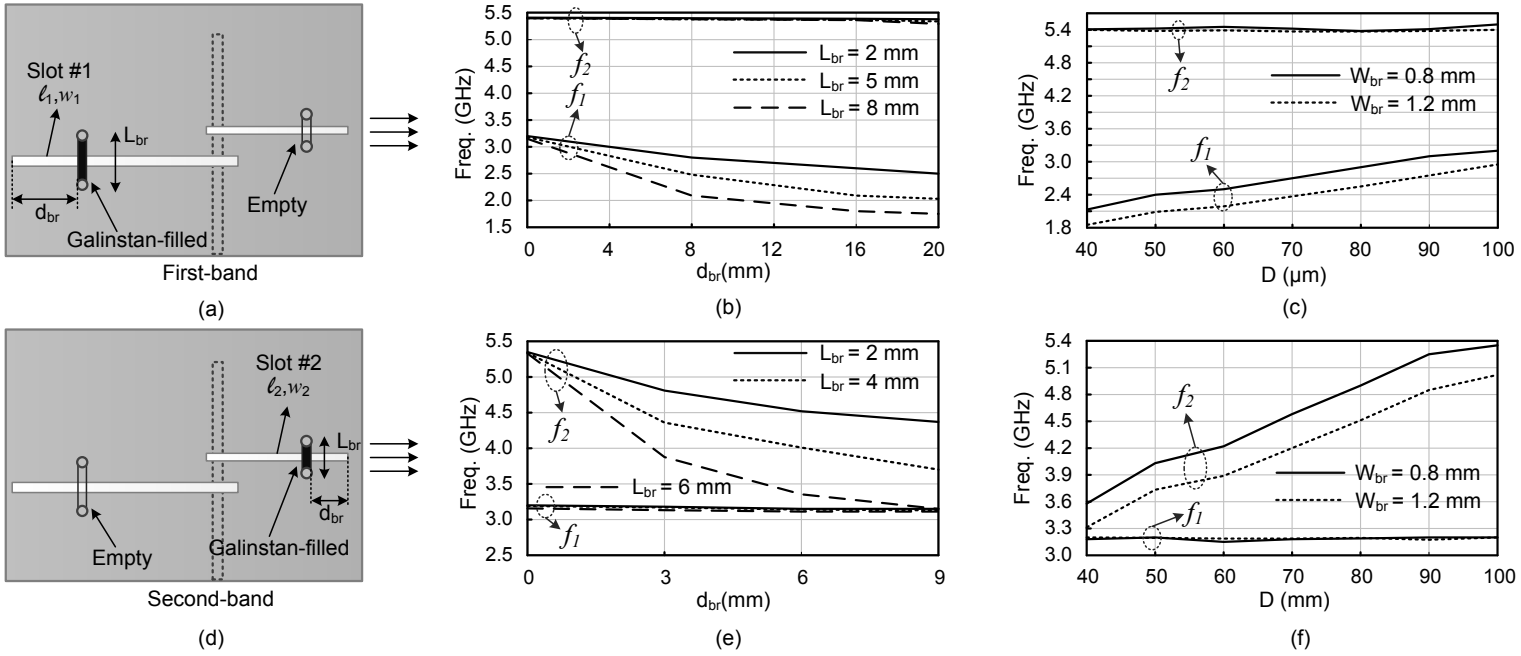

Fig. 3.35: First two resonance frequencies of a dual-band slot antenna when each slot antenna is loaded with a Galinstan bridge as shown in (a), and (d) for (b), and (e) different bridge lengths (L_{br}) and different channel locations (d_{br}) when D= 60 μm [D as shown in Fig. 3.34 (b)] and W_{br}=0.8 mm, and (c) , and (f) different PDMS spin coated heights and different bridge widths (W_{br}) when L_{br} = 4 mm, and d_{br}= 4 mm.

To better discern the effects of the Galinstan bridges on the slot antenna, full-wave simulations in HFSS can be employed. The critical parameters as discussed above (L_{br}, W_{br}, D, d_{br}) for a Galinstan bridge on top of each slot antenna are studied. As shown in Fig. 3.35 (a), the parameters for Slot #1 are first changed while the channel on top of Slot #2 is empty. The results are shown in Fig. 3.35 (b), and (c). The same has been done for Slot #2 [as shown in Fig. 3.35 (d)] while the channel on top of the Slot #1 is empty. The information shown in Fig. 3.35 are used toward designing the proposed dual-band antenna. As can be seen in Fig. 3.35 (b), and (e), increasing the channel's length, L_{br}, and increasing its distance from the slot edge, denoted by d_{br}, both result in decreasing the frequency of resonance for both slot antennas.

Fig. 3.35 (c), and (f) examines the dependence of each resonance frequency to the changes in the spin-coated layer thickness, D, and the width of the Galinstan bridge, W_{br}. As decreasing D, and increasing W_{br} will both decrease the characteristic impedance of the Galinstan bridge TL [73], they both result in a lower resonance frequency. The information in Fig. 3.35 is used toward designing the proposed reconfigurable dual-band slot antenna as discussed in the following section.

3.3.2.3 Micro-channels' Design

In order to achieve a reconfigurable dual-band slot antenna, 2 micro-channels (P, and Q) are employed on top of slot #1, and 3 micro-channels (R, S, and T) are located on top of slot #2. Using these Galinstan bridges, the initial resonance frequencies of the slot antennas (i.e. 3.2 GHz, and 5.4 GHz) are shifted down in different states. As a result, the entire frequency range of 1.8-3.1 GHz is covered by the first slot using four states and the frequency range 3.2-5.4 GHz is covered by the second slot antenna using eight states. The reason for different Galinstan bridges is

that more states need to be achieved by the second slot. This is because a constant frequency tuning resolution is normally of interest. As a result, a same tuning ratio for both slot antennas (1.7:1) is achieved with different number of states. Different locations of the Galinstan bridges (d_{br}) are because of the different frequency of operation of the two slots. A larger capacitance is needed to achieve the same tuning ratio for slot #1 than what is needed for slot #2. Based on the information in Fig. 3.35, this larger capacitance value can be achieved by either decreasing D for slot #1, or increasing the width, or length of the Galinstan bridges, or their distance from the slot edge. Among these options, the first one is not practical, since the spin-coated layer's thickness is constant for both slot antennas. Increasing the width, W_{br}, as the adjusting parameter is not a wise choice as it also affects d_{br} for the adjacent channel(s), which ultimately translates into change in the frequency tuning resolution. This is because of fabrication constrains in choosing the gap distance between two adjacent micro-channels. As the spacing between two micro-channels is a constant value, increasing W_{br} for each channel results in a compulsive increase of d_{br} for the adjacent channel. Also it is better not to increase the length of the bridge to avoid appearing the higher frequency modes of the slot antenna caused by the shortening effect of the $\lambda/2$ long channels. Accordingly, the last parameter (d_{br}) is chosen to adjust the required capacitance value for slots #1, and #2. The final dimensions of the micro-channels are tabulated in Table 3.4.

3.3.3 Fabrication and Experimental Results

A prototype of the proposed antenna is fabricated using common PCB technology, 3D printing, and soft-lithography techniques in 6 main steps [see Fig. 3.36 (a)]. The 3D mold needed is designed in SolidWorks and printed layer by layer using a Stereolithography 3D printer (Step 1). As this 3D mold is reusable, it makes it easy to

re-fabricate the PDMS substrate, and as a result, the tunable antenna. All chemical residues are cleaned off the fabricated mold employing isopropyl alcohol (IPA). Then the mold is left in heating oven at 65°C for at least 24 hours. PDMS solution is prepared by mixing Sylgard 184 (from Dow Corning) resin and curing agent in 10:1 ratio. PDMS solution is then poured over the micro-mold and de-gassed to remove air bubbles in PDMS solution using a vacuum desiccator. PDMS is cured in the oven at 65°C for two hours and peeled from the mold (Steps 2, 3). The holes used for inlet and outlet are punched carefully into the PDMS substrate (Step 3). Afterwards a 60 μm thick layer of PDMS is spin-coated and heat cured on the PCB board (Step 4). Oxygen plasma bonding technique is used to create a permanent bond between PDMS thin layer and the PDMS substrate (Step 5). Flexible tubings are inserted into the holes to serve as inlet and outlet of liquids (Step 6). Disposable syringes are used to inject Galinstan into the micro-channels and Teflon solution is used to evacuate Galinstan from the channels.

The input reflection coefficient of the fabricated reconfigurable antenna is measured using an Agilent N5230A calibrated vector network analyzer (VNA). The simulated[13] and measured S_{11} results of the antenna are shown in Fig. 3.37. There is a small frequency shift comparing the simulated and measured results, which can be justified by the tolerance in the exact dielectric constant of the PDMS, the exact thickness of the spin-coated PDMS layer, and the misalignment of the micro-channels in the bonding process. Independent reconfiguration of each band is demonstrated in Fig. 3.37 while the other band is constant. However, the number of performing states for the proposed antenna are not limited to the ones shown in this figure. The antenna is capable of operating at all 32 possible combination of these frequencies

[13]The simulation results are only shown for the tuned band in each graph for better visibility of the measured response.

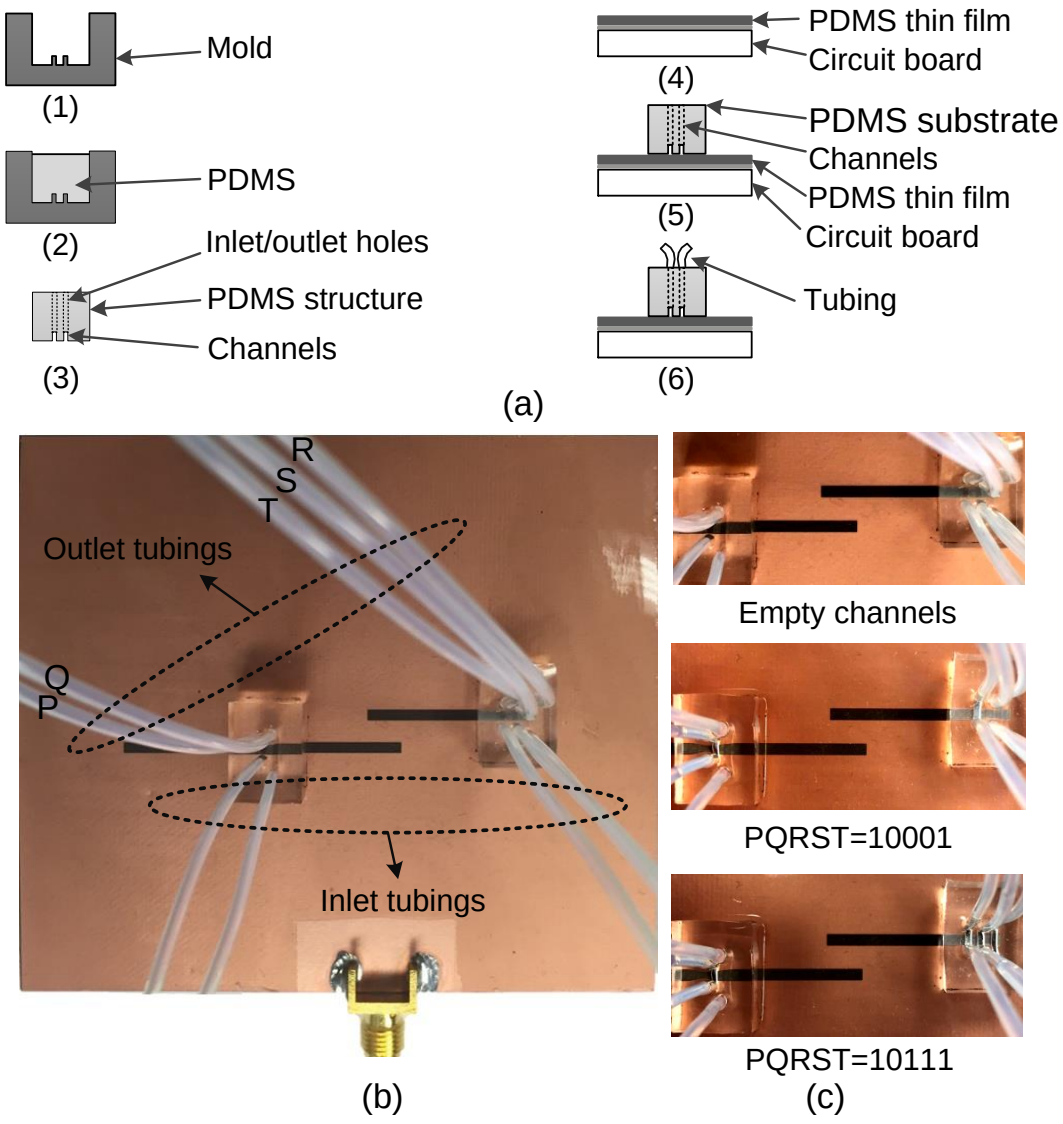

Fig. 3.36: (a) Step-by-step fabrication process, shown for slot #1. (b) Fabricated prototype of the antenna. (c) Magnification of three random states.

(4 states for the first band and 8 for the second one result in 32 possible states). As can be seen the proposed antenna is capable of covering the entire frequency range of 1.8-5.4 GHz using two operating bands (∼3:1). Return loss of more than 15 dB for all the operating states is observed. The measured switching ratio of the antenna is 1.7:1 for the lower and upper bands.

Measured normalized co- and cross- polarized radiation patterns of the antenna in two principal cut planes are shown in Fig. 3.38 for both bands. For each band two radiation patterns are shown, one for the filled with Galinstan (loaded) case, and one for the baseline (non-loaded) state. The maximum measured gains of the antenna at these four frequencies of 3.2, 1.85, 5.4, and 4.2 GHz are 2, 1.1, 3.4, and 2.8 dBi, respectively. The related state numbers, and frequencies at which each radiation pattern is measured are also shown in Fig. 3.38. Measurements show a minimum efficiency of 78%, and 82%, for the first and second bands, respectively. The major contributor to the reduced efficiency of the antenna is the reduction of its electrical size as a result of capacitive loading. Also, loading the antenna with lossy materials such as PDMS affects the efficiency. Although the resistivity of Galinstan is 17.2 times higher than that of Copper, the way it is used for tuning (just as a loading cap) results in a negligible contribution to loss and thus efficiency.

Generally, the most important practical concerns regarding liquid-based tuning methods are the switching speed, integration of syringes with the antenna structure in practical applications, and liquid metal residues due to oxidization. While the reusable syringes seem to offer an effective actuation method for experimental purposes, the methods in [34, 80] also can be applied to the tuning approach proposed in this paper to achieve much faster (movement speed of 0.8 mm/s) and easier switching between states. Also, micro-pumps can be used to help with automation, integration, and switching speed [91].

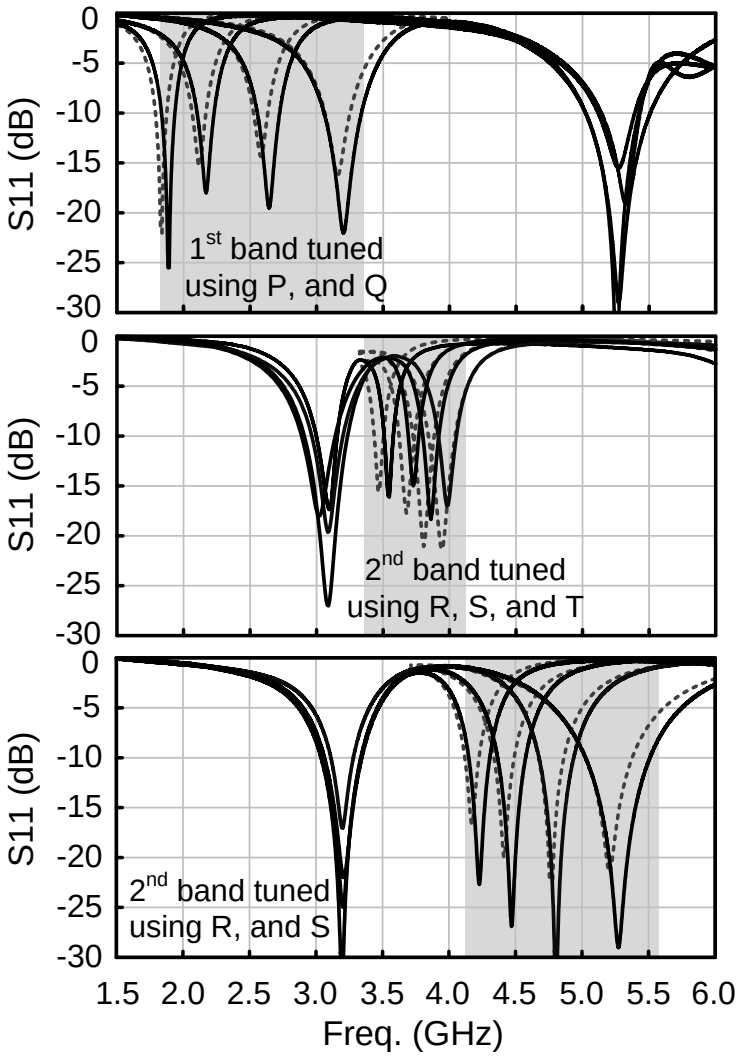

PQRST	1st band (GHz)	2nd band (GHz)
00000	3.20	5.40
10000	2.60	5.35
01000	2.20	5.30
11000	1.80	5.30

PQRST	1st band (GHz)	2nd band (GHz)
00001	3.15	4.00
00101	3.18	3.80
00011	3.15	3.70
00111	3.10	3.55

PQRST	1st band (GHz)	2nd band (GHz)
00000	3.20	5.35
00100	3.20	4.80
00010	3.20	4.45
00110	3.20	4.25

Fig. 3.37: Simulated (dashed) and Measured (solid) reflection coefficient of the dual-band antenna for twelve states in which one band is always fixed (out of the possible 32 states). The shown states are tabulated on the right.

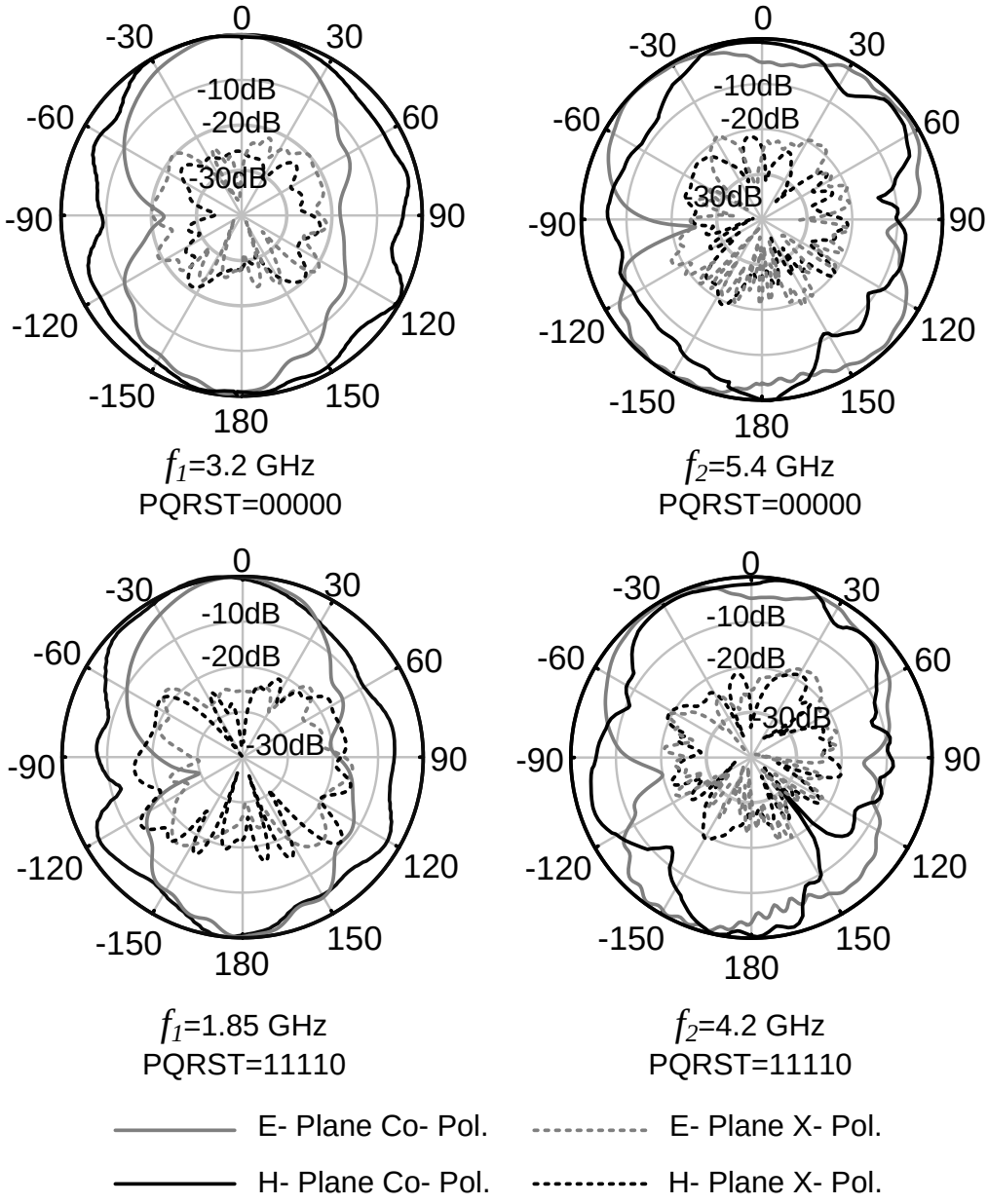

Fig. 3.38: Normalized measured radiation pattern of the antenna for first and second bands for two different states.

In order to examine the issues regarding the liquid metal oxidization, one of the micro-channels was washed with Teflon and refilled with Galinstan for 10 times. Each time the performance of the antenna was measured and the results did not show significant changes in comparison with the original ones (the ones observed during the first measurements). Also, applying the methods in [34, 80] are proven to remove the liquid metal residues, further motivating future research to employ them as the actuation method.

3.3.4 Conclusion

Liquid metal Galinstan is used to implement microfluidic-based switchable capacitors by which frequency reconfiguration of a dual-band slot antenna is achieved. The antenna shows a discrete tuning ratio of 1.7:1 for each band and an entire covering range of 3:1. Since the proposed antenna is not using any non-linear devices, it is expected to be capable of handling high input RF powers for long excitation conditions.

3.4 A Reconfigurable Quarter-mode Substrate Integrated Waveguide Cavity Filter Employing Liquid-metal Capacitive Loading

3.4.1 Introduction

Liquid-based tuning has become popular in the design of tunable filters over the past years [63, 67, 69, 70]. Due to the highly-linear nature of this tuning method it is found promising for high-power applications in comparison with conventional tuning methods based on RF MEMS and PIN diodes [63]. In [63], a broadside coupled split ring resonator filter is presented in which one of the resonators is constructed from liquid metal. By gradually replacing the liquid metal with low loss dielectric liquid, the frequency of the filter is tuned with a tuning ratio of 1.33:1. In [69], instead of liquid metal, metalized glass chunks are employed on top of each resonator gap. Using the metalized glass chunks results in a higher tuning range of 1.65:1 and a lower in-band loss of 1.7 dB. Lumped inductors are used to keep the external quality factor unchanged over the tuning range. However, these lumped inductors will decrease the power handling capabilities of the filter. In [70], a microstrip bandpass filter based on liquid crystal polymer (LCP) with integrated microfluidic channel is proposed. By replacing DI water with acetone, the dielectric constant of a microstrip filter is changed. A micropump is employed to inject different fluids and provide enough pressure to trap the liquid inside the microfluidic channel. Two different frequency states of the filter result in a tuning ratio of 1.5:1.

In this section, a microfluidically reconfigurable ultra-compact substrate integrated waveguide (SIW) cavity filter is proposed. The filter is designed based on quarter-mode cylindrical SIW cavities. An SIW filter is chosen for its superior power handling capability and high quality factor [41, 99]. By employing a shunt shorting via and a series capacitive gap on the SIW top wall, each cavity resonator is loaded

capacitively between the top and bottom walls. The tuning method is based on the capacitive loading effect of liquid metal Galinstan on top of the quarter-ring gaps. By filling the channel with Galinstan, it is possible to change the loading capacitance value and thus alter the center frequency of the filter [67]. The reconfigurable QMSIW cavity filter is implemented based on directly bonding the Polydimethylsiloxane (PDMS) structure (including the micro-channels) to the Rogers dielectric layer using a 15μm thick spin-coated layer of PDMS.

3.4.2 Filter Design

Fig. 3.39 shows the top and A-A' cross section views of the proposed filter. The filter is designed based on Arlon AD1000 substrate (ϵ_r=10.2, tanδ=0.0023). A PDMS structure including one microchannel is employed to place Galinstan on top of the capactive gaps of each resonator. In order to avoid the liquid metal Galinstan to stick to channel walls, Teflon solution is used as a lubricator (Teflon AF 400S2-100-1, 1% Teflon powdered resin dissolved in 3M FC-40 from DuPont). The PDMS structure and the circuit board with the through vias are connected to each other using a very thin spin-coated layer of PDMS (t=15μm).

The quarter-mode SIW cavity resonator is designed based on the approach first introduced in [53] for QMSIW resonators. A full-mode SIW cylindrical cavity resonator is first loaded with a shunt via in the center (Fig. 3.40). Afterwards, a capacitive ring gap disconnects the top and bottom walls and loads the cavity resonator with a small capacitance value. Fig. 3.40 also shows how the ring gap-loaded cylindrical SIW cavity can be divided up into four identical sections. The E-field distribution inside the SIW and the QMSIW cavity resonators is shown. Since the cutting lines are fictitious magnetic walls, each of the quadrants operates at a very similar mode to a full mode SIW resonator (Fig. 3.40). This results in a $\sim$75%

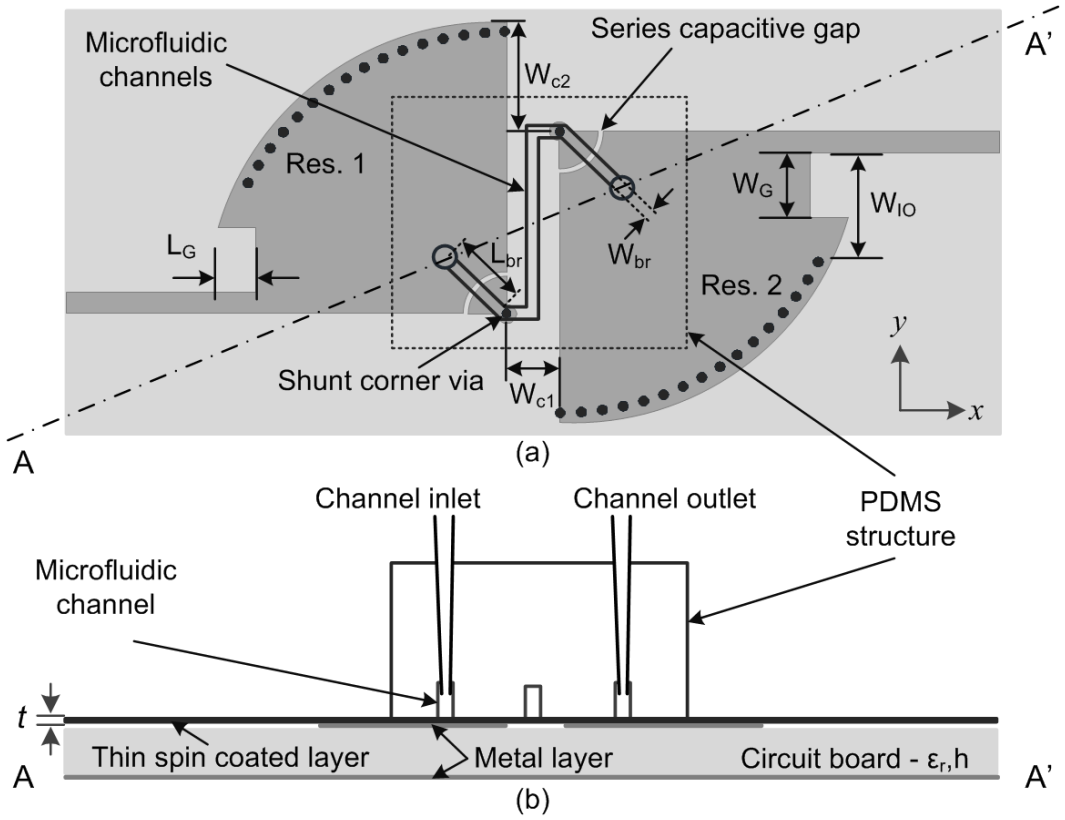

Fig. 3.39: (a) Top view of the microfluidically-reconfigurable QMSIW cavity filter. (b) A-A' cross section view of the filter.

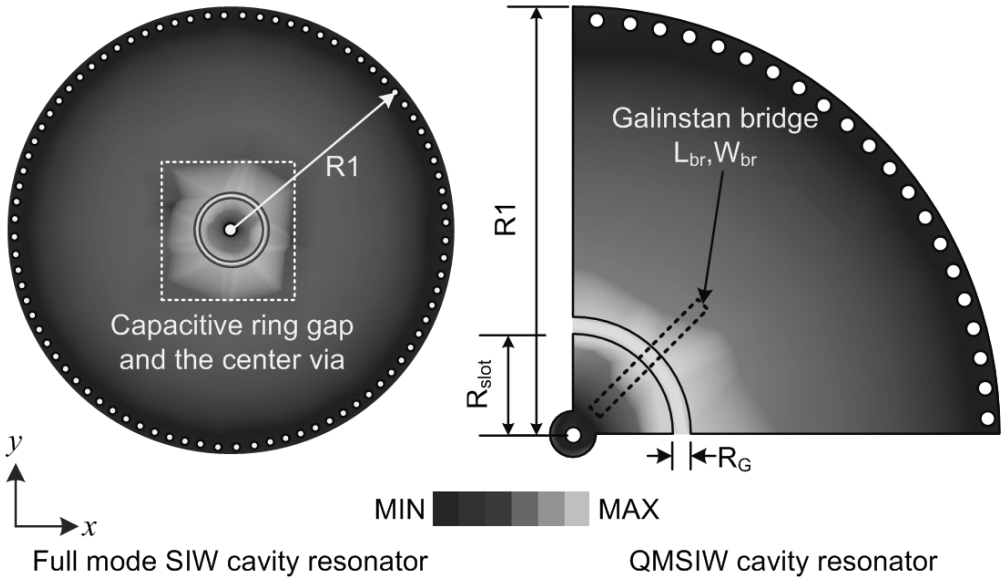

Fig. 3.40: E-field distribution inside a full mode SIW, and a QMSIW resonator with the same radius, loaded with a capacitive ring and quarter-ring gap, respectively. The Galinstan bridge location is shown in dashed-line.

miniature cavity resonator. By using the shunt via and the capacitive gap, the maximum E-field distribution is forced to be around the capacitive gap instead of the center of the cavity resonator. Accordingly, placing the Galinstan bridge on top of this ring gap, increases the ring gap's equivalent capacitance value. As a result of this additional capacitive loading, the frequency of the resonator is shifted down and both miniaturization and tuning is achieved. The amount of this frequency shift mainly depends on three parameters. 1) The length of the Galinstan bridge (L_{br}), 2) the width of the Galinstan bridge (W_{br}), and 3) the thickness of the PDMS spin-coated layer which controls the distance between the bridge and the circuit board (t).

A two-pole coupled resonator bandpass filter based on the proposed microfluidically reconfigurable QMSIW cavity resonator is designed to operate at ∼1.1 GHz. The inter-resonator coupling coefficient K_{12} and the external quality factor Q_e are

calculated using low-pass Chebyshev prototype design values g_0, g_1, g_2, g_3 as [100]

$$K_{12} = \frac{FBW}{\sqrt{g_1 g_2}} \quad , \quad Q_e = \frac{g_0 g_1}{FBW} \tag{3.4}$$

where FBW denotes the filter fractional bandwidth. For a 0.01 dB passband ripple response with a FBW of 5%, the above equations translate into a $K_{12} = 0.14$, and a $Q_e = 9$. To obtain the proper K_{12} value, first, the input and output ports of the filter are weakly coupled to the QMSIW cavity resonators, using the narrow inductive irises at the input/output. The distance of the two resonators along x-axis, $\mathrm{W_{c1}}$, is then adjusted using the 3D full-wave simulator, HFSS[14], to achieve the required K_{12} value using [100]

$$K_{12} = \frac{f_1^2 - f_2^2}{f_1^2 + f_2^2} \tag{3.5}$$

where f_1 and f_2 are the two resonant peaks seen in $\mathrm{S_{21}}$ simulation results, also known as odd- and even-mode resonance frequencies, respectively.

The external quality factor (Q_e) can be also extracted using a singly loaded QMSIW cavity resonator. The Q_e then can be computed from 3D full-wave simulations and by employing the expression [100]

$$Q_e = \frac{f_0}{\Delta f_{\pm 90^\circ}} \tag{3.6}$$

where f_0 is the resonance frequency of the QMSIW cavity resonator and $\Delta f_{\pm 90^\circ}$ denotes the difference of frequencies of which a phase shift of $\pm 90^\circ$ occurs in the $\mathrm{S_{11}}$ response of the cavity resonator. In order to obtain the required Q_e found from (3.4), the width of the input/output inductive iris, $\mathrm{W_{IO}}$, and the capacitive gap, $\mathrm{L_G}$,

[14]Note that the distance along the y-axis, $\mathrm{W_{c2}}$, is fixed for the maximum coupling factor achievable by adjusting this parameter.

Table 3.5: Final Dimensions (mm) of the Microfluidically Reconfigurable QMSIW Filter.

L	62	W	41	h	3.2
R_1	29	R_{slot}	4	R_G	0.2
W_{IO}	12	W_{c1}	6	W_{c2}	11
W_G	8	L_G	3.7	R_{via}	0.5
L_{br}	8	W_{br}	1.2	h_{pdms}	5

are adjusted. While the first one is used for coarse adjustment of the Q_e, the latter is used for fine adjustment.

In order to make the injection of Galinstan easier, and to minimize the number of inlets/outlets needed, the Galinstan bridges are connected to each other so that both channels can be filled or emptied at the same time using a single syringe. This also helps with future use of the design for analog tuning of the filter[15]. The extended portion of the Galinstan bridge is placed in the coupling area and since the top wall of the cavity is etched in that area, this extra length will negligibly load the structure. A small portion that is closer to the shunt corner via will slightly change the coupling factor. Hence, this extra portion of the channel needs to be included in full-wave simulations of the filter to precisely adjust W_{c1}. The final values of these parameters along with the other filter parameters are tabulated in Table 3.5.

3.4.3 Fabrication Process and Experimental Results

3.4.3.1 Fabrication

A prototype of the filter is fabricated using common PCB technology, 3D printer, and softlithography techniques (see Fig. 3.41). The 3D mold needed is designed in Solidworks and then printed layer by layer using a Stereolithography 3D printer. The fabricated mold is reusable and makes mass fabrication of the filter easy. Any

[15]By controlling the length of the Galinstan above the quarter-ring gaps.

Table 3.6: Performance Parameters of The Filter For Both States.

	Empty	Filled with Galinstan
Operating Center Frequency	1.12 GHz	0.65 GHz
3-dB Fractional Bandwidth	∼5.2%	∼3.7%
Insertion Loss	2.5 dB	3.45 dB
Return Loss	>15 dB	>15 dB

sort of chemical residues are cleaned off the fabricated mold by isopropyl alcohol (IPA). Then the mold is left in heating oven at 65°C for at least 24 hours. The holes used for inlet and outlet are punched carefully into the PDMS structure. Two corner via posts are filled with liquid PDMS in order to avoid Galinstan from touching the copper surface. Afterwards a 15μm thick layer of PDMS is spin-coated and heat cured on the PCB board. During this step, removable paper tape is used on the board at the input and output microstrip lines to shape the spin-coated layer in a way that soldering the SMA connectors later won't be an issue. A permanent bond between PDMS thin layer and the PDMS structure including the micro-channel is created using oxygen plasma bonding technique. Finally, flexible tubings are inserted into the punched holes to serve as inlet and outlet of liquids. Micro-scale syringes are used to inject Galinstan into the micro-channel and Teflon solution is used to evacuate Galinstan from the channel.

3.4.3.2 Experimental Results

The fabricated prototype of the filter shown in Fig. 3.41 is measured using a 2 port network analyzer (Agilent N5230A). Fig. 3.42 shows the simulated and measured S-parameters of the filter for the two cases of filled and empty channels. The measured insertion loss is 2.5 and 3.45 dB at 1.12 and 0.65 GHz, respectively. The measured return loss of the filter is higher than 15 dB for both states. A switching ratio of 1.72:1 is achieved. The filter shows a measured fractional bandwidth of ∼4.55±0.7 %. The reason for the different FBW at two states is due to different

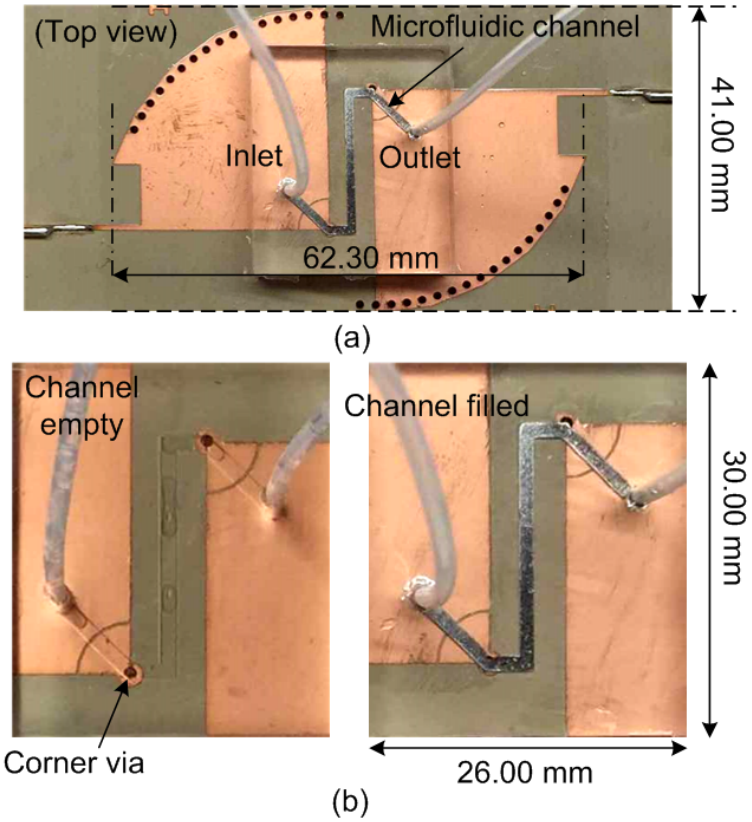

Fig. 3.41: (a) Fabricated prototype of the filter. (b) Magnification of two empty and filled channel configurations.

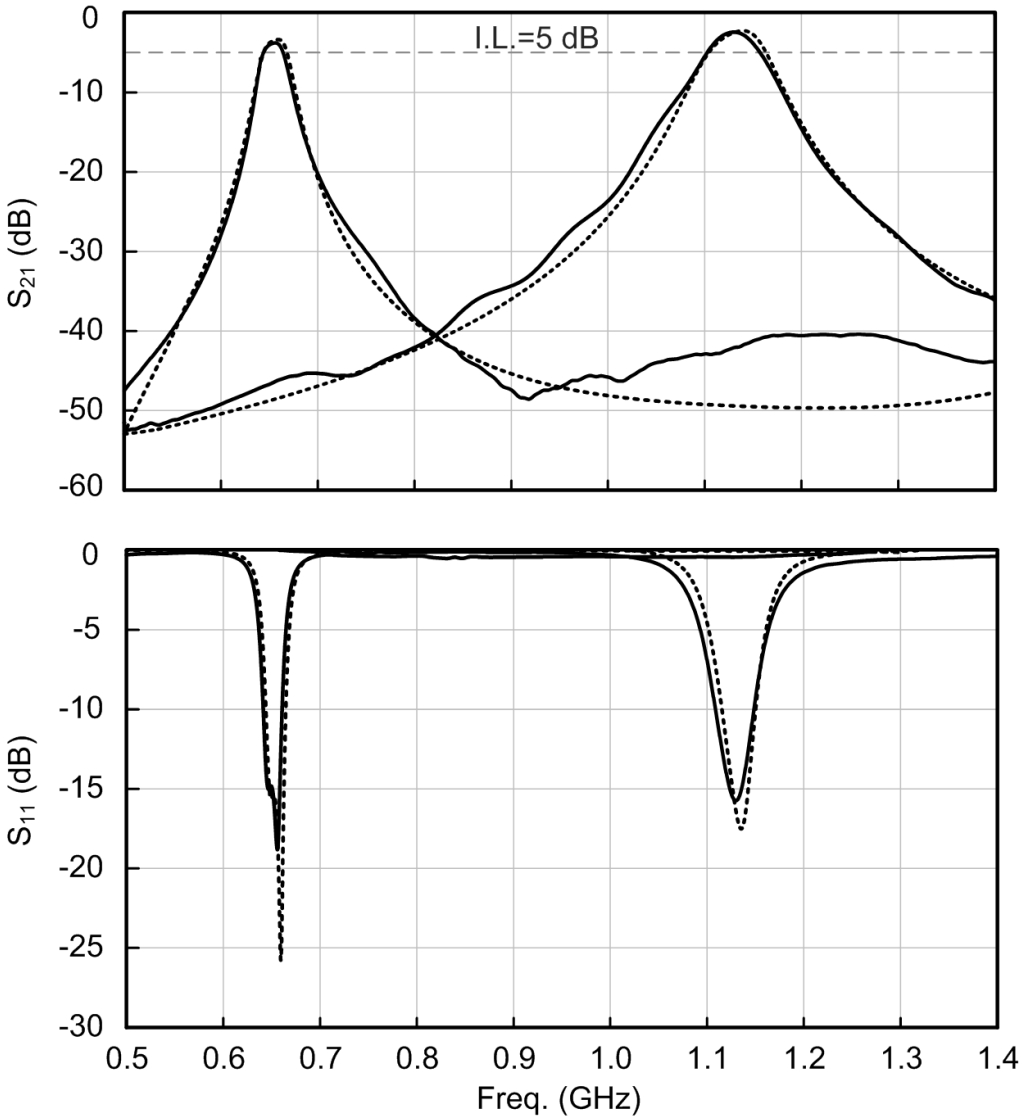

Fig. 3.42: Simulated and measured S-parameter results of the proposed filter.

coupling and external quality factors at each state. Different method of coupling and channel configuration seems to be the solution to achieve a two-pole filter with an approximately constant FBW. The lowest operating frequency of the filter at 0.65 GHz translates into a miniaturization factor of 85%, considering a full-mode 2-pole SIW filter operating at the same frequnecy. The overall size of the filter excluding the microstrip feed lines is 62 $\times$ 41 mm^2 which is equal to $0.15\lambda_0 \times 0.1\lambda_0$, where λ_0 is the free space wavelength at the lowest operating frequency. Table 3.6 compares the filter performance parameters of both operating states.

3.4.4 Conclusion

A microfluidically reconfigurable ultra-compact QMSIW filter is presented. Both the proposed tuning method and the SIW-based filters are suitable for high-power applications. Also, by employing the proposed capacitive switching method, the quarter mode SIW filter is further miniaturized, and a final miniaturization factor of 85% is achieved. The filter shows a switching range of 0.65-1.12 GHz (1.72:1 tuning ratio) with a maximum in-band loss of 3.5 dB.

3.5 Reconfigurable Quarter-mode SIW Antenna Employing a Fluidically Switchable Via

3.5.1 Introduction

Recently different liquid-based tuning approaches have been demonstrated [34, 90, 91, 93, 98]. These tuning methods are believed to have three main advantages over the conventional methods based on semiconductor, and MEMS devices: 1) they are expected to be capable of high-power RF inputs, 2) employing soft materials can result in flexible and wearable devices, and 3) liquid elements are capable of retaining their physical position after removing the actuation force, whether it is a pressure driven force or an electrically actuated one [34]. The existing work in the area of liquid metal-based antenna tuning includes changing the length of antenna [90], using the liquid metal as a non-ideal RF shortening switch [91], using the liquid metal channel as a reactive loading element [93, 98], and changing the feed structure [34].

It is shown in [51] that a QMSIW antenna can be formed by bisecting a SIW cavity on its fictitious magnetic walls. This results in an ultra-miniature antenna with a leaky-based one-sided radiation pattern. Finding a way to tune this antenna might be an appealing remedy for the demand of tunable small antennas with a one-sided radiation characteristics.

This section investigates the application of fluidically-switchable via posts in frequency tuning of SIW antennas working in the microwave band. A non-plated via hole in the corner of a QMSIW is employed. Initially this disconnected via hole does not affect the antenna performance. However, when filled with Galinstan, the result is E-field perturbations inside the cavity as described in detail in [60], and consequently, an up-shift in the antenna operating frequnecy.

3.5.2 Antenna Topology and Design

Fig. 3.43 shows the top and A-A' cross-section views of the proposed reconfigurable antenna along with the magnification of the switchable via in the ON and OFF states. The antenna is based on a Rogers RT/Duroid 5880 ($\epsilon_r = 2.2$, $tan\delta = 0.0009$) with a thickness of $h = 1.6$ mm. Two PDMS structures including the micro-channels are employed to locate Galinstan in the non-plated via post. In order to avoid the liquid metal Galinstan to stick to channel walls, Teflon solution is used as a lubricator (Teflon AF 400S2-100-1, 1% Teflon powdered resin dissolved in 3M FC-40 from DuPont). Both top and bottom PDMS structures and the circuit board with the through vias are connected to each other using very thin spin-coated layers of PDMS (t=60μm) patterned on top and bottom of the PCB, respectively. The idea of reconfiguring an SIW antenna by connecting/disconnecting perturbing via posts is described in detail in [60], where a two-layer structure and p-i-n diodes are employed. However, here the via post is connected/disconnected using liquid metal, Galinstan (an alloy of Gallium, Indium, and Tin).

The QMSIW antenna is designed based on the approach presented in [51]. Since the cutting lines are fictitious magnetic walls, the QMSIW resonator/antenna operates at a very similar mode (TE_{101}) to a full-mode SIW resonator. This means a $\sim$75% miniature antenna.

By inserting a via post into the corner of the QMSIW antenna the field distribution inside the cavity perturbs and as a result the frequency of the antenna shifts up. Accordingly, two channels on both sides of the cavity resonator are placed in a way that the liquid metal can pass through the non-plated via hole. Consequently, the top and bottom metal walls get connected by the liquid metal and the frequency of the antenna changes. By rinsing the channels and via posts with liquid Teflon, the

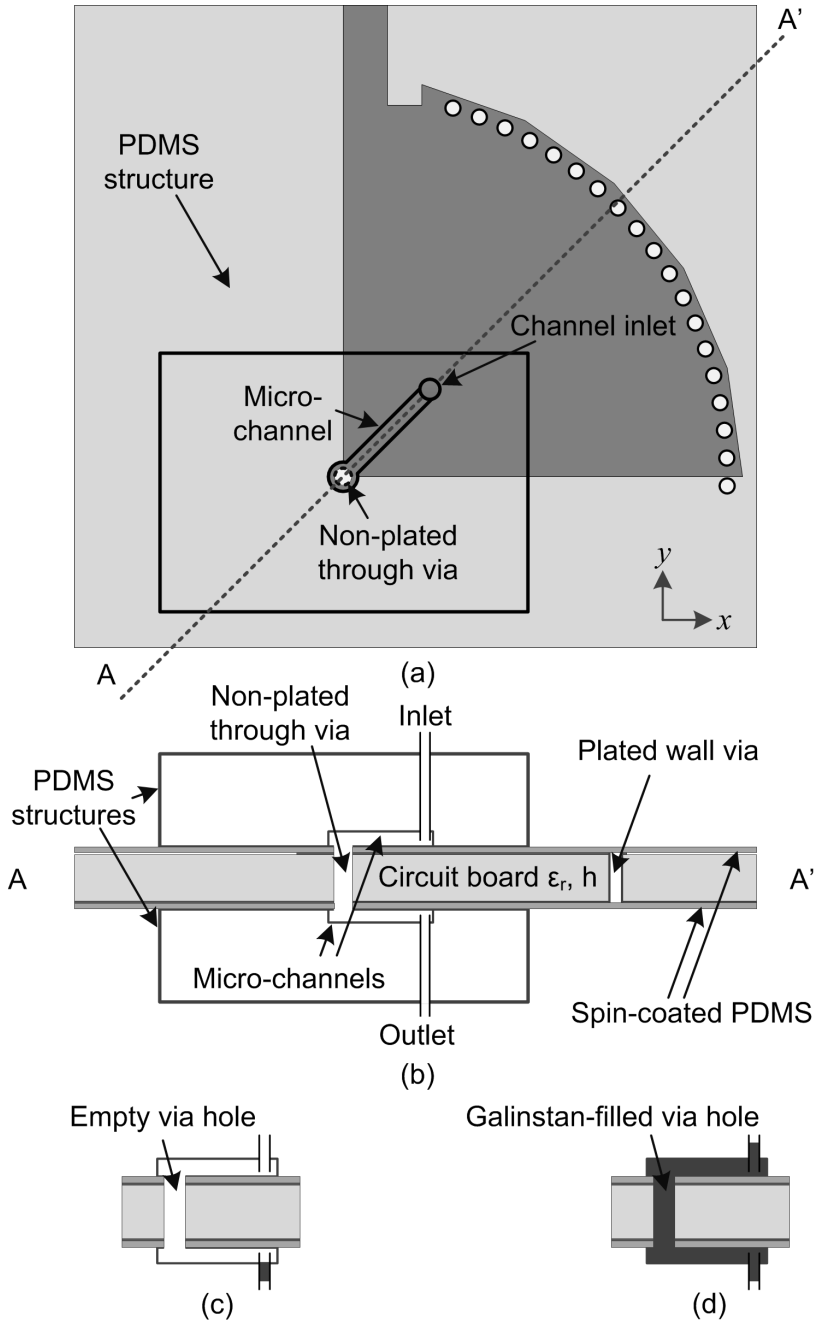

Fig. 3.43: (a) Top view, and (b) A-A' cross section views of the proposed reconfigurable QMSIW antenna. (c), and (d) Magnification of the via post in the OFF, and ON states, respectively.

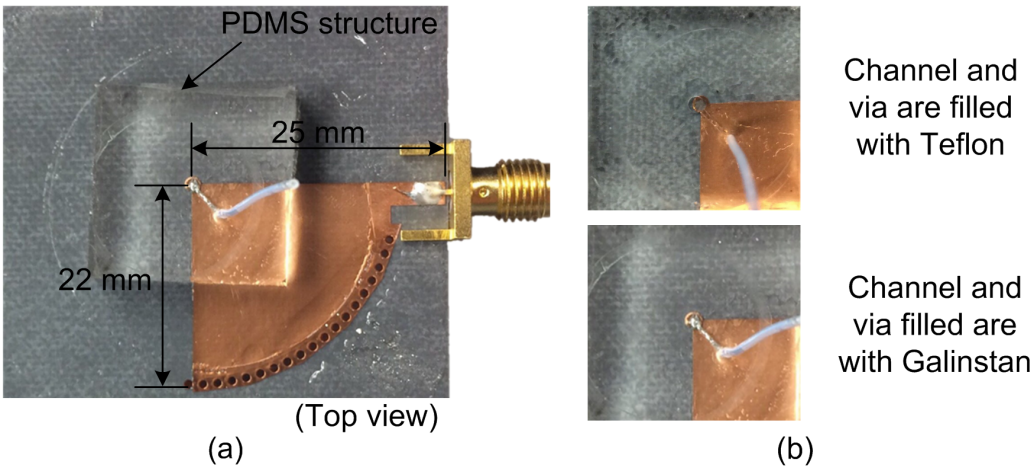

Fig. 3.44: (a) Fabricated prototype of the reconfigurable QMSIW antenna. (b) Magnification of the channel and the switchable via post for two cases of filled and empty.

via post gets disconnected and as a result the frequency of the antenna returns back to the non-loaded state.

3.5.3 Fabrication, Simulations, and Measurements

A prototype of the antenna is fabricated using common PCB technologies, 3D printer, and soft-lithography techniques (see Fig. 3.44). Both sides of the antenna circuit board are spin-coated with a 60μm thick PDMS layer to make the integration of channels and PCB possible. Removable tape is used on the board on the via location on both sides to make sure PDMS won't enter into the via holes. Flexible tubings are used to serve as inlet/outlet of liquids.

Detailed simulations of the antenna are performed in HFSS. The simulated and measured S_{11} results of the antenna are shown in Fig. 3.45. Good agreement between the simulation and measurements is observed. The switching range of the antenna is 3.2–4.7 GHz ($\frac{f_2}{f_1} = 1.45$). The antenna shows a matching level of better than -15 dB for both states. The simulation radiation pattern of the antenna is shown in

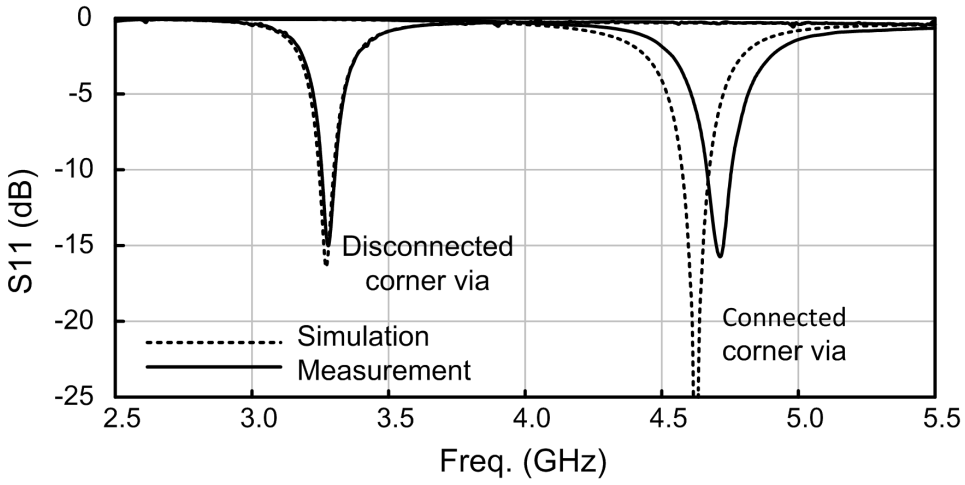

Fig. 3.45: Simulated and measured S_{11} results.

Fig. 3.46 for both operating bands. The antenna offers a linear polarized radiation with purity (i.e. co- to cross- pol. difference) of more than 15 dBc at $\theta = 0°$. The front-to-back ratio for both bands is 15 dBc. and the simulated maximum gain of the antenna is 4.6, and 5 dBi for the first, and second bands, respectively.

3.5.4 Conclusion

A fluidically-switchable via post is proposed. By filling a non-plated via post with Galinstan the top and bottom walls of the cavity are connected and accordingly a frequency up-shift occurs. The measurements show a switching ratio of 1.45:1. The proposed switchable via post can be employed in all sorts of SIW and planar circuits for tuning purposes.

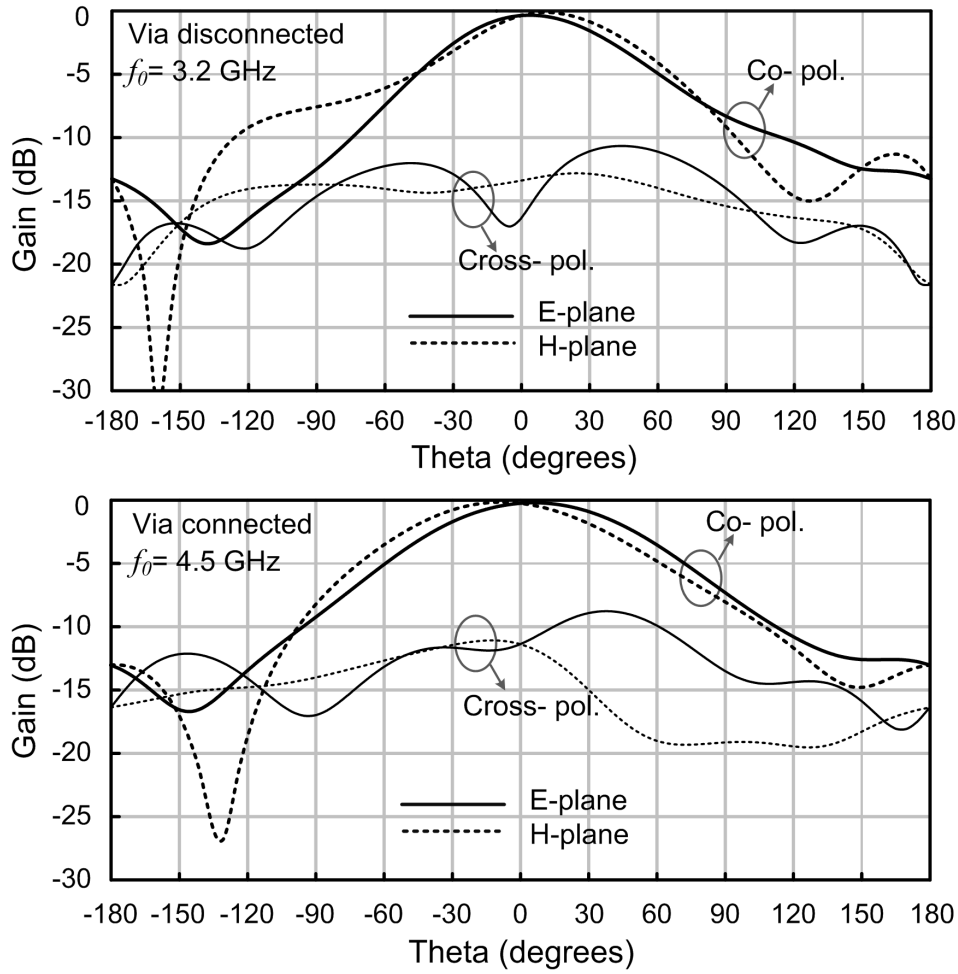

Fig. 3.46: Simulated radiation pattern of the antenna at both operating bands.

4. CONCLUSION AND FUTURE WORK

4.1 Conclusion

The major focus of this dissertation is on advancements in tuning methods for microwave devices. Two different tuning methods are proposed. The first of which is applicable to all sorts of SIW-based passive and active devices and the second method based on capacitive loading effect of liquid metals. In both cases different structures are designed and fabricated to evaluate the methods' performance.

A unique tuning method for substrate integrated waveguide structures is proposed in the second chapter of this dissertation. The method is applied to different antennas to achieve wide tuning ranges and miniaturization at the same time. Miniature structures with highest miniaturization factor of 85% are proposed based on both capacitive loading, and using quarter-mode SIW cavities. Tuning range of 1.1-2.2 GHz for a conventional SIW cavity backed slot antenna is the widest tuning range for a cavity-backed slot antenna achieved at the time of preparing this dissertation, by the best of author's knowledge. Also, this tuning method is modified for a SIW cavity resonator and is employed for a widely-tuned VCO. Due to the high Q of the SIW resonator over the entire tuning range a low phase-noise of at least -109 dBc/Hz at a 100 kHz offset is achieved for the SIW VCO. The proposed tuning method for SIW-based microwave devices has a very high integration potential due to the high isolation of the newly-introduced biasing layer. All the required components of a microwave circuit can be mounted on the back-side of the passive section without affecting the passives' performance. This will limit the size of the entire circuit to the area of the passive component only.

Another major emphasis of this dissertation is on microfluidically-based tunable

microwave devices and their capabilities to be employed in high-power microwave applications. Reconfigurable antennas and filters using the capacitive loading effects of liquid-metal bridges are proposed. As well as achieving wide tuning ranges for the proposed structures, the main focus of this section of the dissertation is on characterizing the power-handling capabilities of such tuning methods. Using a CPW microfluidically-tunable filter, infra-red camera, and a power-amplifying system, these capabilities are characterized experimentally for the first time. Also, COMSOL simulations are proposed to better understand the behavior of the structure. The filter proposed is tunable in the range of 3.4-5.5 GHz, and is capable of handling high-average input-powers with levels of as high as 10 W, without any significant changes in the performance of the filter. Dissertation also discusses a microfluidically-tunable quarter-mode SIW antenna in which a via post is shortened physically to achieve different frequnecy-modes of operation.

Like any other emerging technology, there are some issues and challenges such as durability, repeatability, integration, speed of switching, etc which are discussed in each section for the proposed microfluidically-tuned microwave components. For some cases it is tried to provide remedies and for the others, just possibilities are mentioned.

4.2 Future Work

The works presented in this thesis mainly covered SIW tunable structures, and microfluidically-tunable and miniature microwave devices. In this section, the major areas where the present work can be extended are identified.

4.2.1 Combining SIW Structures With Fluidic Tuning Techniques

One of the most important advantages of fluidic-based tunable microwave devices is known to be high-power tolerability. While the design proposed in 3.1 of this

thesis is characterized in terms of power handling capabilities, no heat management is done during the design process in order to increase the input power tolerance of the filter. Also, the CPW filter employed does not have a high heat toleration caused by high input power levels. Two other works are proposed in which the SIW filters and antennas are combined with liquid-based tuning methods. It is believed by the author that since the SIW structures are high power tolerable by nature, their combination with liquid-based tuning devices can result in the highest power tolerable tunable passive components. Also, fluidics can be used to make the bulky SIW components smaller in case of being employed as loading capacitors for miniaturization purposes.

4.2.2 Resolving the Stiction and Actuation Issues for Galinstan

Third chapter of this thesis focused mostly on how to employ the microfluidics within the microwave circuits to achieve the widest possible tuning range. Although, the actuation method based on syringes and hydraulic forces proves to be an effective one at least for experimental purposes, it is not ideal for commercialization of these devices as it requires additional syringes or pumps which might be bulky for most of applications.

As a result, alternative methods of actuation need to be studied and applied to the tuning techniques proposed in this thesis. One of the most practical techniques at the time of preparing this thesis, is the one based on continuous electrowetting of liquid metal inside the channels [34]. The advantage of this method is that once the liquid metal and the electrolyte are injected into the channel there will not be any other injections needed. Thus, the switching speed in this method is only limited to the movement speed of the liquid metal inside the channel and not the injection time. This method is based on continuous electrowetting of Galinstan inside the micro-channels and can be utilized with the same micro-channel topology proposed

in this paper. As presented in [34], by the aid of an electrolyte, and just a single excitation voltage, the liquid metal moves inside the channel without any residues left behind. The drawback of this method, however, is that the electrolyte itself is a lossy material and further increases the insertion loss of the filter. Ultimately higher insertion loss would reduce the power-handling capabilities of the filter. As a result, it is very important to make considerations in choosing the location of the electrolyte well when designing such filters.

REFERENCES

[1] X. Liu, L. P. Katehi, W. J. Chappell, and D. Peroulis, "Power handling of electrostatic mems evanescent-mode (eva) tunable bandpass filters," *IEEE Trans. Microw. Theory Techn.*, vol. 60, no. 2, pp. 270–283, Feb. 2012.

[2] D. M. Pozar, *Microwave engineering*. John Wiley & Sons, 2009.

[3] R. E. Collin, *Foundations for microwave engineering*. John Wiley & Sons, 2007.

[4] N. Marcuvitz, *Waveguide handbook*. IET, 1951, no. 21.

[5] J. Helszajn, *Ridge waveguides and passive microwave components*. IET, 2000, no. 49.

[6] J. Hirokawa and M. Ando, "Single-layer feed waveguide consisting of posts for plane tem wave excitation in parallel plates," *IEEE Trans. Antennas Propag.*, vol. 46, no. 5, pp. 625–630, 1998.

[7] H. Uchimura, T. Takenoshita, and M. Fujii, "Development of a laminated waveguide," *IEEE Trans. Microw. Theory Techn.*, vol. 46, no. 12, pp. 2438–2443, 1998.

[8] D. Deslandes and K. Wu, "Single-substrate integration technique of planar circuits and waveguide filters," *IEEE Trans. Microw. Theory Techn.*, vol. 51, no. 2, pp. 593–596, 2003.

[9] K. Wu, D. Deslandes, and Y. Cassivi, "The substrate integrated circuits-a new concept for high-frequency electronics and optoelectronics," in *Telecommunications in Modern Satellite, Cable and Broadcasting Service, 2003. TELSIKS 2003. 6th International Conference on*, vol. 1. IEEE, 2003, pp. P–III.

[10] F. Xu and K. Wu, "Guided-wave and leakage characteristics of substrate integrated waveguide," *IEEE Trans. Microw. Theory Techn.*, vol. 53, no. 1, pp. 66–73, 2005.

[11] D. Deslandes and K. Wu, "Accurate modeling, wave mechanisms, and design considerations of a substrate integrated waveguide," *IEEE Trans. Microw. Theory Techn.*, vol. 54, no. 6, pp. 2516–2526, 2006.

[12] M. Bozzi, A. Georgiadis, and K. Wu, "Review of substrate-integrated waveguide circuits and antennas," *Microw., Antennas Propag.*, vol. 5, no. 8, pp. 909–920, 2011.

[13] H. Tang, W. Hong, Z. Hao, J. Chen, and K. Wu, "Optimal design of compact millimetre-wave siw circular cavity filters," *Electron. Lett.*, vol. 41, no. 19, pp. 1068–1069, 2005.

[14] G. Q. Luo, Z. F. Hu, L. X. Dong, and L. L. Sun, "Planar slot antenna backed by substrate integrated waveguide cavity," *IEEE Antennas Wireless Propag. Lett.*, vol. 7, pp. 236–239, 2008.

[15] J. C. Bohórquez, H. A. F. Pedraza, I. C. H. Pinzón, J. A. Castiblanco, N. Pena, and H. F. Guarnizo, "Planar substrate integrated waveguide cavity-backed antenna," *IEEE Antennas Wireless Propag. Lett.*, vol. 8, pp. 1139–1142, 2009.

[16] J.-X. Chen, W. Hong, Z.-C. Hao, H. Li, and K. Wu, "Development of a low cost microwave mixer using a broad-band substrate integrated waveguide (siw) coupler," *IEEE Microw. Wirel. Compon. Lett.*, vol. 16, no. 2, pp. 84–86, 2006.

[17] Y. Cassivi and K. Wu, "Low cost microwave oscillator using substrate integrated waveguide cavity," *IEEE Microw. Wirel. Compon. Lett.*, vol. 13, no. 2, pp. 48–50, 2003.

[18] C. Zhong, J. Xu, Z. Yu, and Y. Zhu, "Ka-band substrate integratedwaveguide gunn oscillator," *IEEE Microw. Wirel. Compon. Lett.*, vol. 18, no. 7, pp. 461–463, 2008.

[19] H. Jin and G. Wen, "A novel four-way ka-band spatial power combiner based on hmsiw," *IEEE Microw. Wirel. Compon. Lett.*, vol. 18, no. 8, pp. 515–517, 2008.

[20] M. Abdolhamidi and M. Shahabadi, "X-band substrate integrated waveguide amplifier," *IEEE Microw. Wirel. Compon. Lett.*, vol. 18, no. 12, pp. 815–817, 2008.

[21] L. Yan, W. Hong, G. Hua, J. Chen, K. Wu, and T. J. Cui, "Simulation and experiment on siw slot array antennas," *IEEE Microw. Wirel. Compon. Lett.*, vol. 14, no. 9, pp. 446–448, 2004.

[22] D. Deslandes and K. Wu, "Substrate integrated waveguide leaky-wave antenna: concept and design considerations," in *Asia Pacific Microwave Conference*, 2005.

[23] W. D'Orazio and K. Wu, "Substrate-integrated-waveguide circulators suitable for millimeter-wave integration," *IEEE Trans. Microw. Theory Techn.*, vol. 54, no. 10, pp. 3675–3680, 2006.

[24] S. Yang, C. Zhang, H. K. Pan, A. E. Fathy, and V. K. Nair, "Frequency-reconfigurable antennas for multiradio wireless platforms," *IEEE Microw. Mag.*, vol. 10, no. 1, pp. 66–83, 2009.

[25] G. M. Rebeiz, K. Entesari, I. Reines, S.-J. Park, M. A. El-Tanani, A. Grichener, and A. R. Brown, "Tuning in to rf mems," *IEEE Microw. Mag.*, vol. 10, no. 6, pp. 55–72, 2009.

[26] A. P. Saghati, M. Azarmanesh, and R. Zaker, "A novel switchable single-and multifrequency triple-slot antenna for 2.4-ghz bluetooth, 3.5-ghz wimax, and 5.8-ghz wlan," *IEEE Antennas Wireless Propag. Lett.*, vol. 9, pp. 534–537, 2010.

[27] C. A. Balanis, *Antenna theory: analysis and design.* John Wiley & Sons, 2012.

[28] A. P. Saghati and K. Entesari, "A reconfigurable siw cavity-backed slot antenna with one octave tuning range," *IEEE Trans. Antennas Propag.*, vol. 61, no. 8, pp. 3937–3945, 2013.

[29] G. Gonzalez, *Microwave transistor amplifiers: analysis and design.* Prentice hall New Jersey, 1997, vol. 2.

[30] P. Blondy and D. Peroulis, "Handling rf power: The latest advances in rf-mems tunable filters," *Microwave Magazine, IEEE*, vol. 14, no. 1, pp. 24–38, Jan 2013.

[31] F.-S. Su, Y.-M. Chen, and S.-F. Chang, "Packaged tunable combline bandpass filters," *Microwave Magazine, IEEE*, vol. 16, no. 2, pp. 93–98, March 2015.

[32] R. Mansour, F. Huang, S. Fouladi, W. Yan, and M. Nasr, "High-q tunable filters: Challenges and potential," *Microwave Magazine, IEEE*, vol. 15, no. 5, pp. 70–82, July 2014.

[33] K. Entesari, A. Saghati, V. Sekar, and M. Armendariz, "Tunable siw structures: Antennas, vcos, and filters," *IEEE Microw. Magazine*, vol. 16, no. 5, pp. 34–54, Jun. 2015.

[34] R. Gough, A. Morishita, J. Dang, W. Hu, W. Shiroma, and A. Ohta, "Continuous electrowetting of non-toxic liquid metal for rf applications," *IEEE Access*,

vol. 2, pp. 874–882, Aug. 2014.

[35] N. Behdad and K. Sarabandi, "Dual-band reconfigurable antenna with a very wide tunability range," *IEEE Trans. Antennas Propag.*, vol. 54, no. 2, pp. 409–416, Feb. 2006.

[36] A. P. Saghati, M. Azarmanesh, and R. Zaker, "A novel switchable single-and multifrequency triple-slot antenna for 2.4-ghz bluetooth, 3.5-ghz wimax, and 5.8-ghz wlan," *IEEE Antennas Wireless Propag. Lett.*, vol. 9, pp. 534–537, 2010.

[37] K. Van Caekenberghe and K. Sarabandi, "A 2-bit ka-band rf mems frequency tunable slot antenna," *IEEE Antennas Wireless Propag. Lett.*, vol. 7, pp. 179–182, 2008.

[38] C. White and G. Rebeiz, "A shallow varactor-tuned cavity-backed slot antenna with a 1.9:1 tuning range," *IEEE Trans. Antennas Propag.*, vol. 58, no. 3, pp. 633–639, Mar. 2010.

[39] G. Q. Luo, Z. F. Hu, W. J. Li, X. H. Zhang, L. L. Sun, and J. F. Zheng, "Bandwidth-enhanced low-profile cavity-backed slot antenna by using hybrid siw cavity modes," *IEEE Trans. Antennas Propag.*, vol. 60, no. 4, pp. 1698–1704, Apr. 2012.

[40] F. Giuppi, A. Georgiadis, A. Collado, M. Bozzi, and L. Perregrini, "Tunable siw cavity backed active antenna oscillator," *Electron. Lett.*, vol. 46, no. 15, pp. 1053–1055, 2010.

[41] V. Sekar, M. Armendariz, and K. Entesari, "A 1.2–1.6-ghz substrate-integrated-waveguide rf mems tunable filter," *IEEE Trans. Microw. Theory Techn.*, vol. 59, no. 4, pp. 866–876, April 2011.

[42] X.-P. Chen, K. Wu, and D. Drolet, "Substrate integrated waveguide filter with improved stopband performance for satellite ground terminal," *IEEE Trans. Microw. Theory Techn.*, vol. 57, no. 3, pp. 674–683, Mar. 2009.

[43] Ansys HFSS ver. 15, Ansys Inc.. Canonsburg, PA, USA, 2013.

[44] N. Marcuvitz, *Waveguide Handbook*. Newyork: Dover, 1951.

[45] NXP Semiconductors. Eindhoven, the Netherlands.

[46] D. Peroulis, K. Sarabandi, and L. Katehi, "Design of reconfigurable slot antennas," *IEEE Trans. Antennas Propag.*, vol. 53, no. 2, pp. 645–654, Feb. 2005.

[47] Rogers Corp., Connecticut, US.

[48] Y. Dong and T. Itoh, "Miniaturized substrate integrated waveguide slot antennas based on negative order resonance," *IEEE Trans. Antennas Propag.*, vol. 58, no. 12, pp. 3856–3864, Dec. 2010.

[49] A. Pourghorban Saghati and K. Entesari, "A miniaturized switchable siw-cbs antenna using positive and negative order resonances," in *Proc. IEEE APS-URSI*, Jul. 2013, pp. 566–567.

[50] S. Somarith, H. Kang, and S. Lim, "Frequency reconfigurable and miniaturized substrate integrated waveguide interdigital capacitor (siw-idc) antenna," *IEEE Trans. Antennas Propag.*, vol. 62, no. 3, pp. 1039–1045, Mar. 2014.

[51] C. Jin, R. Li, A. Alphones, and X. Bao, "Quarter-mode substrate integrated waveguide and its application to antennas design," *IEEE Trans. Antennas Propag.*, vol. 61, no. 6, pp. 2921–2928, Jun. 2013.

[52] M. El-Tanani and G. Rebeiz, "A two-pole two-zero tunable filter with improved linearity," *IEEE Trans. Microw. Theory Techn.*, vol. 57, no. 4, pp. 830–839, Apr. 2009.

[53] Z. Zhang, N. Yang, and K. Wu, "5-ghz bandpass filter demonstration using quarter-mode substrate integrated waveguide cavity for wireless systems," in *Proc. Radio and Wireless Symp.*, Jan. 2009, pp. 95–98.

[54] Y. Cassivi, L. Perregrini, K. Wu, and G. Conciauro, "Low-cost and high-q millimeter-wave resonator using substrate integrated waveguide technique," in *Microwave Conference, 2002. 32nd European*, Sep. 2002, pp. 1–4.

[55] S. Sirci, J. Martinez, M. Taroncher, and V. Boria, "Varactor-loaded continuously tunable siw resonator for reconfigurable filter design," in *Microwave Conference (EuMC), 2011 41st European*, Oct. 2011, pp. 436–439.

[56] F. He, X.-P. Chen, K. Wu, and W. Hong, "Electrically tunable substrate integrated waveguide reflective cavity resonator," in *Microwave Conference, 2009. APMC 2009. Asia Pacific*, Dec. 2009, pp. 119–122.

[57] Z. Chen, W. Hong, J. Chen, and J. Zhou, "Design of high-q tunable siw resonator and its application to low phase noise vco," vol. 23, no. 1, Jan. 2013, pp. 43–45.

[58] F. F. He, K. Wu, W. Hong, L. Han, and X. P. Chen, "A low phase-noise vco using an electronically tunable substrate integrated waveguide resonator," *IEEE Trans. Microw. Theory Techn.*, vol. 58, no. 12, pp. 3452–3458, 2010.

[59] M. Armendariz, V. Sekar, and K. Entesari, "Tunable siw bandpass filters with pin diodes," in *40th Eur. Microw. Conf.*, Sep. 2010, pp. 830–833.

[60] A. P. Saghati and K. Entesari, "A reconfigurable siw cavity-backed slot antenna with one octave tuning range," *IEEE Trans. Antennas Propag.*, vol. 61, no. 8, pp. 3937–3945, 2013.

[61] V. Sekar, W. J. Torke, S. Palermo, and K. Entesari, "A self-sustained microwave system for dielectric-constant measurement of lossy organic liquids," *IEEE Trans. Microw. Theory Techn.*, vol. 60, no. 5, pp. 1444–1455, Feb. 2012.

[62] Advanced Design Systems 2011.01, Agilent Technol. Inc. Palo Alto, CA, USA, 2011.

[63] G. Mumcu, A. Dey, and T. Palomo, "Frequency-agile bandpass filters using liquid metal tunable broadside coupled split ring resonators," *IEEE Microw. Wirel. Compon. Lett.*, vol. 23, no. 4, pp. 187–189, Apr. 2013.

[64] M. Khan, G. Hayes, S. Zhang, M. Dickey, and G. Lazzi, "A pressure responsive fluidic microstrip open stub resonator using a liquid metal alloy," *IEEE Microw. Wirel. Compon. Lett.*, vol. 22, no. 11, pp. 577–579, Nov. 2012.

[65] S. Guo, B. J. Lei, W. Hu, W. Shiroma, and A. T. Ohta, "A tunable low-pass filter using a liquid-metal reconfigurable periodic defected ground structure," in *IEEE MTT-S Int. Microw. Symp. Dig.*, Jun. 2012, pp. 1–3.

[66] C.-H. Chen, J. Whalen, and D. Peroulis, "Non-toxic liquid-metal 2-100 ghz mems switch," in *IEEE MTT-S Int. Microw. Symp. Dig.*, Jun. 2007, pp. 363–366.

[67] A. Pourghorban Saghati, J. Batra, J. Kameoka, and K. Entesari, "Microfluidically-tunedminiaturized planar microwave resonators," in *Proc. IEEE Wireless Microw. Conf.*, Jun. 2014, pp. 1–3.

[68] O. Chlieh, W. Khan, and J. Papapolymerou, "Integrated microfluidic cooling of high power passive and active devices on multilayer organic substrate," in *IEEE MTT-S Int. Microw. Symp. Dig.*, Jun. 2014, pp. 1–4.

[69] T. Palomo and G. Mumcu, "Highly reconfigurable bandpass filters using microfluidically controlled metallized glass plates," in *IEEE MTT-S Int. Microw. Symp. Dig.*, Jun. 2014, pp. 1–3.

[70] O. Chlieh, W. Khan, and J. Papapolymerou, "L-band tunable microstrip bandpass filter on multilayer organic substrate with integrated microfluidic channel," in *IEEE MTT-S Int. Microw. Symp. Dig.*, Jun. 2014, pp. 1–4.

[71] K. Entesari and G. Rebeiz, "A 12–18-ghz three-pole rf mems tunable filter," *IEEE Trans. Microw. Theory Techn.*, vol. 53, no. 8, pp. 2566–2571, Aug. 2005.

[72] A. Abbaspour-Tamijani, L. Dussopt, and G. Rebeiz, "Miniature and tunable filters using mems capacitors," *IEEE Trans. Microw. Theory Techn.*, vol. 51, no. 7, pp. 1878–1885, Jul. 2003.

[73] K. C. Gupta, R. Garg, I. J. Bahl, and P. Bhartia, *Microstrip lines and slotlines*. 2nd ed. Norwood, MA: Artech House, 1979.

[74] Sonnet ver. 14.54, Sonnet software Inc.. Syracuse, NY, USA, 1986–2013.

[75] B.-H. Jo, L. M. Van Lerberghe, K. M. Motsegood, and D. J. Beebe, "Three-dimensional micro-channel fabrication in polydimethylsiloxane (pdms) elastomer," *IEEE J. Microelectromech. Syst.*, vol. 9, no. 1, pp. 76–81, 2000.

[76] M. Li and N. Behdad, "Fluidically tunable frequency selective/phase shifting surfaces for high-power microwave applications," *IEEE Trans. Antennas Propag.*, vol. 60, no. 6, pp. 2748–2759, Jun. 2012.

[77] COMSOL multiphysics ver. 4.4, COMSOL Inc.. Burlington, MA, USA, 2014.

[78] A. Pourghorban Saghati, S. Baghbani Kordmahale, J. Kameoka, and K. Entesari, "A reconfigurable quarter-mode substrate integrated waveguide cavity

filter employing liquid-metal capacitive loading," in *IEEE MTT-S Int. Microw. Symp. Dig.*, May. 2015, pp. 1–3.

[79] J. Barrera and G. Huff, "A fluidic loading mechanism in a polarization reconfigurable antenna with a comparison to solid state approaches," *IEEE Trans. Antennas Propag.*, vol. 62, no. 8, pp. 4008–4014, Aug. 2014.

[80] M. R. Khan, C. Trlica, and M. D. Dickey, "Recapillarity: Electrochemically controlled capillary withdrawal of a liquid metal alloy from microchannels," *Advanced Functional Materials*, 2014.

[81] T. Weller, L. Katehi, and G. Rebeiz, "Single and double folded-slot antennas on semi-infinite substrates," *IEEE Trans. Antennas Propag.*, vol. 43, no. 12, pp. 1423–1428, Dec 1995.

[82] C.-J. Wang, J.-J. Lee, and R.-B. Huang, "Experimental studies of a miniaturized cpw-fed slot antenna with the dual-frequency operation," *IEEE Antennas Wireless Propag. Lett.*, vol. 2, no. 1, pp. 151–154, 2003.

[83] W.-H. Tu and K. Chang, "Miniaturized cpw-fed slot antenna using stepped impedance resonator," in *Proc. IEEE APS-URSI*, vol. 4. IEEE, 2005, pp. 351–354.

[84] B. Ghosh, S. Haque, and D. Mitra, "Miniaturization of slot antennas using slit and strip loading," *IEEE Trans. Antennas Propag.*, vol. 59, no. 10, pp. 3922–3927, Oct 2011.

[85] C.-P. Lai, S.-C. Chiu, and S.-Y. Chen, "Miniaturization of cpw-fed slot antennas using reactive terminations and truncated bilateral ground plane," *IEEE Antennas Wireless Propag. Lett.*, vol. 11, pp. 1072–1075, 2012.

[86] S.-C. Chiu and S.-Y. Chen, "Miniaturization of cpw-fed slot antenna using a pair of interdigital capacitors," in *Proc. IEEE APS-URSI*, July 2013, pp. 1380–1381.

[87] D. Anagnostou and A. Gheethan, "A coplanar reconfigurable folded slot antenna without bias network for wlan applications," *IEEE Antennas Wireless Propag. Lett.*, vol. 8, pp. 1057–1060, 2009.

[88] J.-H. So, J. Thelen, A. Qusba, G. J. Hayes, G. Lazzi, and M. D. Dickey, "Reversibly deformable and mechanically tunable fluidic antennas," *Advanced Functional Materials*, vol. 19, no. 22, pp. 3632–3637, 2009.

[89] D. Rodrigo, L. Jofre, and B. A. Cetiner, "Circular beam-steering reconfigurable antenna with liquid metal parasitics," *IEEE Trans. Antennas Propag.*, vol. 60, no. 4, pp. 1796–1802, 2012.

[90] A. Dey, R. Guldiken, and G. Mumcu, "Wideband frequency tunable liquid metal monopole antenna," in *Proc. IEEE APS-URSI*, July 2013, pp. 392–393.

[91] A. J. King, J. F. Patrick, N. R. Sottos, S. R. White, G. H. Huff, and J. T. Bernhard, "Microfluidically switched frequency-reconfigurable slot antennas," *IEEE Antennas Wireless Propag. Lett.*, vol. 12, pp. 828–831, 2013.

[92] M. Kelley, C. Koo, H. McQuilken, B. Lawrence, S. Li, A. Han, and G. Huff, "Frequency reconfigurable patch antenna using liquid metal as switching mechanism," *Electron. Lett.*, vol. 49, no. 22, pp. 1370–1371, 2013.

[93] A. Pourghorban Saghati, J. Batra, J. Kameoka, and K. Entesari, "A microfluidically-switched cpw folded slot antenna," in *Proc. IEEE APS-URSI*, July 2014, pp. 557–558.

[94] C. Murray and R. Franklin, "Frequency tunable fluidic annular slot antenna," in *Proc. IEEE APS-URSI*, July 2013, pp. 386–387.

[95] ——, "Independently tunable annular slot antenna resonant frequencies using fluids," *IEEE Antennas Wireless Propag. Lett.*, vol. 13, pp. 1449–1452, 2014.

[96] W.-H. Tu and K. Chang, "Microstrip elliptic-function low-pass filters using distributed elements or slotted ground structure," *IEEE Trans. Microw. Theory Techn.*, vol. 54, no. 10, pp. 3786–3792, Oct 2006.

[97] UCT, Inc. Bristol, PA, USA.

[98] A. Pourghorban Saghati, J. Batra, J. Kameoka, and K. Entesari, "A microfluidically-tuned dual-band slot antenna," in *Proc. IEEE APS-URSI*, Jul. 2014, pp. 1244–1245.

[99] X. Chen and K. Wu, "Substrate integrated waveguide filters: Practical aspects and design considerations," *IEEE Microw. Mag.*, vol. 15, no. 7, pp. 75–83, Nov 2014.

[100] J.-S. G. Hong and M. J. Lancaster, *Microstrip Filters for RF/Microwave Applications*. John Wiley & Sons, 2004.